LAPPEENRANTA
UNIVERSITY OF TECHNOLOGY

Aki Grönman

Numerical modelling of small supersonic axial flow turbines

Thesis for the degree of Doctor of Science (Technology) to be presented with due permission for public examination and criticism in the Auditorium 1383 at Lappeenranta University of Technology, Lappeenranta, Finland on the 25th of August, 2010, at noon.

Acta Universitatis
Lappeenrantaensis
392

Supervisor Professor Jaakko Larjola
Laboratory of Fluid dynamics
LUT Energy
Lappeenranta University of Technology
Finland

Reviewers Professor Jörg Seume
Institute of Turbomachinery and Fluid Dynamics
Leibniz University Hannover
Germany

Associate Professor Andrew Martin
Department of Energy Technology
Royal Institute of Technology
Sweden

Opponents Professor Jörg Seume
Institute of Turbomachinery and Fluid Dynamics
Leibniz University Hannover
Germany

Professor Jos van Buijtenen
Process and Energy Department
Delft University of Technology
The Netherlands

ISBN 978-952-214-953-4
ISBN 978-952-214-954-1 (PDF)
ISSN 1456-4491
Lappeenrannan teknillinen yliopisto
Digipaino 2010

Abstract

Aki Grönman
Numerical modelling of small supersonic axial flow turbines
Lappeenranta 2010
102 pages
Acta Universitatis Lappeenrantaensis 392
Diss. Lappeenranta University of Technology
ISBN 978-952-214-953-4, ISBN 978-952-214-954-1 (PDF), ISSN 1456-4491

Supersonic axial turbine stages typically exhibit lower efficiencies than subsonic axial turbine stages. One reason for the lower efficiency is the occurrence of shock waves. With higher pressure ratios the flow inside the turbine becomes relatively easily supersonic if there is only one turbine stage. Supersonic axial turbines can be designed in smaller physical size compared to subsonic axial turbines of same power. This makes them good candidates for turbochargers in large diesel engines, where space can be a limiting factor. Also the production costs are lower for a supersonic axial turbine stage than for two subsonic stages. Since supersonic axial turbines are typically low reaction turbines, they also create lower axial forces to be compensated with bearings compared to high reaction turbines.

The effect of changing the stator-rotor axial gap in a small high (rotational) speed supersonic axial flow turbine is studied in design and off-design conditions. Also the effect of using pulsatile mass flow at the supersonic stator inlet is studied. Five axial gaps (axial space between stator and rotor) are modelled using three-dimensional computational fluid dynamics at the design and three axial gaps at the off-design conditions. Numerical reliability is studied in three independent studies. An additional measurement is made with the design turbine geometry at intermediate off-design conditions and is used to increase the reliability of the modelling. All numerical modelling is made with the Navier-Stokes solver Finflo employing Chien's $k - \epsilon$ turbulence model.

The modelling of the turbine at the design and off-design conditions shows that the total-to-static efficiency of the turbine decreases when the axial gap is increased in both design and off-design conditions. The efficiency drops almost linearily at the off-design conditions, whereas the efficiency drop accelerates with increasing axial gap at the design conditions.

The modelling of the turbine stator with pulsatile inlet flow reveals that the mass flow pulsation amplitude is decreased at the stator throat. The stator efficiency and pressure ratio have sinusoidal shapes as a function of time. A hysteresis-like

behaviour is detected for stator efficiency and pressure ratio as a function of inlet mass flow, over one pulse period. This behaviour arises from the pulsatile inlet flow.

It is important to have the smallest possible axial gap in the studied turbine type in order to maximize the efficiency. The results for the whole turbine can also be applied to some extent in similar turbines operating for example in space rocket engines. The use of a supersonic stator in a pulsatile inlet flow is shown to be possible.

Keywords: axial turbine, supersonic flow, CFD, turbocharging
UDC 621.438 : 533.6.011.5 : 51.001.57

Acknowledgements

This study was conducted at the Lappeenranta University of Technology, Laboratory of Fluid Dynamics between the years 2007 and 2010. I would like to express my sincere gratitude to professor Jaakko Larjola for offering the possibility to do this research, supervising, and guiding the process. I would also like to thank associate professor Teemu Turunen-Saaresti who has, during our tens of discussions, given me guidance and ideas for this work.

I would like to thank all the people in the Laboratory of Fluid Dynamics for their help and support. Especially, many discussions with D.Sc. Pekka Röyttä were very fruitful. Also professor Jari Backman and D.Sc. Ahti Jaatinen should be mentioned.

I am grateful for the reviewers, professor Jörg Seume of Leibniz University Hannover and associate professor Andrew Martin of Royal Institute of Technology for their valuable insights and comments during the review process.

This study was funded by The Finnish Graduate School in Computational Fluid Dynamics, Finnish Cultural Foundation, South Karelia Regional fund and Henry Ford Foundation.

Without the support of my family and the game of golf this work would have been impossible to conduct. I would like to thank my wife Kaisa for listening and encouraging me during these years.

Aki Grönman
June 2010
Lappeenranta, Finland

Contents

Nomenclature

Latin alphabet

A	pulsation amplitude	
b	blade or vane height	m
c	chord, absolute velocity	m, m/s
C_1	coefficient in the $k-\epsilon$ turbulence model	ms^4/kg
C_2	coefficient in the $k-\epsilon$ turbulence model	ms^4/kg
C_μ	turbulent viscosity coefficient	
c_p	specific heat capacity in constant pressure	J/(kgK)
C_{pr}	static pressure rise coefficient	
E	total internal energy	J/m^3
e	specific internal energy	J/kg
F	inviscid flux vector in x-direction	
f	frequency	1/s
G	inviscid flux vector in y-direction	
g_{ax}	axial distance between stator and rotor at the hub	m
H	inviscid flux vector in z-direction	
I	number of time steps	
k	turbulent kinetic energy	J/kg
l_{ax}	axial distance between stator leading edge and rotor leading edge at the hub	m
l_{TE}	distance from trailing edge	m
n	unit normal vector	
p	pressure	Pa
Q	source term vector	

q_i	heat flux in the i-direction	kg/s
q_m	mass flow	kg/s
R	right hand eigenvector matrix in Roe's method	
r	right hand eigenvector	
R_i	vector in van Albadas limiter	
S	area of cell face	m^2
T	rotation matrix	
T	temperature	K
t	time	s
U	vector of conservative variables	
u	velocity, peripheral velocity	m/s
u, v, w	velocity in x-, y-, and z-direction	m/s
u_τ	friction velocity	m/s
V	volume	m^3
w	relative velocity	m/s
x	distance to axial direction	m
y^+	non-dimensional wall distance	
y_n	normal distance to the wall	m

Greek alphabet

α	absolute flow angle from axial direction	$^\circ$
α	characteristic variable in the Cartesian flux equation	
β	compression wave angle	$^\circ$
δ_{ij}	Kronecker delta function	
ϵ	dissipation of turbulent kinetic energy	W/kg
η	efficiency	$\%$

γ	ratio of specific heats	
κ_1, κ_2	constants in MUSCL-type formula	
Λ	diagonal eigenvalue matrix	
λ	eigenvalue in the Cartesian flux equation	
μ	molecular viscosity	kg/(ms)
μ_ϵ	diffusion coefficient of ϵ	kg/(ms)
μ_k	diffusion coefficient of k	kg/(ms)
ω	total pressure loss	
π	pressure ratio	
ρ	density	kg/m^3
σ_ϵ	coefficient in $k-\epsilon$ turbulence model	
σ_k	coefficient in $k-\epsilon$ turbulence model	
τ	shear stress	N/m^2
θ	wake angle	$^\circ$

Subscripts

ax	axial
s	isentropic
$\mathrm{t-s}$	total to static
t	total state
v	viscous
w	wall
$\mathrm{x}, \mathrm{y}, \mathrm{z}$	x-, y-, z-direction
T	turbulent
1	turbine inlet, stator inlet
2	rotor inlet, stator outlet

3 rotor outlet, second stage stator inlet

4 diffuser outlet, second stage stator outlet or rotor inlet

5 second stage rotor outlet

des design value

is isentropic

t tangential

x axial

Superscripts

$*$ throat

$,,$ fluctuating component

$-$ averaged quantity

$\hat{}$ convective value

$\vec{}$ vector

k index in the Cartesian form of the flux equation

l left side

r right side

Dimensionless numbers

M Mach number

Pr Prandtl number

Re_{T} turbulent Reynolds number

Abbreviations

ASME American Society of Mechanical Engineers

AVDR Axial Velocity Density Ratio

CFD Computational Fluid Dynamics

CO Coupled approximation

DDADI Diagonally Dominant Alternating Direction Implicit

DLR German Aerospace Center

EGV Exit Guide Vane

FEM Finite Element Method

LES Large Eddy Simulation

LUT Lappeenranta University of Technology

MUSCL Monotonic Upwind Schemes for Conservation Laws

ORC Organic Rankine Cycle

RNG Reynolds Renormalization Group

TA Turbine Alone approximation

TKK Helsinki University of Technology

UN Uncoupled approximation

1 Introduction

The laboratory of Fluid Dynamics at Lappeenranta University of Technology has nearly thirty years of experience in high speed electric motor and turbomachine technology. During the years, several turbines and compressors with high rotating speeds have been designed and studied in detail. Several dissertations in the field of high speed technology have been published, many of them comprising both numerical and experimental studies. The work presented in this thesis is a continuation of this tradition and expertise.

The drive towards lower emissions in the field of larger diesel engines promotes more efficient turbocharger designs. There is a trend of increasing the turbocharger pressure ratio. Limited space can be one design constraint and with high pressure ratios the flow becomes relatively easily supersonic if only one turbine stage is used. One answer to these requirements is the use of a supersonic axial turbine. This turbine type can be designed in smaller size compared to subsonic design of the same power. Costs of producing only one turbine stage are also lower than the costs of producing two turbine stages. Usually supersonic turbines have low degree of reaction which leads to lower axial forces to be compensated with bearings compared to high reaction turbines.

Supersonic axial turbines are used in space rocket turbo pumps to rotate the pump feeding fuel or oxygen to the combustion chamber. Another place where supersonic turbines are used is the Curtis stage of an industrial turbine. These turbines are usually impulse type turbines, where the pressure drop happens in the stator and the flow velocity at the stator outlet is very high. In the rotor, the torque comes from changes in the direction of the velocity vector without any pressure drop.

Usually supersonic turbine stages work with lower efficiencies than subsonic turbine stages. In this study, a new idea of employing a supersonic turbine with 15 per cent of reaction to a turbocharger application is modelled with computational fluid dynamics (CFD). The effect of changing the distance between the turbine stator trailing edge and rotor leading edge is studied in both design and off-design conditions using the quasi-steady modelling approach. Additionally, the turbine stator is studied with pulsatile inlet flow, which is typical for a pulse-charged engine, by time-accurate CFD.

A literature review for the current state of research is presented in chapter 2. This is followed by describing the studied turbine geometry and measurement setup for the turbine and introducing the numerical methods used in this study in chapters 3 and 4, respectively. In chapter 5 the numerical accuracy is discussed. Later in

the chapter, the code performance is validated against measured transonic cascade results. Also the analytical and numerical results of the stator trailing edge shock wave angle are compared. In chapter 6, the results of turbine modelling under design and off-design conditions are presented with conclusions and discussion. Five different axial distances are modelled at the design conditions and three at off-design conditions. Measured efficiency is compared with calculated efficiency to increase the reliability of the modelling. This is followed by the modelling of the turbine stator with pulsatile inlet conditions. Chapter 7 contains a summary of the study, recommendations, and suggestions for further research.

The objectives of the study can be divided in three parts:

- To study the effect of stator-rotor axial distance on the studied supersonic turbine type and to improve the efficiency of the turbine in the design conditions.
- To study the effect of stator-rotor axial distance on the studied supersonic turbine type and to improve the efficiency in the off-design conditions.
- To study the effect of pulsating inlet flow into the flow field and the performance of a supersonic axial turbine stator.

The literature review has been done solely by the author. All numerical modelling presented in this study has been performed by the author, including preprocessing, numerical modelling and post processing. Part of the post processing has been performed with an in-house developed program that has been modified for the current study by the author. The results of Jeong et al. (2006) in figure 6.2 have not been modelled by the author. The measurements presented in the study have not been made by the author. The measurements for the studied turbocharger turbine have been re-designed by the author.

The scientific contribution of this work can be divided in two parts; the use of a low reaction supersonic axial turbine in a turbocharger and its modelling in design and off-design conditions with variating stator-rotor axial distances, and time-accurate modelling of a supersonic stator with pulsatile inlet flow.

2 Literature review

2.1 Supersonic turbines

The stators of supersonic turbines have subsonic inlet conditions and supersonic outlet conditions. The flow is considered to be supersonic when the free-stream Mach number is greater than 1.3. Supersonic turbines differ from subsonic and transonic turbines particularly in the stator profile. A Laval nozzle, originally invented by Carl G. P. de Laval, is designed between two stator blades and it can be handled in three parts, as shown in figure 2.1. These parts are: 1) a subsonic converging inlet section, *) a sonic throat and 2) a symmetrical supersonic diverging outlet section. Most attention has to be paid to the design of the diverging section. Figure 2.1 also shows the throat flow angle α^*, which is defined to start from the axial direction in this study. After the diverging section, the blade suction surface profile can be straight or slightly curved.

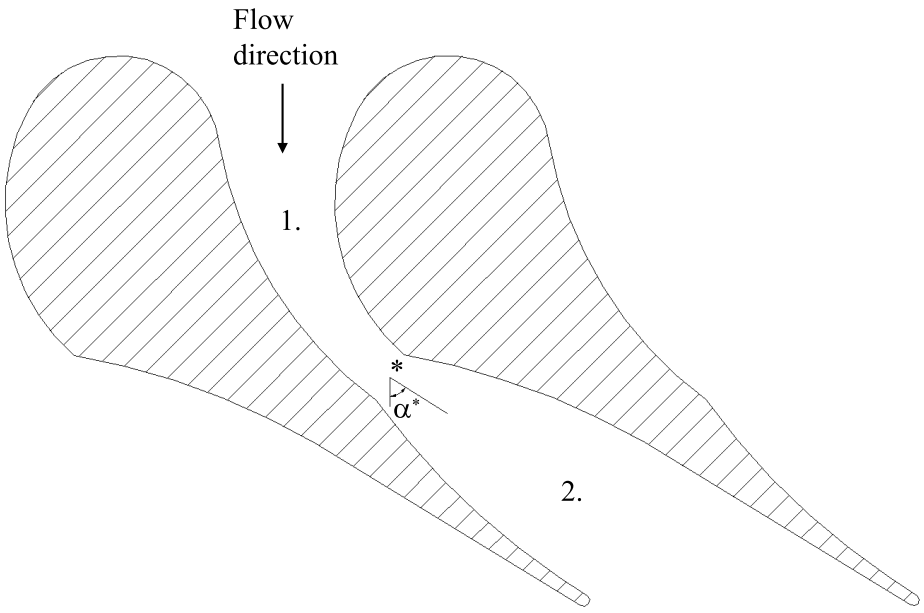

Figure 2.1: An example of a supersonic stator design with the Laval nozzle between two vanes. Shown in figure are 1) a subsonic converging section, a sonic throat, α^* throat flow angle, and 2) a supersonic diverging section.*

Supersonic turbines can produce high specific powers because of high pressure ratios and they can therefore be smaller than subsonic turbines producing the same amount of power. The efficiencies are typically relatively low, even less than 50% as shown in Dorney et al. (2000b) and Dorney et al. (2002a). One reason for the

lower efficiency is the occurrence of shock waves. More generally shock waves can e.g. cause flow separation in the blade passages when they interact with the blade surfaces. Since supersonic axial turbines typically work with low degree of reaction the axial force that is compensated by the bearings is lower than with high reaction turbines.

Supersonic stator nozzles are used also in radial turbines. Supersonic radial inflow turbines have been used in Organic Rankine Cycle (ORC) power plants and several studies concerning this turbine type have been made, see e.g. Hoffren et al. (2002), Turunen-Saaresti et al. (2006) and Harinck et al. (2010). A study that partly considers the design of a supersonic radial turbine nozzle has been made by Reichert and Simon (1997).

Supersonic axial turbine-stages are typically used in industrial steam turbines for controlling purposes, and are then called Curtis-stages. An example of the velocity triangles of a Curtis-stage is shown in figure 2.2. Another application is a turbo pump turbine, where a supersonic turbine is used to rotate a pump that pumps oxygen or fuel to the combustion chamber of a space rocket engine.

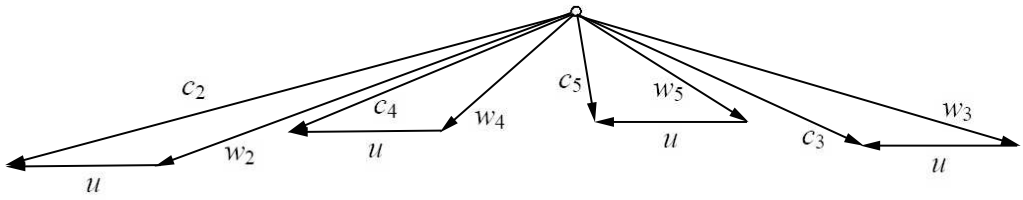

Figure 2.2: An example of the velocity triangles of a Curtis turbine stage (Traupel (1977)).

Andersson et al. (1998) have made experiments on an axial two-stage supersonic/ transonic turbo pump turbine. They found good agreement between CFD and measurements in predicting the performance and pressure distribution. The calculated flow angle at the second rotor outlet differed from the measured one, especially for the areas close to the shroud. In a recent paper by Groth et al. (2010), flutter limits of a supersonic 1.5 stage axial space turbine has been studied both experimentally and numerically. Motion of the in-passage normal shock is seen to be the driving mechanism for the flutter type in their study.

Andersson (2007) has studied the impact of tolerances on supersonic axial turbine performance by testing several variables and their effect to the efficiency and fluid turning. Blade stagger was identified as the most significant driver of efficiency, but also large leading and trailing edge radii caused clear deterioration in perfor-

mance. Improvements in the fluid turning due to a larger blade, were concluded to be caused by the larger area for the work extraction.

Dorney et al. (2000b) have studied the effects of tip clearance in an one stage supersonic axial turbine numerically. The turbine rotated 31300 rpm, and the ratio of rotor exit static pressure to stator inlet total pressure was 0.1875. The operating gas was air with the specific heat ratio of $\gamma = 0.13537$. They did two simulations, the first with the tip clearance of 2.5 per cent of span and the second without tip clearance. The rotor blades in the second simulation were extended 2.5 per cent to the spanwise direction, compared to the case with tip clearance. The total-to-static efficiency was slightly higher (0.479) when tip clearance was included than without tip clearance (0.470). Significant unsteadiness was observed in the rotor pressure surface close to leading edge at 60 per cent span in both simulations at blade passing and twice the blade passing frequencies. Dorney et al. (2000b) conclude that the improved efficiency was due to 1) unloading of the rotor tip region, which reduced secondary losses, 2) weakened shock system in the stator and rotor, and 3) the losses generated by the tip clearance were smaller than the additional losses generated by the stronger expansion wave/shock system in the second case.

Dorney et al. (2000a) have studied the effect of different simulation approximations for a supersonic axial turbine. The nozzle exit Mach number was 2.13, and rotational speed 20000 rpm. Rocket fuel RP1 was considered as the working fluid. The modelling was done with three different approximations. Two of the approximations were uncoupled (TA and UN) and the third was a coupled approximation (CO). Dorney et al. (2000a) found out that when the nozzle, the rotor and the exit guide vane were modelled coupled and simultaneously, the turbine power (869 kW) was closest to the experiments (895 kW). With the other two modelling approximations TA (733 kW) and UN (796 kW) power was significantly underpredicted. Interaction between the nozzle and the turbine was underpredicted when the simulation was uncoupled (UN). The efficiency of the coupled simulation was slightly lower (61.2$\%$) than in the uncoupled simulations (62.5 and 62.8$\%$), owing to the interaction between the nozzle and the turbine created losses. They conclude that the flow fields of the nozzle and rotor should be solved simultaneously and coupled in order to predict the unsteadiness generated by the nozzle/rotor interaction accurately.

In the paper by Dorney et al. (2002b), the effects of the first stage supersonic turbine stator endwall geometry and stacking in a two-stage supersonic turbine have been studied numerically. A flow separation region was found in the hub between the first stage stator and the rotor. Dorney et al. (2002b) managed to decrease the separated region by re-stacking the first stage stator along the radial line con-

necting the trailing edge instead of the stacking stator vanes along the center of gravity. This led to significantly improved performance. Different stator endwall geometries had only a small effect on the flow separation or on the turbine efficiency.

In Dorney et al. (2002a) the effect of variable specific heat on the flow in a supersonic turbine has been studied numerically. The rotational speed was 31300 rpm, and the stator outlet Mach number varied between 1.41 and 1.52. Time-averaged Navier-Stokes simulations showed small decrease in the total-to-total (60.8 and 60.2%) and total-to-static efficiencies (44.9 and 44.7%) when variable specific heat was used. When Fourier decompositions of unsteady pressure traces in the rotor (10% span, near the leading edge) were examined, it was seen that the greatest difference between variable and constant specific heat in unsteadiness was at the vane passing frequency. Also the highest unsteadiness was at that frequency. Dorney et al. (2002a) conclude that the variable specific heat should be included in CFD calculations.

Dorney et al. (2004) have studied the effect of full and partial admission for supersonic turbines. They made unsteady time-accurate calculations for two geometries. The nozzle exit Mach number was 1.06 in full and 1.39 in partial admission. The calculated total-to-total efficiencies for full and partial admissions were 63.3 and 50.4 per cent, respectively. According to the full admission calculations, the unsteadiness on the rotor suction surface was greatest at the nozzle-passing frequency. Also significant unsteadiness was observed at the pressure surface and at the trailing edge when the frequency was twice or once the nozzle-passing frequency. In partial admission, the dominant unsteadiness when the rotor was in the nozzle jet was at the nozzle-passing frequency, and moderate unsteadiness was observed at twice the rotor-passing frequency. Subsonic areas in the nozzle exit generated force peaks for the rotor in full admission.

Rashid et al. (2006) have studied the effect of nozzle-rotor interaction in a Curtis turbine stage. The actual flow path in the rotor was shown to be smaller than the designed geometry. The transition into a smaller (narrower) flow path was seen to begin in the last covered portion of the nozzle. Also time-accurate CFD calculations were run, and they showed similar flow separation on the rotor suction surface as seen by the authors in the dirt pattern during a field inspection. Similar impingement of separated flow into the adjacent blade pressure surface was seen in the simulations as observed in the dirt and wear patterns.

2.2 Effect of axial spacing on axial flow turbines

A moderate amount of studies have been made to understand the effect of axial spacing of subsonic and supersonic turbines. There seems to be no clear agreement of the shape of the efficiency curve as a function of axial spacing. Relatively often the trend is that the efficiency drops when the axial gap increases, but this is not the case every time. Also, the current data only covers subsonic turbines and impulse-type supersonic turbines. The schematic figure 2.3 shows the idea of changing the axial spacing (gap) in an axial flow turbine. In figure 2.3 (a), a configuration with a nominal gap is shown, and in figure 2.3 (b), an increased axial gap is seen between the stator and the rotor. The increasing of the axial gap has been made by changing the position of the rotor downstream from the stator.

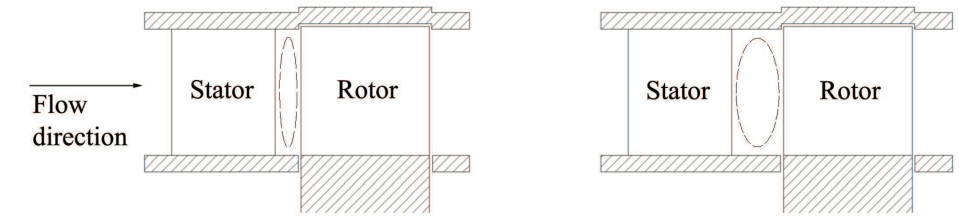

Figure 2.3: Schematic figure of two different axial gaps in an axial flow turbine: a nominal axial gap (a) and an increased axial gap (b). Axial gap is shown as broken ellipse between stator and rotor.

There also seems to be a lack of studies about the effect of axial gap variation in off-design conditions. Yamada et al. (2009) have studied the effect of axial gap on secondary flows and aerodynamic performance in both design and off-design conditions. They made time-accurate numerical and experimental studies with a one-stage axial flow turbine having the rotating speed of 1650 rpm at design and 1300 rpm at off-design conditions. At the off-design conditions, a relatively linear efficiency decrement was seen when the axial gap increased, but at design conditions the results showed increment in the efficiency when the axial gap was changed from the smallest to the second smallest. Yamada et al. (2009) conclude that the higher off-design stage performance was achieved because large passage vortices were generated in the rotor to be suppressed by the stator wake interaction. The non-linear efficiency behaviour at design conditions was seen to be due to less beneficial wake interaction near the tip, which reduced the positive interaction near the hub.

Funazaki et al. (2007) have studied the effect of an axial gap between the stator and rotor on the performance of a subsonic axial turbine numerically and experimentally. Three different axial gap configurations, normalized with the stator axial chord length (0.255, 0.383 and 0.510), were used. A decrease of the axial gap increased the turbine efficiency. The stator exit flow angle (rotor incidence) increased when the axial gap was increased. This increase of rotor incidence increased the rotor wake width. A longer axial gap increased the wall (hub and shroud) boundary layer thickness before the rotor blade, and this was considered to be the source of high entropy areas at the hub and shroud at the rotor outlet.

Changing the axial gap has an effect on the blade excitation, but the effect is not always the same. Jöcker (2002) has studied the effect of axial gap into blade vibration excitation of different axial turbines numerically. A decrease of the axial gap decreased the aerodynamic excitation, but it was concluded that the behaviour is not necessarily always similar.

Usually supersonic turbines are impulse stages where the expansion takes place in the stator. Jeong et al. (2006) have studied the effect of stator-rotor axial clearances, and their numerical and experimental studies confirm that the efficiency of a supersonic impulse turbine increases by decreasing the clearance. They conclude that the decrease in efficiency is caused by the increase in total pressure loss in the region between the stator and rotor.

Griffin and Dorney (2000) have made time-accurate CFD simulations on a one-stage supersonic axial turbine with exit guide vanes (EGV). The pressure unsteadiness was found to be relatively high at the blade passing frequency and at its second harmonic. The unsteadiness was highest on the leading edge, but was decreased with a larger axial gap between the stator and rotor. The power was predicted to be greater when the axial gap was smaller. When the axial gap was larger, additional losses were caused by nozzle jet interaction between successive nozzles. The nozzle wake was shown to cause both earlier separation on the blade suction surface and separation on the EGV pressure surface. Also the effect of calculating the stator separately and giving the results for the inlet state for the rotor was studied. The simulation showed that the results were not similar, simulation of the stator separately underpredicted flow separation and losses. Also the mixing between the stator and rotor was not properly modelled.

Sadovnichiy et al. (2009) have studied the effect of the axial gap on the performance of an impulse turbine. They found that, for the leaned-twisted stage, the efficiency was decreased when the axial gap was increased, but for the radial-twisted stage there was no decrease in efficiency. Increasing the axial gap reduced

the downward curvature of the streamlines, and this way the aerodynamic resistance was decreased and the amount of leakage over the sealing was increased. This phenomenon was only seen in the leaned-twisted stage.

Denos et al. (2001) have made numerical and experimental studies for a transonic axial turbine stage having a fluctuating relative rotor inlet total pressure. Largest pressure fluctuations at the rotor blade surface were detected at the leading edge region. Denos et al. (2001) report that a noticeable decrease in fluctuation amplitudes was observed in the rotor leading edge region when the axial gap was increased from 0.35 to 0.5 of the stator axial chord. This was probably due to a strong shock intensity decrease with the increasing axial gap.

In the first part of their two-part study Gaetani et al. (2006a) made time-averaged measurements with a high pressure axial turbine stage. Two axial gaps were measured, and detailed flow fields were presented. The overall mass averaged efficiency of the turbine decreased from 0.83 to 0.79 when the axial gap was increased from the nominal value of 0.35 stator axial chord to 1.0 stator axial chord. For the larger axial gap, the traces of the stator vortex structures vanished downstream of the rotor.

In the second part of their study, Gaetani et al. (2006b) made time-accurate measurements with a high pressure axial turbine stage. Two axial gaps, similar to the first part, were used. In the tip region, where the stator-rotor interaction was low, increasing the axial gap induced higher losses, but at the hub region the behaviour was opposite. When the maximum axial gap was used, the flow field downstream of the rotor was seen to be mainly dominated by the rotor effects.

Venable et al. (1999) have made time-averaged numerical and experimental studies for the effect of stator-rotor spacing on the performance and aerodynamics of a transonic axial turbine stage. They found that axial spacing had a negligible effect on the time-averaged surface pressures, whereas the decrease of the axial gap increased the unsteadiness of surface pressures. They also found that when the axial gap decreased, the stage adiabatic total pressure drop increased. A tendency of slight adiabatic efficiency increase was reported when the axial gap increased.

Busby et al. (1999) have made time-resolved analysis for the influence of stator-rotor spacing on transonic turbine stage aerodynamics, presented in Part II of a paper by Venable et al. (1999). A detailed description of stator-rotor interaction during one stator-passing period is given. According to the authors the decreased stator losses when the axial gap was decreased were due to a stronger stator-rotor interaction and wake mixing loss reduction. The increase in rotor blade relative

total pressure loss, when the axial gap decreased, was seen to be mainly due to increased stator wake/rotor blade interaction.

2.3 Turbine in a turbocharger

Small turbocharger turbine designs are usually based on radial or mixed-flow type when they are connected to small engines, such as car or truck engines. In large marine diesel engines, axial turbines are mostly used. Most of the studies concerning turbocharger turbines have been made of radial or mixed flow turbines.

Several studies of one-dimensional turbocharger turbine modelling have been made. Costall et al. (2006) have studied the importance of unsteady effects by comparing calculated one-dimensional results with experimental results for a mixed flow turbine. Another one-dimensional study has been made by Ghasemi et al. (2002), who have modelled a twin-entry turbine in partial admission and steady state conditions.

The inlet flow in a turbocharger turbine is unsteady by nature, and the flow quantities such as mass flow, pressure and temperature fluctuate highly as a function of time. An example of mass flow fluctuation is shown in figure 2.4.

When using pulse charging, a hysteresis behaviour can be seen when the mass flow and the expansion ratio (turbine inlet stagnation pressure divided by turbine exit static pressure) are plotted. This behaviour arises from the fluctuating inlet conditions. When comparing the steady state conditions to the unsteady pulsating conditions, the actual performance can differ in some areas quite a lot from the steady state. A schematic presentation of this behaviour is given in figure 2.5. The real turbine performance and flow characteristics differ from the steady state, as mentioned by Karamanis and Martinez-Botas (2002). Although an increase in the pulsating frequency seems to move the hysteresis shape of the curve closer to the steady state curve, as shown by Karamanis and Martinez-Botas (2002) and Hakeem et al. (2007).

In an early study of Daneshyar et al. (1969), three axial flow turbines were tested under steady and pulsatile flow conditions. The tested turbines were one-stage turbines with different degrees of reaction. They found that the turbine having the highest degree of reaction had the best efficiency under both steady and pulsatile conditions.

In a paper of Filsinger et al. (2001), a pulse-charged turbocharger axial turbine is

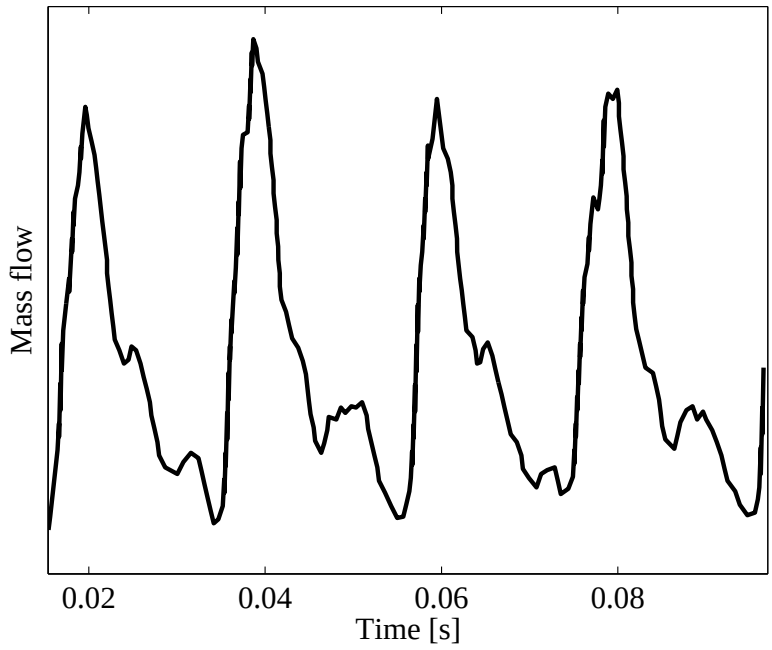

Figure 2.4: Mass flow fluctuation as a function of time at the turbocharger turbine inlet according to real engine simulation by Matlab/GT-Power, Honkatukia (2006).

modelled using CFD. The flow over the rotor is very different from the designed one when the rotor is under pulsating conditions. In another CFD study Schäfer (2002), two axial turbocharger turbines are modelled. The amplitude of static pressure pulsation decrease from 4 bar at the inlet to 0.5 bar at the gas exhaust casing inlet. Filsinger et al. (2002) have made coupled CFD-FEM studies for an axial turbocharger turbine with pulsating inlet total pressure and temperature.

Rajoo and Martinez-Botas (2007) have studied the effect of pulsating flow for a vaned mixed flow turbocharger turbine experimentally. The rotating speed of the turbine was 48000 rpm and it was tested in 40 Hz and 60 Hz pulsating inlet flow frequencies, and also unsteady behaviour for nozzle angles between 40° and 70° were tested. The highest steady state efficiency (80%) was reached at vane angles between 60° and 65°. Rajoo and Martinez-Botas (2007) found that the nozzle damped the upstream flow fluctuation. Instantaneous efficiency proved to be inaccurate as point-by-point calculation. Comparing the cycle averaged power, to deduce the cycle averaged efficiency was proposed to be one solution for the efficiency calculation problem. This produced satisfactory results in some cases, but there were also major differences between the cycle-averaged and quasi-steady efficiencies, such as 82.2 and 58.5% at the 60 Hz condition, respectively.

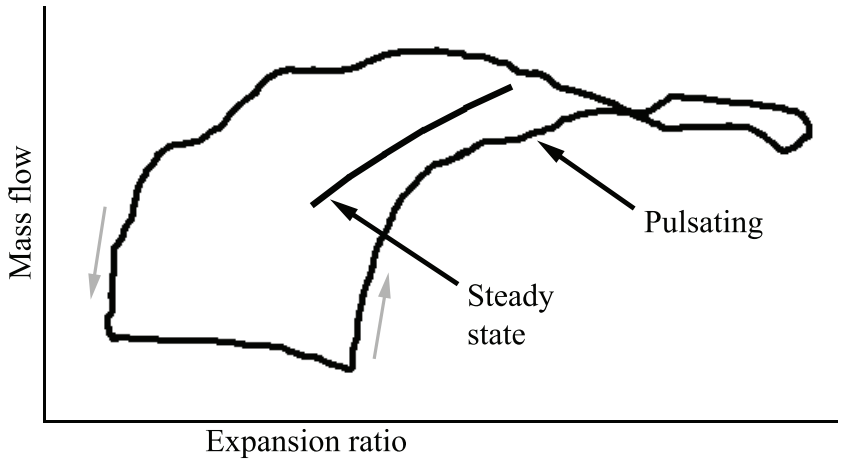

Figure 2.5: Schematic comparison of the mixed flow turbine expansion ratio as a function of mass flow on the steady state (Steady state) and pulsating inlet conditions (Pulsating). Turbine performance under pulsating inlet conditions makes a hysteresis-like loop around the steady state curve. The figure follows the shape presented in Hakeem et al. (2007). Gray arrows indicate the direction of the hysteresis cycle.

Lam et al. (2002) have made time-accurate CFD modelling for a vaned turbocharger turbine with pulsating inlet conditions. The turbine was first modelled with constant flow conditions, and it was found to be quite close to the experimental results. There was approximately 11% difference in the average mass flow between the steady and unsteady calculations due to poor convergence. Pulse smoothing was seen in the volute, which should be taken into consideration when the unsteady response of a turbine is modelled. The lowest rotor efficiency was seen when the available power was greatest. The rotor peak-to-peak efficiency differed 5% from the mean average value. There were indications that flow unsteadiness does not affect the rotor efficiency significantly.

Hellström and Fuchs (2008) have conducted unsteady modelling for a radial turbine with pulsating inlet flow. They modelled the turbine with pulsatile and non-pulsatile condition. Turbulence was modelled using Large eddy simulation (LES) in pulsatile conditions. They found that the turbine can not be treated as quasi-stationary if the flow is pulsatile. This is due to the inertia of the system and the flow detachment from the rotor suction surface during the acceleration phase. Also a non-constant phase shift during the pulse was seen between the pressure, mass flow and shaft power. A hysteresis type behaviour was seen when the shaft power was plotted as a function of inlet mass flow.

Ijichi et al. (1998) have conducted experimental studies of two high expansion

ratio single stage axial turbines, designed for a marine turbocharger. The original turbine was designed with a constant nozzle exit angle and the improved turbine with a controlled vortex design. The designed total-to-static pressure ratio was 3.35, and the rotational speed was 17700 rpm. In the rig tests, turbine peak efficiency of around 87 per cent was obtained. The partial load performance improved when the controlled vortex design method was applied instead of the original constant nozzle exit angle design. The full scale turbocharger tests showed almost similar characteristics as the rig tests.

Hakeem et al. (2007) have studied the effects of pulsating inflow and volute geometry for mixed flow turbines experimentally. They found that the volute geometry possibly plays a critical role in the overall mixed-flow turbine performance. When the pulsating instantaneous inlet static pressure was studied, they found that there were several peaks in the pressure pulse with 60 Hz pulse frequency compared to one peak with 40 Hz pulse frequency. This was due to back-and-forth reflections of the pressure waves from the turbine. The pressure difference during one pulse decreased when the pulse frequency was increased from 40 Hz to 60 Hz. Similar behaviour was also noticed with the instantaneous mass flow rate, rotational speed and turbine fluctuating torque. When the mass flow parameter was plotted against the expansion ratio, the ”hysteresis like” loop shrank towards the steady state curve with the higher 60 Hz pulse frequency. Hakeem et al. (2007) conclude that the cycle-mean efficiency is always higher than the corresponding steady-state efficiency and it is pronounced at a lower pulse frequency. The cycle-mean value of instantaneous inlet static pressure was higher than the steady state pressure value with both 50 and 70 per cent equivalent design speeds.

Karamanis and Martinez-Botas (2002) have made experimental studies of a single inlet mixed flow turbine. A mixed flow turbine had peak efficiency at a lower velocity ratio than a radial turbine, which confirmed that a mixed flow turbine can utilize a higher pressure ratio better than a radial turbine. Also the efficiency curves were seen to be flatter than with radial turbines. It was shown that ignoring the pulsating exit pressure can have a significant effect on the estimation of expansion ratios. It was also shown that pulsation from the engine propagates close to the speed of sound, and that the area enclosed by the hysteresis loop was reduced when the air pulse frequency increased, which indicated that the flow conditions in the turbine became closer to the steady state.

Palfreyman and Martinez-Botas (2005) have made computational studies of a vaneless single inlet mixed flow turbine and compared the flow field and performance values with measured ones. An RNG $k - \epsilon$ turbulence model and standard wall functions were used. They were able to model the hysteresis in the flow dur-

ing a pulse period and conclude that the numerical results agree reasonably with the experiment. The pressure ratio differed from measured values due to the use of time constant pressure in the exit boundary and having the trailing edge close to the boundary, which caused exit pressure dampening. Pressure fluctuation traces in the leading edge and inducer were observed to follow the inlet pressure, although at a lower pressure level. Small perturbations caused by the blade passing the monitoring location, were seen in the leading edge. Also additional perturbations were observed in the inducer region, caused by the blade passing the volute tongue. In the exducer, the pressure trace was seen to be relatively flat during one pulse period, being influenced by the exit pressure damping. The computational results also revealed that in the low pressure region during one pulse, the blade loading was lost across the blade surface. Poor flow guidance was indicated in the turbine inlet and exit. The flow velocity in the turbine exit was also observed to be influenced by the pulsation.

3 Studied turbine geometry

The turbine geometry has been designed for a turbocharger application, and it has been constructed and run in real engine tests. The original design process of the turbine has been performed by Grönman (2006). The real turbine stator and rotor are shown in figure 3.1 and a 3-D model in figure 3.2.

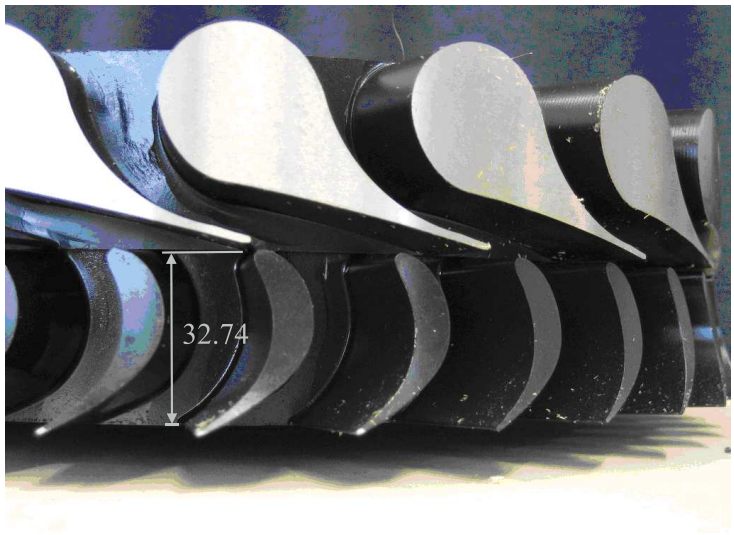

Figure 3.1: Top view of the modelled turbine stator and rotor. Photo taken by Teemu Turunen-Saaresti.

The specifications and design operating conditions of the studied turbine are shown in table 3.1. The presented design conditions are from the one-dimensional design of the turbine. The turbine has a constant stator outlet flow angle and supersonic outlet Mach number. The relative velocity entering the rotor is designed to be subsonic, and the rotor inlet flow angle is constant. The rotor outlet flow is designed to be axial. The measurement planes and geometry definitions are shown in figures 3.3 (a) and (b). Measurement plane 4 at the diffuser outlet is not shown in the figures.

3.1 Experimental setup

The studied turbine is run with flue gas by a four-stroke diesel engine with six cylinders. During the test run, the turbocharger is accelerated electrically in several steps to desired rotating speed and measurements are taken. The turbine has two connection pipes to the engine (one for three cylinders), and the temperature

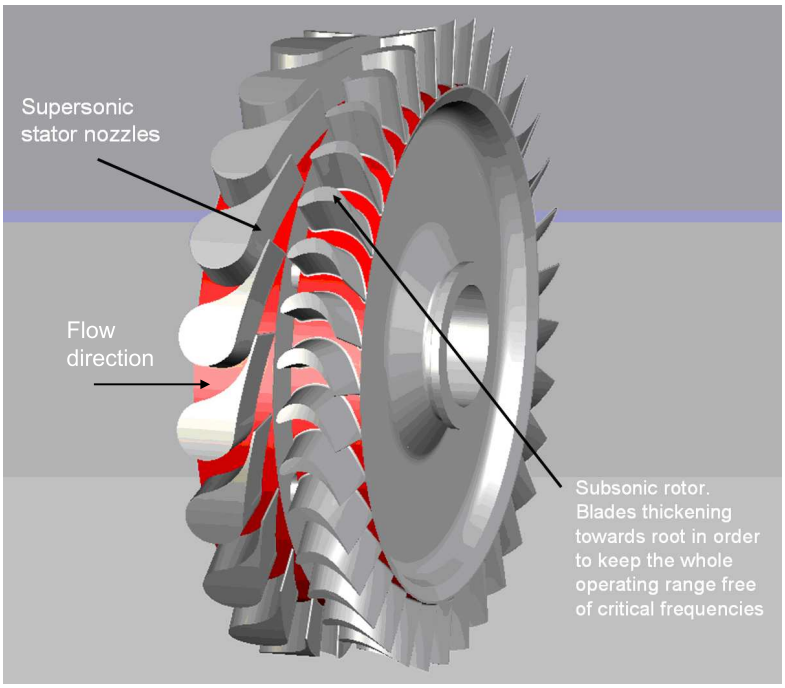

Figure 3.2: The modelled turbine stator and rotor, Larjola et al. (2009).

Table 3.1: Specifications of the studied turbine.

Number of stator blades	20
Number of rotor blades	35
Designed meanline degree of reaction	0.15
Pressure ratio	5.6
Design rotating speed [rpm]	31500
Design stator outlet absolute Mach number	1.41
Design stator outlet absolute flow angle [°]	78
Design rotor outlet absolute flow angle [°]	0
Stator axial chord at the hub [mm]	37.40
Rotor axial chord at the hub [mm]	32.74
Stator blade height [mm]	22.87
Average rotor blade height, b_{rotor}, [mm]	26.77

before the turbine is measured with two Pt100 sensors (one for each pipe). The temperature measurement setup (T) at the turbine inlet is shown in figure 3.4 (a). The temperature between the turbine stator and rotor is measured with one Pt100 sensor. Also four Pt100 sensors are used to measure the temperature after the

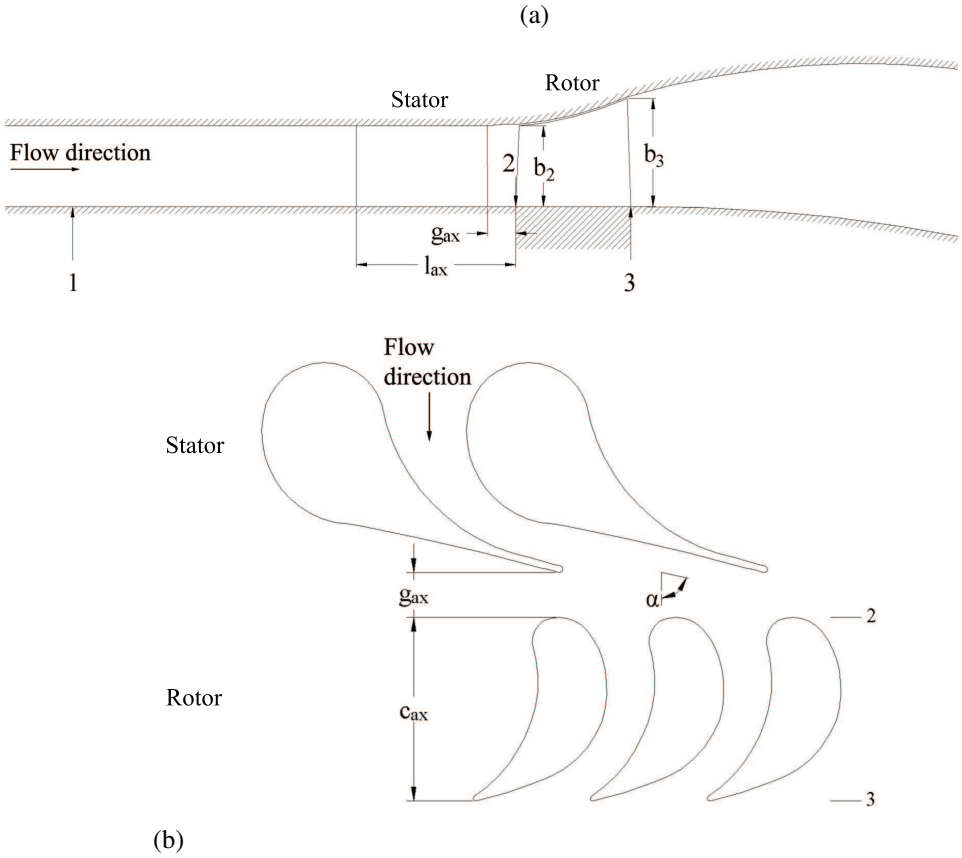

Figure 3.3: Definitions of the studied turbine geometry and measurement planes, (a) side view and (b) top view (hub).

turbine. The positions of the temperature measurements (T) after the turbine are shown in figure 3.4 (b).

Static pressure before the turbine is measured from the connection pipes between the engine and the turbine (two pipes and one measurement for each pipe). These measurements (p) are shown in figure 3.4 (a). Also the static pressure between the stator and rotor is measured. The pressure measurements are made by pressure taps. The pressure after the turbine is measured manually with a manometer. The position of this measurement (p) is shown in figure 3.4 (b).

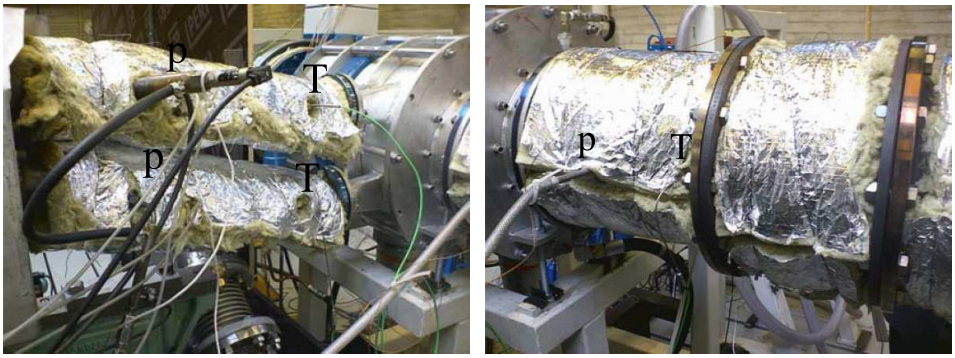

(a) (b)

Figure 3.4: Experimental setup of the turbocharger tests with a diesel engine. Measurement setup (a) at the turbine inlet and (b) at the turbine outlet, Larjola et al. (2009).

4 Numerical procedure

A CFD-code called Finflo is used in this study. This code has been successfully used in both time-accurate and quasi-steady modelling of radial flow turbomachinery. Several doctoral dissertations have been made by using Finflo. Turunen-Saaresti (2004) has made quasi-steady and time-accurate calculations on a high-speed centrifugal compressor. Quasi-steady modelling of a high speed centrifugal compressor has recently been made by Jaatinen (2009) and earlier by Tang (2006) and Reunanen (2001). Supersonic real gas flow on a ORC-turbine nozzle has been modelled in several papers including, for example Hoffren et al. (2002), Turunen-Saaresti et al. (2006), Tang (2006), and Harinck et al. (2010).

4.1 Numerical code

Finflo is a multi-grid Navier-Stokes solver that employs the finite-volume method for spatial discretization. In this study the code uses constant specific heat capacity at constant pressure. The code was originally developed at Helsinki University of Technology (TKK). The development was started in 1987, and some development work has been made later in the Laboratory of Fluid Dynamics at Lappeenranta University of Technology. Finflo is written in the FORTRAN programming language. In this study the fluid is modelled as ideal gas, but the code is also capable of modelling real gas flows (Tang (2006)).

Finflo can calculate at an unlimited number of grid levels, which means that when using the second grid level, every second node is removed from the original calculation domain. When calculating at the first grid level, all nodes of the grid are included. In this study, all the numerical results presented in chapter 6 have been calculated at first grid level after being initialized from second grid level results (which were not fully converged). In chapter 5, two grid dependency tests have been calculated at the second grid level until convergence whereas other cases are calculated in the first grid level after being initialized from the second grid level results.

4.1.1 Governing equations

The Reynolds averaged Navier-Stokes (RANS) and the equations describing the turbulent kinetic energy k and the dissipation of turbulent kinetic energy ϵ can be written in conservative form as

$$\frac{\partial U}{\partial t} + \frac{\partial (F - F_{\mathrm{v}})}{\partial x} + \frac{\partial (G - G_{\mathrm{v}})}{\partial y} + \frac{\partial (H - H_{\mathrm{v}})}{\partial z} = Q \tag{4.1}$$

where $U = (\rho, \rho u, \rho v, \rho w, E, \rho k, \rho \epsilon)^T$ and the inviscid fluxes F, G and H are defined as

$$F = \begin{pmatrix} \rho u \\ \rho u^2 + p + \frac{2}{3}\rho k \\ \rho v u \\ \rho w u \\ (E + p + \frac{2}{3}\rho k)u \\ \rho u k \\ \rho u \epsilon \end{pmatrix} G = \begin{pmatrix} \rho v \\ \rho u v \\ \rho v^2 + p + \frac{2}{3}\rho k \\ \rho w v \\ (E + p + \frac{2}{3}\rho k)v \\ \rho v k \\ \rho v \epsilon \end{pmatrix}$$

$$H = \begin{pmatrix} \rho w \\ \rho u w \\ \rho v w \\ \rho w^2 + p + \frac{2}{3}\rho k \\ (E + p + \frac{2}{3}\rho k)w \\ \rho w k \\ \rho w \epsilon \end{pmatrix} \tag{4.2}$$

where ρ is density, u, v, w are the velocities in the $x-$, $y-$ and $z-$directions, p is the pressure, Q is the source term and E is the total internal energy and is defined as

$$E = \rho e + \rho \frac{u^2 + v^2 + w^2}{2} + \rho k \tag{4.3}$$

where e is the specific internal energy. The equation of state for a perfect gas is used to calculate the pressure

$$p = \rho e(\gamma - 1) \tag{4.4}$$

where γ is the ratio of specific heats. The viscous fluxes F_v, G_v and H_v are defined as

$$F_v = \begin{pmatrix} 0 \\ \tau_{xx} \\ \tau_{xy} \\ \tau_{xz} \\ u\tau_{xx} + v\tau_{xy} + w\tau_{xz} - q_x \\ \mu_k(\frac{\partial k}{\partial x}) \\ \mu_\epsilon(\frac{\partial \epsilon}{\partial x}) \end{pmatrix} G_v = \begin{pmatrix} 0 \\ \tau_{xy} \\ \tau_{yy} \\ \tau_{yz} \\ u\tau_{xy} + v\tau_{yy} + w\tau_{yz} - q_y \\ \mu_k(\frac{\partial k}{\partial y}) \\ \mu_\epsilon(\frac{\partial \epsilon}{\partial y}) \end{pmatrix}$$

$$H_v = \begin{pmatrix} 0 \\ \tau_{xz} \\ \tau_{yz} \\ \tau_{zz} \\ u\tau_{xz} + v\tau_{yz} + w\tau_{zz} - q_z \\ \mu_k(\frac{\partial k}{\partial z}) \\ \mu_\epsilon(\frac{\partial \epsilon}{\partial z}) \end{pmatrix} \tag{4.5}$$

where q_i is the heat flux in the x-, y- and z-direction, μ_k is the diffusion coefficient of k, and μ_ϵ is the diffusion coefficient of ϵ. The viscous stress tenson τ_{ij} is defined as

$$\tau_{ij} = \mu\left[\frac{\partial u_j}{\partial x_i} + \frac{\partial u_i}{\partial x_j} - \frac{2}{3}\frac{\partial u_k}{\partial x_k}\delta_{ij}\right] - (\overline{\rho u_i'' u_j''} - \delta_{ij}\frac{2}{3}\rho k) \tag{4.6}$$

where μ is the molecular viscosity. The modelling of Reynolds stresses $\overline{\rho u_i'' u_j''}$ is described in the next chapter as part of the turbulence modelling. The Kronecker delta function δ_{ij} is defined as

$$\begin{cases} \delta_{ij} = 0 & \text{if } i \neq j \\ \delta_{ij} = 1 & \text{if } i = j \end{cases} \tag{4.7}$$

The heat flux in equation 4.5 containing laminar and turbulent part is defined as

$$\vec{q} = -(k + k_T)\nabla T = -\left(\mu\frac{c_p}{Pr} + \mu_T\frac{c_p}{Pr_T}\right)\nabla T \tag{4.8}$$

where μ_T is the turbulent viscosity and Pr is the Prandtl number. The diffusion coefficients of the turbulence quantaties and the scalar quantity are approximated in equation 4.5 as

$$\mu_k = \mu + \tfrac{\mu_T}{\sigma_k} \quad \mu_\epsilon = \mu + \tfrac{\mu_T}{\sigma_\epsilon} \tag{4.9}$$

where σ_k and σ_ϵ are coefficients in the $k-\epsilon$ turbulence model. The flow equation 4.1 is written in integral form for the finite-volume method

$$\frac{d}{dt}\int_V UdV + \int_S \vec{F}(U)\cdot d\vec{S} = \int_V QdV \tag{4.10}$$

where $\vec{F}(U)$ is the flux vector. By integrating equation 4.10 over the control volume and surface for a computational cell i, the following discrete form is achieved

$$V_i\frac{dU_i}{dt} = \sum_{faces} -S\hat{F} + V_iQ_i \tag{4.11}$$

where the sum is taken over the faces of the computational cell i. The flux $\hat{F}$ for the face is defined as

$$\hat{F} = n_xF + n_yG + n_zH \tag{4.12}$$

where n_x, n_y and n_z are the unit normal vectors in the x-, y- and z-directions, respectively. Fluxes F, G and H are defined by equations 4.2 and 4.5. The inviscid fluxes are evaluated by Roe's flux splitting method (Roe (1981))

$$\hat{F} = T^{-1}F(TU) \tag{4.13}$$

where T is a rotation matrix which transforms the variables to a local coordinate system that is normal to the cell surface. The Cartesian form F of the flux is calculated as

$$F(U^l,U^r) = \frac{1}{2}[F(U^l)+F(U^r)] - \frac{1}{2}\sum_{k=1}^{K} r^{(k)}\lambda^{(k)}\alpha^{(k)} \tag{4.14}$$

where U^l and U^r are the solution vectors on the left and right sides of the cell surface, $r^{(k)}$ is the right hand side eigenvector $A = \partial F/\partial U = R\Lambda R^{-1}$, $\lambda^{(k)}$ is the corresponding eigenvalue, and $\alpha^{(k)}$ is the corresponding characteristic variable calculated from $R^{-1}\Delta U$, where $\Delta U = U^r - U^l$.

A MUSCL-type approach is used to evaluate U^l and U^r

$$U^l_{i+1/2} = U_i + \frac{\phi(R_i)}{4}[\kappa_1(U_i - U_{i-1}) + \kappa_2(U_{i+1} - U_i)] \tag{4.15}$$

$$U^r_{i+1/2} = U_i - \frac{\phi(R_{i+1})}{4}[\kappa_2(U_{i+1} - U_i) + \kappa_1(U_{i+2} - U_{i+1})] \tag{4.16}$$

The limiter presented by van Albada et al. (1982) is used in equations 4.15 and 4.16 and is defined as

$$\phi(R) = \frac{R^2 + R}{R^2 + 1} \tag{4.17}$$

where

$$R_i = \frac{U_{i+1} - U_i}{U_i - U_{i-1}} \tag{4.18}$$

DDADI-factorization presented by Lombard et al. (1983) is used to integrate discretized equations in time. The method is based on approximate factorization and on the splitting of the Jacobians of the flux terms. The viscous fluxes are evaluated by thin-layer approximation. More detailed information about the code and used methods can be found in the User's guide by Siikonen et al. (2004).

4.2 Turbulence modelling

The $k - \epsilon$ turbulence model presented by Chien (1982) is used in this study. The model is a low Reynolds number model, which means that the non-dimensional wall distance y^+ should be close to unity in order to model the boundary layer correctly. The non-dimensional wall distance is defined as

$$y^+ = y_n \frac{\rho u_\tau}{\mu_w} = y_n \frac{\sqrt{\rho \tau_{\mathrm{w}}}}{\mu_w} \tag{4.19}$$

where y_n is the normal distance from the wall, u_τ is the friction velocity, μ_w is the molecular viscosity on the wall and τ_w is shear stress on the wall.

The Boussinesq approximation is made for the Reynolds stresses and is defined as

$$-\overline{\rho u_i'' u_j''} = \mu_T \left[\frac{\partial u_j}{\partial x_i} + \frac{\partial u_i}{\partial x_j} - \frac{2}{3} \frac{\partial u_k}{\partial x_k} \delta_{ij} \right] - \frac{2}{3} \rho k \delta_{ij} \tag{4.20}$$

The source term for the turbulence model is defined as

$$Q = \begin{pmatrix} P - \rho\epsilon - 2\mu \frac{k}{y_n^2} \\ C_1 \frac{\epsilon}{k} P - C_2 \frac{\rho \epsilon^2}{k} - 2\mu \frac{\epsilon}{y_n^2} e^{\frac{-y^+}{2}} \end{pmatrix} \tag{4.21}$$

The production of turbulent kinetic energy P is modelled by Boussinesq approximation from equation 4.20

$$P = -\overline{\rho u_i'' u_j''}\frac{\partial u_i}{\partial x_j} = \left[\mu_T(\frac{\partial u_j}{\partial x_i} + \frac{\partial u_i}{\partial x_j} - \frac{2}{3}\frac{\partial u_k}{\partial x_k}\delta_{ij}) - \frac{2}{3}\rho k\delta_{ij}\right]\frac{\partial u_i}{\partial x_j} \tag{4.22}$$

The turbulent viscosity μ_T is calculated as

$$\mu_{\mathrm{T}} = \frac{C_\mu \rho k^2}{\epsilon} \tag{4.23}$$

The empirical coefficients used in equations 4.21 and 4.23 are shown in table 4.1. The employed turbulence model differs from the one presented by Chien (1982). Coefficients C_1 and C_2 are 1.35 and 1.8 in the original paper, but in Finflo the coefficients are 1.44 and 1.92, respectively. The new coefficients are based on the most commonly used values.

Table 4.1: Empirical coefficients in Chien's $k-\epsilon$ turbulence model as used by Finflo.

C_1 = 1.44	σ_k =1.0
C_2 = 1.92	σ_ϵ =1.3
C_μ = 0.09	

4.3 Boundary conditions

At the outlet of calculation domain, constant static pressure is used as the boundary condition in all cases. This is also the case in modelling with pulsatile inlet flow, although it has been reported to influence upstream to pulsatile flow by Palfreyman and Martinez-Botas (2005). This approach has been also used by Lam et al. (2002). Momentum and total enthalpy distributions are defined as inlet boundary conditions in every calculation.

4.3.1 Pulsatile inlet model

A simple sinusoidal pulsatile inlet model is used in this study to model the pulsatile inlet mass flow typical for a turbocharger turbine in a process using pulse charging. This is not similar to real engine pulsation, but is assumed to give a good view to the effects of pulsation inside a turbine stator. The pulsation function for mass flow q_m is defined as

$$q_m = q_{m,des} + Asin(2\pi ft) \tag{4.24}$$

where A is the pulsation amplitude and f is the pulse frequency.

Mass flow pulsation as a function of time is plotted in figure 4.1. At the inlet of the computational domain total enthalpy is kept constant and momentum distribution changes as the mass flow changes. The total enthalpy is the same as the one used in the quasi-steady or time-accurate modelling of the stator. Average mass flow over one pulse is the same as the designed steady state value.

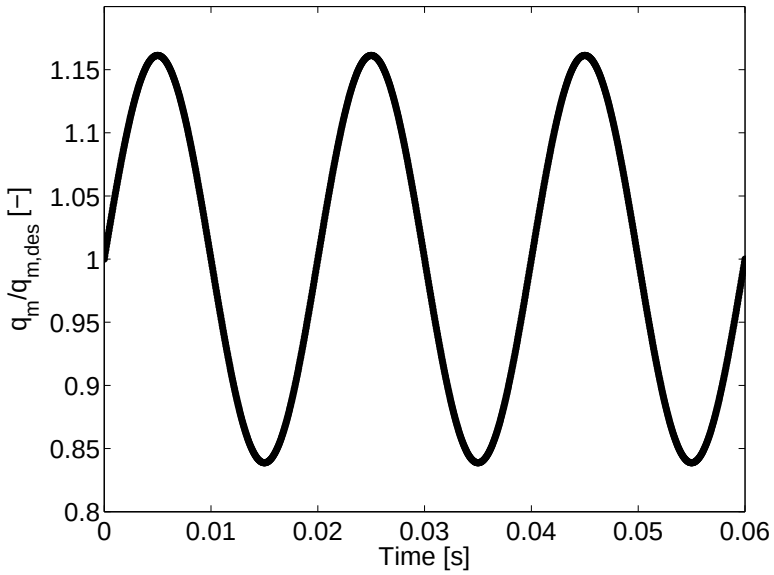

Figure 4.1: Mass flow pulsation as a function of time at the turbine inlet scaled with the design mass flow.

4.4 Modelling procedure with pulsatile inlet conditions

The modelling with pulsatile inlet conditions is done in three stages. The following procedure is used:

1. A quasi-steady modelling for the whole computational system is performed with time-averaged boundary conditions until convergence.

2. Pulsatile inlet calculation is started from the quasi-steady results using new inlet boundary conditions, which are based on the pulsatile inlet conditions.

3. In the beginning of every following time-step, new inlet boundary conditions are given to the program, based on the pulsatile inlet conditions.

The total number of 1200 time steps are used to model 0.06 seconds of stator operation. This makes the time step to be 5 μs. The number of inner iterations during each time step is determined on the basis of previous studies and following the convergence during inner iterations. In this study the number of inner iterations is 30. The same number of inner iterations is also used in the time-accurate modelling of the supersonic stator geometry in chapter 6.3. A lower number of 25 inner iterations was used by Turunen-Saaresti (2004). All time-accurate modelling (also with a pulsatile inlet) is based on a second order implicit time-integration method described by Hoffren (1992). The time-accurate simulation procedure without pulsating inlet conditions is also started from quasi-steady results, but the same inlet boundary conditions as in quasi-steady modelling are used during the whole modelling.

4.5 Convergence criteria

In this study, two of the most important convergence criteria are the mass flow difference between the inlet and outlet boundaries and the L2-norm of the density residual. In addition to these, the L2-norms of momentum in x-, y- and z-direction and energy residuals are also important. Also the effect of additional iterations is tested in some cases by checking the efficiency changes after different numbers of iteration cycles in order to be certain about convergence. An example of convergence monitoring is shown in figures 4.2 (a) and (b) for the inlet and outlet mass flow difference and L_2-norm of density residual, respectively.

4.6 Computational resources

All modelling in this study was run in two separate computers employing the LINUX operating system. Only one processor was used for each calculation. An average calculation time for the modelling of a turbine in design and off-design conditions and quasi-steady stator-only modelling are shown in table 4.2. The CPU-time for one cycle needed in time-accurate and pulsatile-inlet modelling of the stator was close to the value of quasi-steady stator modelling. Convergence was achieved before the end of calculations, but the modelling was continued to be certain about it.

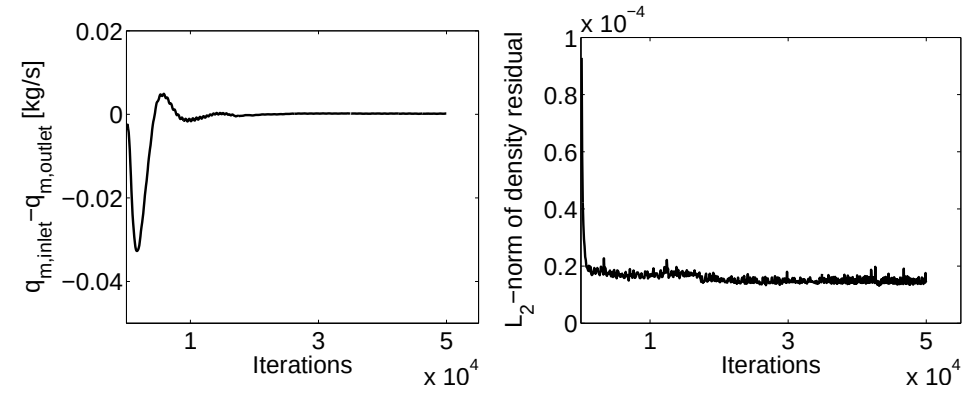

(a) (b)

Figure 4.2: Convergence history of grid 4 in the grid dependency test, the difference between inlet and outlet mass flows (a) and L_2-norm of density residual (b) as a function of iteration cycles.

Table 4.2: Average computational time needed for whole turbine modelling in design and off-design conditions. The computational time for quasi-steady stator-only modelling is presented as well.

	CPU-time / cycle	Cycles
Design	35.06	74000
Off-design	38.71	70000
Stator	5.24	50000

5 Numerical reliability

In this chapter, the reliability of the numerical modelling is evaluated, first by presenting the grid dependency study, where both effects of grid density and non-dimensional wall distance are studied in detail. This is followed by the validation study with transonic linear cascade measurements in order to have understanding of code performance when shock waves appear in the flow field. In addition to these, the capability of the code to model supersonic flow is studied by comparing the numerical and analytical results of shock wave formation at the supersonic stator trailing edge.

5.1 Grid dependency

The effect of grid density for the studied geometry is tested with five different grids. Also the effect of increasing non-dimensional wall distance is studied with one grid. The studied grid densities are shown in table 5.1. Grids 1 and 4 are basically the same grid, but every second node of grid 4 has been removed in grid 1 (grid levels one and two). Grids 2 and 5 are also the same grids from grid levels two and one, respectively. Also shown in table 5.1 is grid 6 which is used to study the effect of the non-dimensional wall distance. It has the same number of cells as grid 4, but the non-dimensional wall distance is increased from the nominal value of grid 4.

Table 5.1: Number of cells for five grids used in the grid dependency tests. Also shown is grid 6, which is used in studying the effect of non-dimensional wall distance.

	Grid 1	Grid 2	Grid 3	Grid 4	Grid 5	Grid 6
Stator	127680	159600	860160	1021440	1276800	1021440
Rotor	121408	149408	633472	971264	1195264	971264
Diffusor	56000	70000	358400	448000	560000	448000
Total	305088	379008	1852032	2440704	3032064	2440704

Four stator vanes and seven rotor blades and a diffuser are modelled in all six grids. The grid covers one fifth of the whole turbine geometry. Part of the surface grid of grid 3 is presented in figure 5.1, every second grid line is visible for clarity. The calculation domain consists of 39 blocks with one block for each stator channel and one for each rotor channel. Tip clearance (1.9% of b_{rotor}) is also modelled. The distance of the inlet boundary face from the stator vane is 27% of the stator

axial chord.

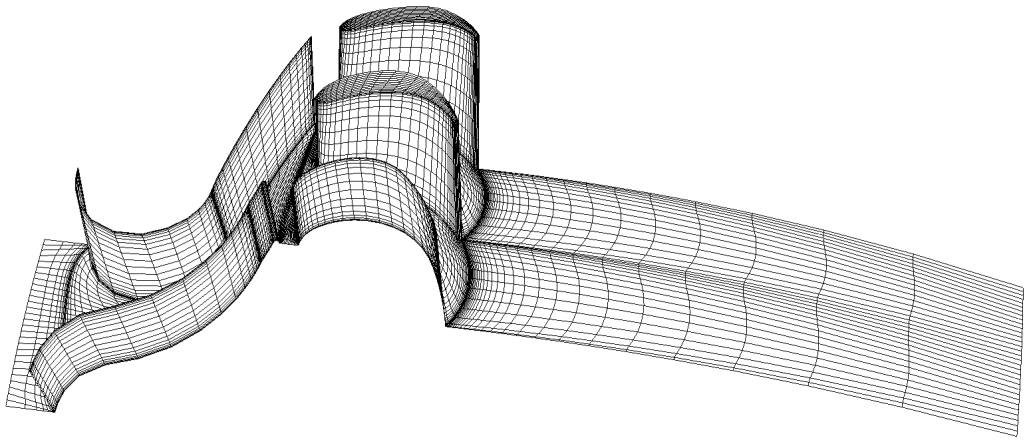

Figure 5.1: Surface grid of one stator channel and two rotor channels followed by a diffuser, every second grid line is visible for clarity. The shroud wall is not shown in the figure.

The performance parameter used in the grid dependency study is the total-to-static isentropic efficiency of the turbine, which is defined as

$$\eta_{\mathrm{s,t-s}} = \frac{T_{\mathrm{t1}} - T_4}{T_{\mathrm{t1}} - T_{4\mathrm{s}}} \tag{5.1}$$

where T_{t1} is the total inlet temperature, T_4 is the static outlet temperature, and $T_{4\mathrm{s}}$ is the static isentropic outlet temperature. All thermodynamic and flow properties are mass flow averaged.

The turbine total-to-static efficiency is plotted as a function of cell number in figure 5.2. The efficiency decreases from grid 1 to grid 3 but increases suddenly in grid 4, decreasing again from grid 4 to grid 5. According to the results, the grid density has an effect on the efficiency, and grid independency is not achieved from the efficiency point of view.

The non-dimensional wall distance y^+ of grid 1 at the rotor blade surfaces has a maximum value of 41.5, but is under 14 at a major part of the rotor suction surfaces and under 8 at a major part of the pressure surfaces. For grid 2, the maximum of y^+ at the rotor surface is 79.9, and a major part of the values are under 15 at the suction surface and under 8 at the pressure surface. For grid 3, the maximum

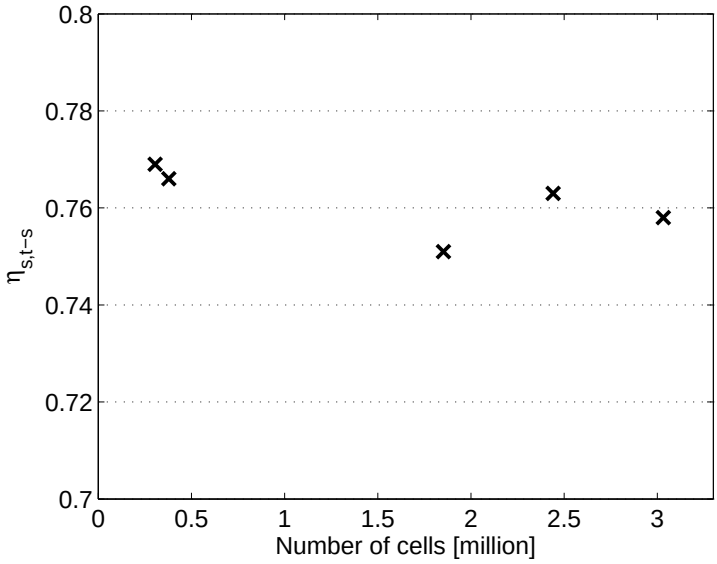

Figure 5.2: Effect of grid density on the total-to-static efficiency of the turbine.

of y^+ is 6.3, and a majority of the values are under three at the pressure surface and under four at the suction surface of the rotor. The maximum y^+ for grid 4 is 7.2, but most of the values are less than three, being overall slightly lower at the pressure surface. Grid 5 has a maximum y^+ of 7.4, but most of the values are less than three, and slightly lower values are detected at the pressure surface.

Radially averaged absolute rotor inlet and outlet flow angle distributions are plotted with a varying cell number in figures 5.3 (a) and (b), respectively. The variation of the flow angle at the rotor inlet is reasonably similar with all grids. The rotor outlet flow angle has more variation. Closer to the hub, all grids produce relatively similar flow angle distributions. The two densest grids produce most of the time the lowest flow angles, especially at the midspan and at the shroud. The effect of tip clearance is seen at the shroud as a higher flow angle in every case. With the two largest grids, the flow angles are reasonably similar from the midspan to shroud, the second largest being lower after the hub until the midspan.

When considering the absolute Mach number distribution at the rotor inlet and outlet (figures 5.3 (c) and (d)), the effect of grid density is opposite to the flow angle behaviour. The Mach number variates more at the rotor outlet than at the inlet. The distributions in grids 1 and 2 are relatively similar. The distributions in grids 4 and 5 are also quite similar, the values of the largest grid being a little higher most of the time. The Mach number distribution at the rotor outlet in figure

5.3 (d) shows that the distribution in the two smallest grids is relatively similar, and the three largest grids produce almost similar distributions.

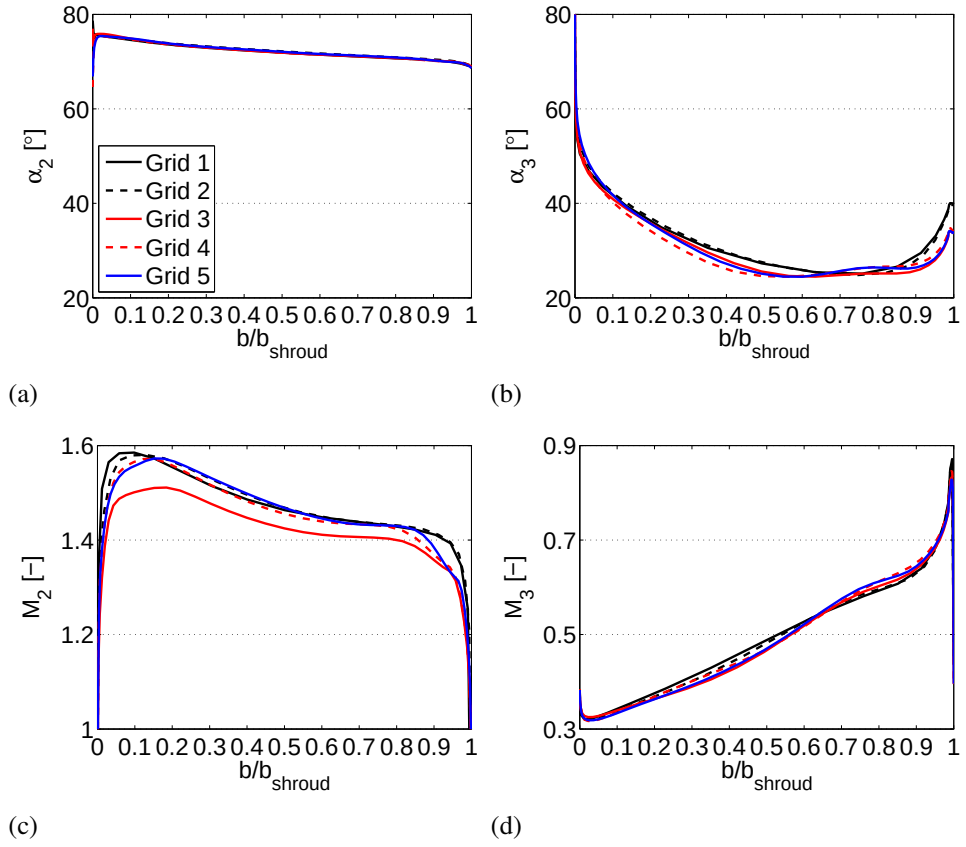

Figure 5.3: Effect of cell number in (a) absolute rotor inlet flow angle, (b) absolute rotor outlet flow angle, (c) absolute rotor inlet Mach number and (d) absolute rotor outlet Mach number variation, for grids in table 5.1.

5.1.1 Effect of non-dimensional wall distance

The effect of non-dimensional wall distance is studied by increasing the maximum y^+ of grid 4 from 6.7 to 33.9 of grid 6. The results are plotted in figures 5.4 (a) and (b). The value of grid 6 is subtracted from the corresponding value of grid 4 at each spanwise position. The absolute flow angles in figure 5.4 (a) are relatively similar at the rotor inlet, although the flow angle is slightly underestimated before the midspan and slightly overestimated especially at the shroud. The flow angle at the stator throat is predicted to increase if the y^+ is increased. Variations between

two cases are largest at the rotor outlet. The flow angle is underestimated with higher y^+ from the hub until approximately $1/3$ of the span and overestimated at the shroud. It is also slightly overestimated around the midspan and slightly underestimated before the shroud.

The Mach number distribution at the throat and rotor inlet and outlet is quite stable in figure 5.4 (b) when compared with the flow angle variation in figure 5.4 (a). At the rotor inlet, the Mach number of grid 6 deviates from grid 4 from the hub side, being slightly higher overall. The Mach number is slightly underestimated at the throat and for the last third of the span close to the shroud at the rotor outlet. The efficiency of grid 6 is 77.2% which is high compared to the 76.3 % of grid 4.

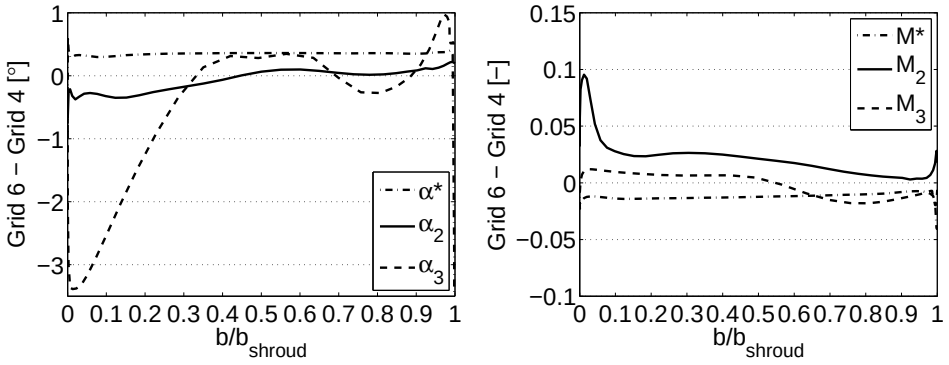

(a) (b)

Figure 5.4: Effect of grid density in the spanwise distribution of (a) absolute stator throat, rotor inlet and outlet flow angles, (b) stator throat, absolute rotor inlet and outlet Mach numbers as a function of non-dimensional wall distance.

5.2 Validation of numerical results

The performance of the solver Finflo in axial turbomachinery flows is validated against the baseline geometry presented by Sonoda et al. (2006). The modelled geometry is a 2-D transonic turbine profile. The measurements were done in the straight cascade windtunnel at DLR Goettingen. The tunnel is a blow-down type windtunnel having an atmospheric inlet.

Validation is made on a transonic profile in order to have understanding about the code performance when shock waves appear in the flow field. The surface grid

of the studied geometry is shown in figure 5.5, every second grid line is visible for clarity. The grid has two calculation blocks, and one block covers one flow channel having 1507328 cells. The maximum of non-dimensional wall distance y^+ is 6.8, overall the majority of the values are under 4 at the suction surface and under 3 at the pressure surface, which is close to the y^+ used in the largest grids of the grid dependency test.

Three measurement planes are defined and described here, more information is available in Sonoda et al. (2006). Measurement planes SS-37 and SS-02 are perpendicular to the suction surface, starting from suction surface positions $x/c_{ax} = 0.759$ and 0.993, respectively. Measurement plane 2 after the cascade is located at $x/c_{ax} = 1.325$. Pressure along the blade surface and the total pressure variation at measurement planes SS-37 and SS-02 are taken from the midspan. All other values are mass flow averaged.

The axial chord of the blade is $c_{ax} = 55.687$ mm, and the blade inlet flow angle α_1 is $65°$. The isentropic Mach number is 1.2 at plane 2.

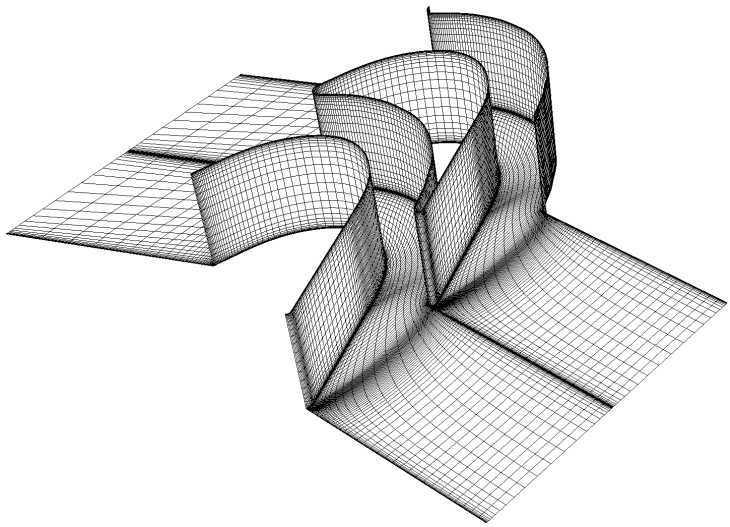

Figure 5.5: Surface grid of the studied transonic linear cascade by Sonoda et al. (2006), every second grid line is visible for clarity. The shroud wall is not shown in the figure.

The contours of density and the Schlieren image from Sonoda et al. (2006) are plotted in figure 5.6. Shock waves starting from the trailing edge of the blade look similar to the Schlieren image of the actual measurements. Reflections and compression waves from the suction surface of the blade are not fully reproduced.

Only darker shade areas are seen in the areas where the reflection from the suction surface coincides with the wake from the trailing edge. The angles of the trailing edge shock waves are compared in table 5.2. Shock waves are named upper (U) and lower (L) in figure 5.6 (a). Shock wave angles are measured relative to the axial flow direction. Both shock waves are measured lower than they are modelled. The angle of the lower shock wave is closer to the measurement than the upper one.

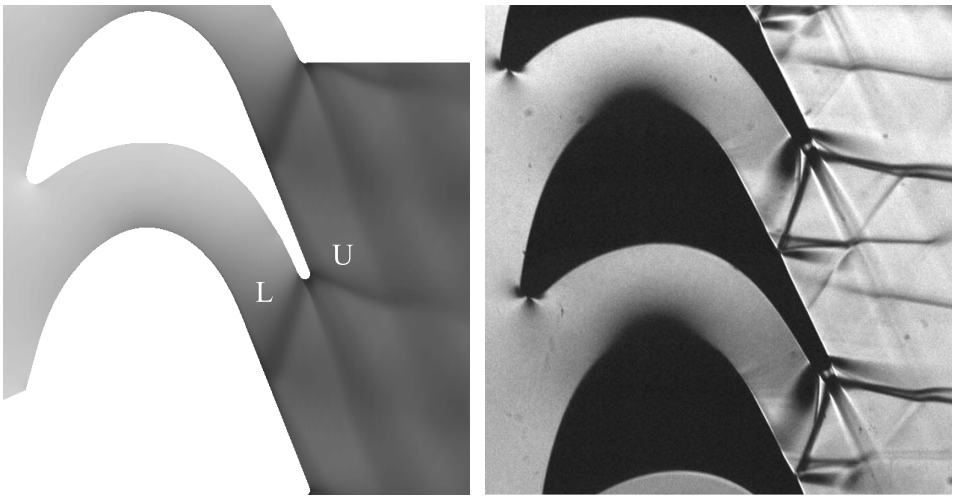

(a) (b)

Figure 5.6: Contours of density for the validation case with Finflo (a) and (b) measured cascade Schlieren image from Sonoda et al. (2006). Copyright © 2006 by ASME.

Table 5.2: Comparison between measured and modelled trailing edge shock wave angles. Values are from the blades that are fully shown in figure 5.6. Shock wave angles are measured relative to the axial flow direction.

	CFD	Measurement
Upper (U) [°]	20.5	9.7
Lower (L) [°]	109.3	103.6

The calculated isentropic Mach number along the airfoil profile is compared with the measurements of Sonoda et al. (2006) in figure 5.7. The figure shows that on the pressure surface the Mach number follows the measured values quite accurately. On the suction surface the Mach number is underpredicted from the leading

edge until $x/c_{ax} = 0.767$, except at $x/c_{ax} = 0.381$ the values coincide. Sonoda et al. (2006) also found that the calculated Mach number at the front part of the blade surface (until $x/c_{ax} = 0.381$) was lower than the measured value. This was reported to be due to a lower axial velocity density ratio ($AVDR = \rho_2 u_2/\rho_1 u_1$) compared to the measurements. In the subsonic two-dimensional cascade calculations of Pan (1993), employing Finflo with the Baldwin-Lomax turbulence model, the blade pressure distribution was underestimated for most of the blade surface.

The peak value at $x/c_{ax} = 0.836$ is higher than the measured one, with little transition to the downstream direction. The reflected shocks and compression waves at the suction surface are not seen clearly in CFD, which makes the curve flat compared to the drop in the measured value $x/c_{ax} = 0.933$. This is also seen in figure 5.6.

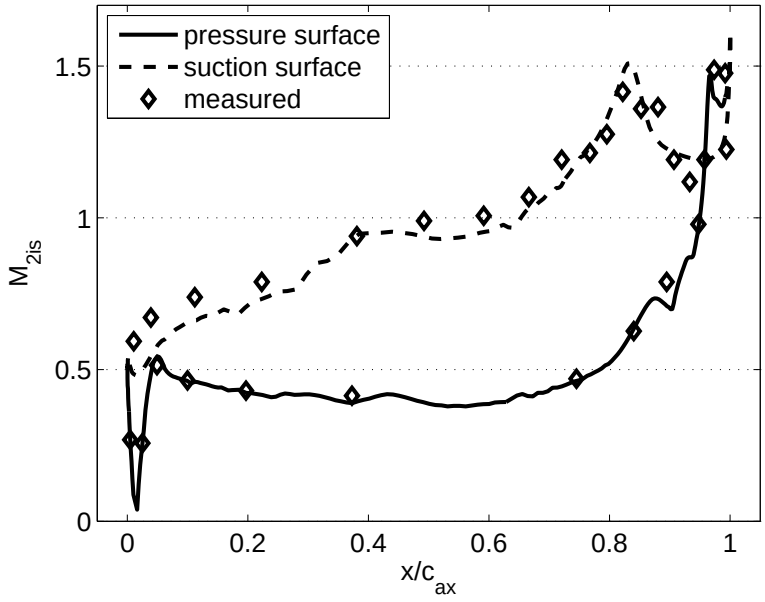

Figure 5.7: Comparison of calculated airfoil isentropic Mach number with the measurements of Sonoda et al. (2006).

The total pressure loss ω is calculated by equation

$$\omega = 1 - \frac{p_{\mathrm{t}}}{p_{\mathrm{t}1}} \tag{5.2}$$

where p_{t} is the total pressure at the measurement plane, and p_{t1} is the total pressure at the inlet of the calculation domain.

The total pressure losses at planes SS-37 and SS-02 are plotted in figures 5.8 (a) and (b) respectively. The total pressure loss at plane SS-37 shows that the wake is wider with CFD than the measurements indicate. Also the losses are underestimated outside the wake area, except for most of the area between the suction surface and the wake. Figure 5.8 (b) shows also a wider than measured wake profile at plane SS-02. The total pressure losses are higher than the measured ones in the areas close to the suction surface followed by a relatively long underestimated area. The higher pressure losses close to the suction surface are caused by shock waves starting from that area. The losses are underestimated in the area between the suction surface shock waves and the wake. The wake-generated losses have a higher peak value than in the measurements, which could be due to weaker shocks and reflections from the suction surface.

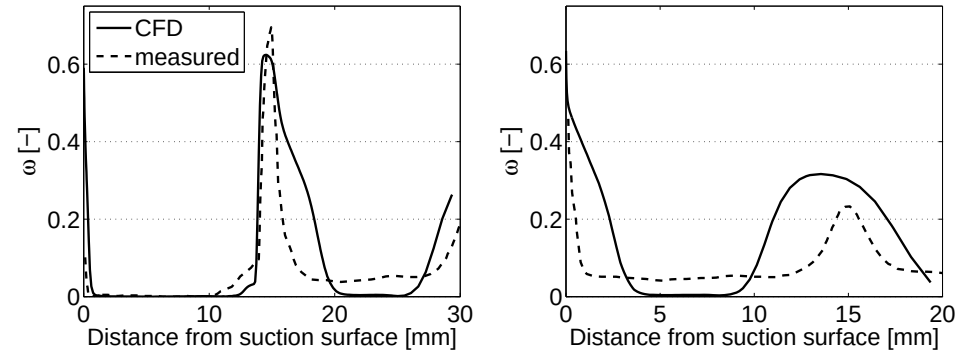

Figure 5.8: Comparison of calculated total pressure loss coefficients at planes SS-37 (a) and SS-02 (b) with the measurements of Sonoda et al. (2006).

5.3 Comparison of analytical and numerical shock wave angles

A simple calculation is made with the quasi-steady supersonic stator results presented in chapter 6.3. Analytical calculations are made using the theory presented by Anderson (1991). The calculations follow the path presented by Harinck et al. (2007), which is based on oblique shock formation at the trailing edge. The method is described here briefly. First the wake angle θ is determined from the CFD results. Next by knowing the Mach number, static pressure, static temperature and the speed of sound upstream of the shock wave, the analytical compres-

sion wave angle β is solved iteratively. The comparison between analytical and numerical shock wave angles is shown in figure 5.9. It should be noted that the wake angle determination causes some uncertainties to the analytical calculation. The figure shows that the numerical and analytical shock wave solutions are relatively similar in the beginning, but after that the numerical results deviate from the analytical ones.

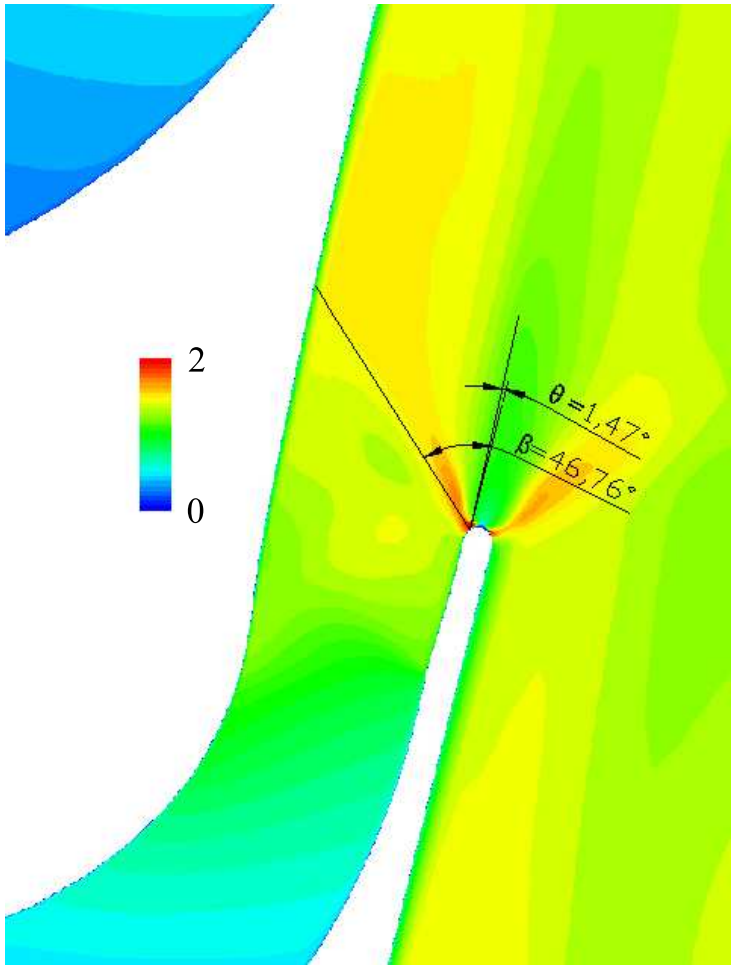

Figure 5.9: Contours of the Mach number from quasi-steady-stator-only modelling presented in chapter 6.3, and a comparison of analytical and numerical shock wave angles.

5.4 Conclusions and discussion

The grid dependency tests showed that the turbine efficiency depend on the number of cells in the calculation domain. According to the results, the density of the grid used in the modelling is not dense enough to produce grid-independent results. The spanwise variation of the absolute flow angle at the rotor inlet is grid-independent, but at the rotor outlet there is more variation. At the rotor outlet, the increase of cell number from the second largest to the largest grid does not have a great effect on the absolute flow angle from the midspan to the shroud. The absolute Mach number distribution at the rotor inlet depends on the grid density. The Mach number increases slightly from the second largest to the largest grid, but the shape of the distribution is affected only slightly. At the rotor outlet, the Mach number distribution is affected only slightly by the grid density in the three largest grids.

The absolute Mach number at the rotor outlet and stator throat is not drastically affected by the increase of the non-dimensional wall distance y^+, whereas a clearer increment in the Mach number can be seen at the hub side at the rotor inlet. The absolute outlet flow angle of the rotor at the hub is underestimated until $1/3$ of the span, and overestimated at the shroud. At the rotor inlet, the effect of increasing y^+ is similar to the rotor outlet, but less drastic. The results show that increasing y^+ increases the efficiency. This could be due to underestimation of viscous losses in the boundary layer.

The flow field at the validation study showed that Finflo is capable to predict the shock waves starting from the trailing edge. The angle of the trailing edge shock wave is modelled higher than the measurements show (relative to the axial flow direction). The shape of the shock wave at the suction surface differs from the measured one, starting earlier from the upstream direction. This may be caused by some small differences between the measured and modelled blade profiles. Also the over-unity non-dimensional wall distance can cause an error in the modelling. The wake profile is also wider when compared to the measurements.

The shock wave reflections and compressions from the suction surface were not fully modelled. This caused differences in the airfoil isentropic Mach number distribution. It also might have caused some differences with the measured total pressure losses.

The airfoil isentropic Mach number distribution is well modelled at the pressure surface, but the suction surface distribution is underestimated along the blade surface until $x/c_{ax} = 0.381$, and after that again until $x/c_{ax} = 0.767$. The pressure

along most of the blade surface has been reported to be underestimated also in an earlier study with Finflo employing the Baldwin-Lomax turbulence model. The peak value of isentropic Mach number is higher than the measured at the suction surface.

Overall Finflo, is capable of modelling shock waves with certain limitations on reflections and compressions from surfaces. It should be noted, however, that it could be possible to produce better modelling of reflections and compressions by decreasing the non-dimensional wall distance. This could also lead to better prediction of the total pressure losses.

In the case of the supersonic stator, the trailing edge shock wave is modelled well in the beginning of the wave, when numerical and analytical results are compared. Later on in the flow channel, the results deviate from each other when the angle of the numerical results decreases.

6 Numerical results

In the beginning of the chapter, the effect of changing the axial distance between the stator and rotor is studied under the design conditions. This is followed by an off-design performance study of the turbine in the case of a variating axial gap between the stator and rotor. In the third part, a pulsating inlet flow model is introduced to Finflo, and the effects of mass flow pulsation to the flow field and performance are studied with a supersonic axial turbine stator.

6.1 Quasi-steady modelling of the effects of stator-rotor axial distance at the design conditions

In order to improve the understanding of the effect of variation of stator-rotor axial distance on the performance of supersonic turbines having small reaction, five axial gaps are studied under the design operating conditions presented in table 3.1. The studied cases are shown in table 6.1. The axial gap is measured from the hub, as shown in figures 3.3 (a) and (b), and is scaled with the average rotor height ($b_{\mathrm{rotor}} = (b_2 + b_3)/2$). Case 2 is the original design of the turbine.

In all the cases, four stator and seven rotor channels are modelled with a diffuser following every rotor. Also the tip clearance (1.9% of b_{rotor}) is modelled. The grid of case 2 is similar to grid 4 in the grid dependency tests, the only difference is that the inlet part of the computational domain is 10 times longer than in the grid dependency tests. This has been done to make certain that the computational inlet boundary is not affected by the stator.

The number of cells varies between each calculated case, due to a different number of nodes inserted in the axial gap between the stator and the rotor. The number of cells in the inlet part, stator flow channel, rotor flow channel and diffusor are kept constant between the cases. The total number of cells for each case, and the maximum non-dimensional wall distance y^+ at the rotor blade surface are shown in table 6.1. A relatively high y^+ compared to case 2 was used in the other four cases, due to problems with calculation stability when having smaller wall distances. The effects of the higher y^+ were studied in chapter 5.1.1 and are also discussed in this chapter. The side profiles of the modelled axial gaps are shown in figure 6.1. It should be noted that increasing the axial gap slightly changes the shape of the shroud wall between the stator and the rotor.

The isentropic total-to-static efficiency of the turbine is calculated by equation 5.1. The performance of the diffuser is evaluated by the diffuser static pressure

Table 6.1: Calculated cases with relative axial gaps, cell numbers and maximum y^+ at the rotor blade surface.

	$g_{\mathrm{ax}}/b_{\mathrm{rotor}}$	Number of cells	Maximum y^+
Case 1	0.112	2530304	18.3
Case 2	0.149	2601984	7.2
Case 3	0.299	2763264	38.5
Case 4	0.448	2781184	18.3
Case 5	0.598	2852864	17.5

rise coefficient, which is defined as

$$C_{\mathrm{pr}} = \frac{p_4 - p_3}{p_{\mathrm{t}3} - p_3} \tag{6.1}$$

where p_3 is the static pressure at the diffuser inlet, p_4 is the static outlet pressure, and $p_{\mathrm{t}3}$ is the total pressure at the diffuser inlet. All the temperatures and pressures used in calculating the performance parameters are mass flow averaged. Also the flow angle, Mach number and velocity distributions are made with mass flow averaged values.

The calculated total-to-static efficiency of the turbine is plotted in figure 6.2. The calculated efficiencies are divided with the total-to-static efficiency of case 2 (0.721) in order to be comparable with the comparison case of Jeong et al. (2006). The efficiency decreases when the axial distance increases. The decrement in the turbine efficiency accelerates when the axial gap increases. Especially starting in $c_{\mathrm{ax}}/b_{\mathrm{rotor}} = 0.448$, the penalty from the increased axial gap grows rapidly. Agreement with the results of Jeong et al. (2006) is reasonably good, although their studies concern supersonic impulse turbines. The new results also cover higher relative axial gaps. It should be noted, however, that the efficiency for two of the smallest measured axial gaps is clearly higher than the CFD predicts. This could be e.g. due to overprediction of the stator-rotor interaction with smaller relative axial gaps.

The rest of the performance parameters are shown in table 6.2. The actual total-to-static efficiency variation is 1.9 per cent between the peak and bottom values. The differences between the cases in C_{pr} are relatively small, and dramatic drops are not seen. The difference between the peak value of case 2 and the bottom value

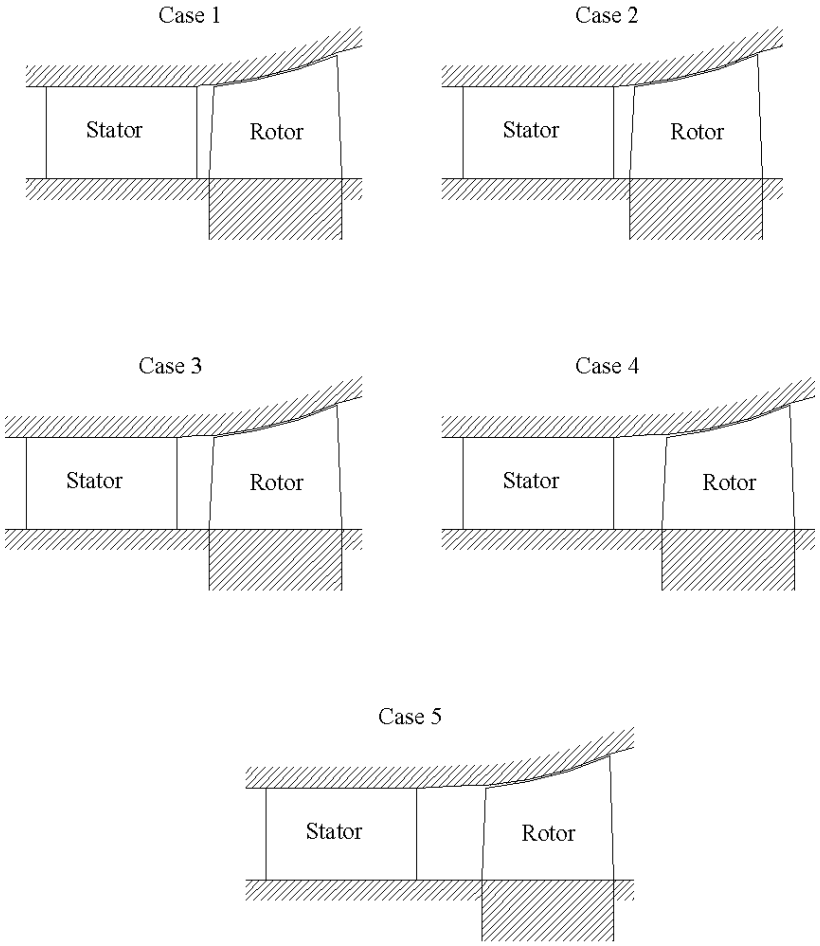

Figure 6.1: Different modelled axial gaps.

of case 1 is 0.019.

In figures 6.3 (a) and (b), the total pressure loss as a function of the axial gap is plotted. The loss is calculated by equation 5.2. In figure 6.3 (a), the increase is small between cases 1 and 2, but a steeper increase is seen in cases 3, 4 and 5. An increase of total pressure loss due to the increase of the axial gap is also reported by Jeong et al. (2006). In figure 6.3 (b), spanwise total pressure loss is plotted. At the midspan the losses are almost equal between the cases, but when the axial gap increases, the losses increase at the hub and shroud rapidly from case 2 to case 3. An increase in total pressure loss at the hub and shroud is also seen with larger axial gaps in cases 4 and 5.

The flow development from the stator leading edge to the rotor leading edge (mea-

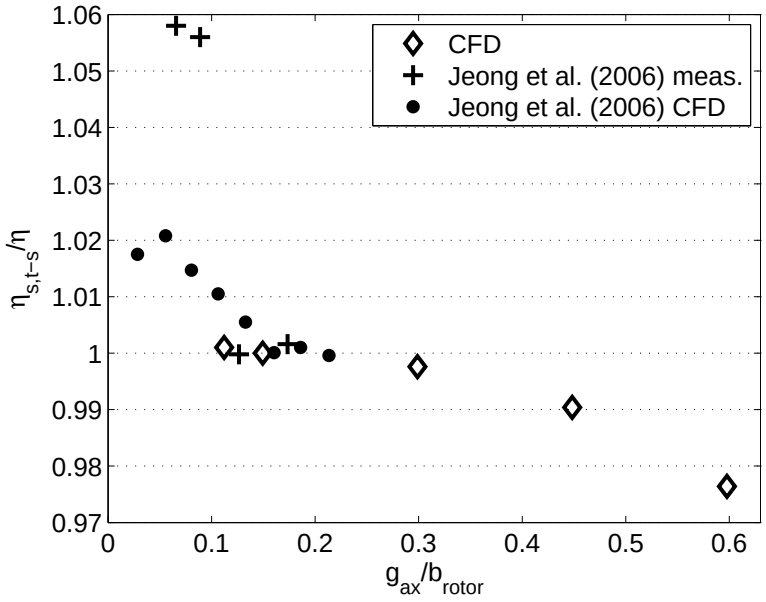

Figure 6.2: Variation of total-to-static efficiency as a function of axial distance between the stator and rotor. The results (CFD) are compared with the results of Jeong et al. (2006).

Table 6.2: Performance of the turbine with variating axial distance between the stator and rotor.

	Case 1	Case 2	Case 3	Case 4	Case 5
$\eta_{\mathrm{s,t-s}}$ [%]	76.3	76.2	76.0	75.5	74.4
C_{pr} [-]	0.547	0.566	0.564	0.550	0.561

surement plane 2) is plotted in figures 6.4 (a) and (b) as mass flow averaged values along the axial length l_{ax}. The flow accelerates smoothly into sonic speed and continues to rise steeply until the acceleration becomes slower before the trailing edge of the stator. After this small step, the flow continues to accelerate steeper, and this is common for all cases. The peak value is detected in all geometries just before the trailing edge. It is common for all the cases that the Mach number decrement is fastest closer to the peak value. The Mach number becomes constantly lower when the distance from the peak value increases in cases 1 and 2, until there is a small increase in the Mach number just before the rotor leading edge. This increase is in practice negligible. Also in case 3 the Mach number decreases smoothly and a small increment appears just before the rotor leading edge, and a similar increment is also seen in cases 4 and 5. In case 4, the Mach number

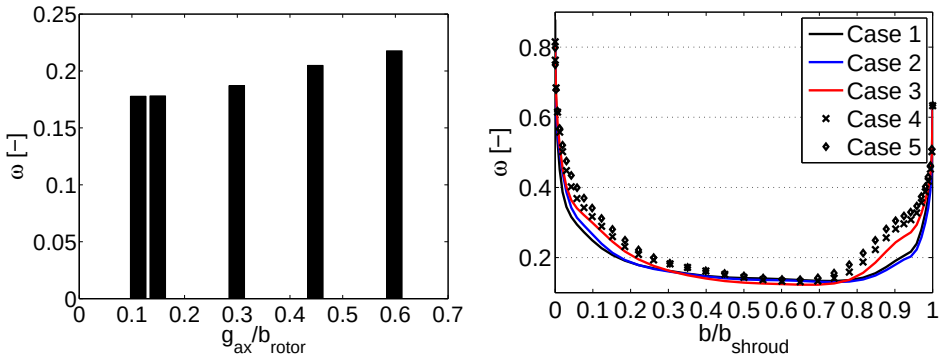

(a) (b)

Figure 6.3: Total pressure loss from turbine inlet to measurement plane 2 at the rotor inlet, (a) mass flow averaged values and (b) spanwise mass flow averaged distribution with variating axial gap. The calculated cases 1 to 5 are presented in table 6.1 and figure 6.1.

decreases until a minimum value is found at approximately 16% of the axial gap length g_{ax} and is followed by a rise and a second local minimum approximately at $0.75g_{\mathrm{ax}}$. The Mach number behaviour in case 5 is similar to case 4, the first minimum is found at $0.1g_{\mathrm{ax}}$ and the second minimum at $0.45g_{\mathrm{ax}}$.

6.1.1 Stator throat flow field

In figures 6.5 (a) and (b), the spanwise flow field at the stator throat is plotted. The stator throat absolute flow angle in figure 6.5 (a) is relatively similar in other cases than in case 2. The flow angle is lower than the design value of $78°$ at areas near the hub or shroud. Approximately at 20% to 80% of the flow channel length in case 2, the flow angle is close to the designed value, whereas the values in other cases are higher than the designed ones. This is in accordance with the results presented in chapter 5.1.1, which predict an increased throat flow angle when y^+ is increased. It also explains the highest flow angle distribution of case 3.

The Mach number in figure 6.5 (b) is highest at the hub and decreases towards the shroud. The Mach number of case 2 is higher than in the other cases. This is in accordance with the results presented in chapter 5.1.1, which predict a decreased throat absolute Mach number when y^+ is increased. It also explains the lowest Mach number distribution of case 3. The Mach number distribution is higher than the designed value of unity at the throat, which is common for all the cases.

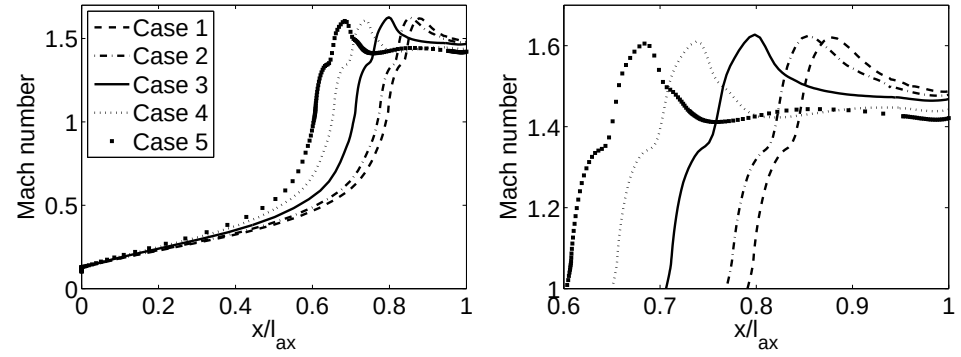

Figure 6.4: Flow development from stator leading edge into rotor leading edge at measurement plane 2 (a) and (b) magnification of the areas with Mach number greater than unity. The calculated cases of 1 to 5 are presented in table 6.1 and figure 6.1. The rotor leading edge is situated in $x/l_{\mathrm{ax}} = 1$.

6.1.2 Rotor inlet flow field

The measurement plane at the rotor inlet was situated approximately at the rotor leading edge. The radially averaged rotor inlet flow angle at the rotor inlet is plotted in figure 6.6 (a). The flow angle decreases from the hub to the shroud. In the areas close to the hub, the flow angle increases when the axial distance between the stator and rotor increases. At the shroud side of the spanwise distribution, the increase of the axial gap decreases the flow angle. These changes lead to less variating rotor incidence with the smaller axial gap. This is slightly different from the results of Funazaki et al. (2007), who found that the increase of axial gap increases the rotor incidence angle. When the potential effect of higher y^+ is considered, it could move the distribution of case 3 closer to cases 4 and 5.

In figure 6.6 (b), the spanwise absolute Mach number at the rotor inlet is plotted. The differences at spanwise distributions are more pronounced at the hub and shroud than they are at the midspan. The Mach number is highest at the areas close to the hub and it decreases towards the shroud. The maximum value of the distribution moves towards the shroud when the axial gap increases. At the hub and shroud, increasing of the axial gap decreases the Mach number, except for cases 1 and 2, which have almost identical distributions at the shroud. The distribution in cases 3 to 5 has a greater drop before the shroud wall than cases 1 and 2. When the potential effect of a higher y^+ is considered, it moves the distribution of case 3 closer to cases 4 and 5. When the axial gap is increased, the boundary

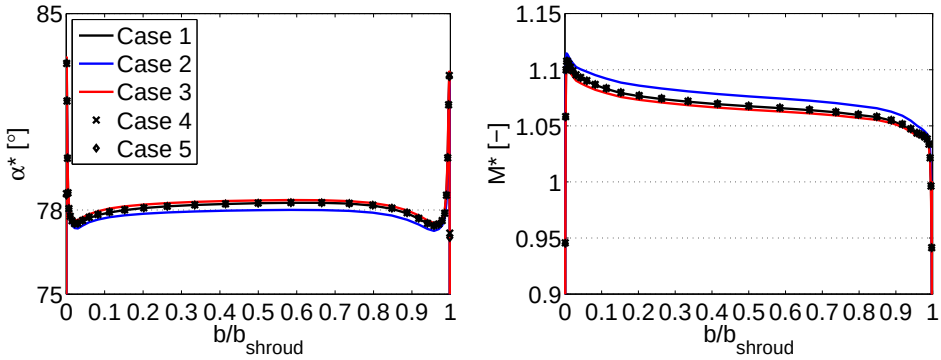

(a) (b)

Figure 6.5: Spanwise averaged stator throat (a) absolute flow angle and (b) Mach number with variating stator-rotor axial distance. The calculated cases of 1 to 5 are presented in table 6.1 and figure 6.1.

layer thickness at the hub increases. At the shroud, the boundary layer thickness increases with an increasing axial gap in other cases than between the two smallest axial gaps. In the paper Funazaki et al. (2007), boundary layer thickness is also reported to grow at the rotor inlet when the axial gap increases.

In figure 6.6 (c), the spanwise axial velocity distribution is plotted. The axial velocity increases from the hub to the shroud. At the hub the axial velocity decreases when the axial gap increases. The differences between all cases are greater at the hub than at the shroud.

Spanwise tangential velocity is plotted in figure 6.6 (d). It follows the Mach number distribution quite well. Tangential velocity decreases from the hub to the shroud, and the differences between the cases are less pronounced at the midspan. Tangential velocity increases when the axial gap decreases at the hub and shroud, except for cases 1 and 2, where the distributions are almost similar at the shroud.

6.1.3 Pressure at the rotor surface

The static pressure variations at the rotor hub, midspan and shroud are plotted in figures 6.7 (a), (b) and (c), respectively. The pressure variation over the blade is smaller at the hub than at the midspan. The highest pressure variation is seen at the shroud. A pressure peak is seen at the leading edge. A low pressure area is seen at the suction surface after the leading edge. This low pressure area moves towards

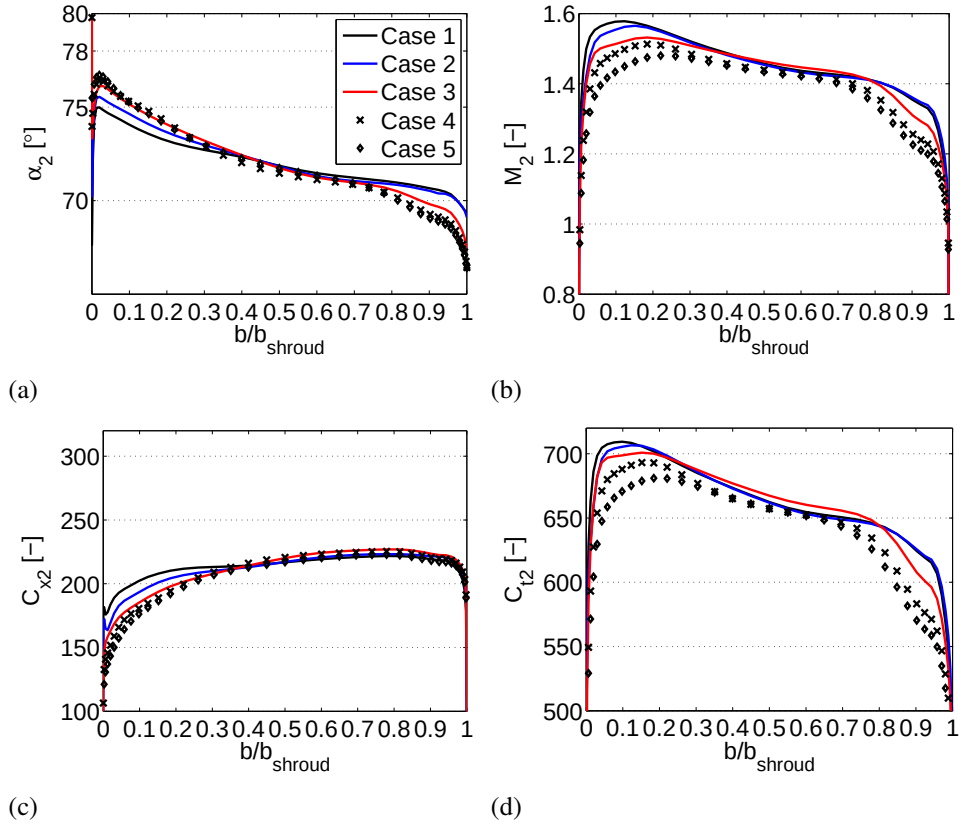

Figure 6.6: Spanwise averaged rotor inlet (a) absolute flow angle, (b) absolute Mach number, (c) axial velocity, and (d) tangential velocity with variating stator rotor axial distance. The calculated cases of 1 to 5 are presented in table 6.1 and figure 6.1.

the trailing edge when the observed area changes from the hub to the midspan and further to the shroud. An area of low pressure is also seen at the trailing edge at the midspan and the shroud. The differences in the calculated pressures between the different cases at the hub and midspan are higher in the suction surface than in the pressure surface.

In case 5, a relatively high pressure is seen at the suction surface at the hub, starting from the leading edge. Also in case 4, the pressure is almost as high as in case 5 and is higher than in the three smallest axial gaps, approximately from 15% of axial chord length until $0.35c_{ax}$. At the shroud the pressure at the suction surface in case 5 is the highest and in case 4 the second highest after the leading edge, until approximately $0.23c_{ax}$ in case 4 and $0.43c_{ax}$ in case 5. At the shroud, the pressure difference over the rotor blade is best in case 2, especially the pressure at

the pressure surface is higher for most of the blade surface.

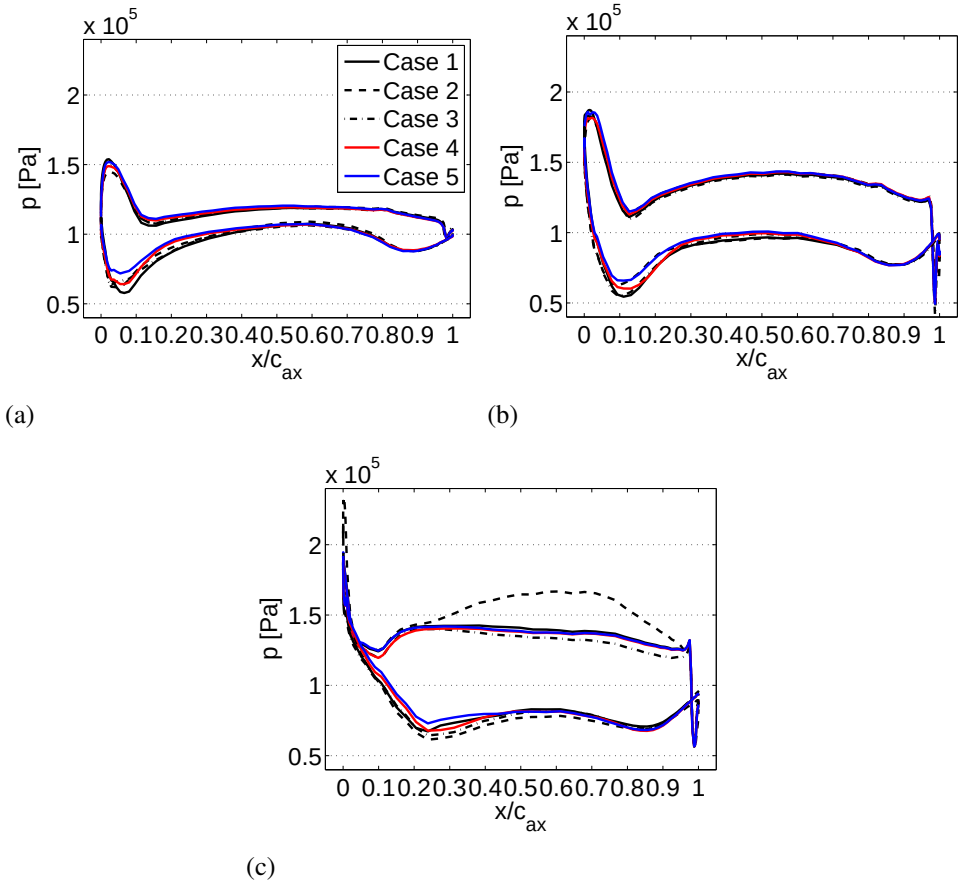

Figure 6.7: Pressure at the rotor surface at the hub (a), at the midspan (b) and at the shroud (c). Calculated cases from 1 to 5 are described in table 6.1 and figure 6.1.

6.1.4 Rotor outlet flow field

The absolute flow angle at the rotor outlet is plotted in figure 6.8 (a). The flow angle is higher at the hub than at the shroud. There is also a steep increase in the flow angle close to the shroud due to tip clearance flow and a small drop before the casing in all geometries. A second smaller increase is seen in cases 1 and 2 a little after the midspan, but these kinds of steps are not seen in the other cases. When the potential effect of a higher y^+ is considered, it moves the distribution of case 3 closer to cases 4 and 5 at the midspan. It should be noted that the rotor outlet

flow angle has been designed to be zero degrees, which is not achieved according to these results.

In figure 6.8 (b), the spanwise absolute Mach number distribution is plotted. The Mach number rises from the hub to the shroud and more ”linear” curves are seen in cases 1 and 2 than in the rest of the cases. Similar behaviour is also seen in the axial velocity distribution in figure 6.8 (c). When the potential effect of a higher y^+ is considered, it moves the Mach number distribution of case 3 closer to cases 1 and 2. Figure 6.8 (d) shows that the tangential velocity decreases at the hub, and after that it starts to increase towards the shroud. A rise in tangential velocity due to tip clearance flow is seen just before the shroud, followed by a drop before the casing. This behaviour is also common for the Mach number and axial velocity. Tangential velocity has more drastic changes in cases 1 and 2 than in the other cases.

The isentropic total-to-static efficiency from the turbine inlet to the rotor outlet is calculated as

$$\eta_{\mathrm{s,t-s}} = \frac{T_{\mathrm{t1}} - T_3}{T_{\mathrm{t1}} - T_{3\mathrm{s}}} \tag{6.2}$$

where T_3 is the static rotor outlet temperature and $T_{3\mathrm{s}}$ is the static isentropic rotor outlet temperature. All thermodynamic and flow properties are mass flow averaged.

In figure 6.9, the turbine efficiency at the rotor outlet is plotted from hub to shroud for all five different axial gaps. An increase of the axial gap decreases the efficiency at the hub area. The most drastic drops are seen from case 2 to 3 and from case 4 to 5. At the shroud all the cases have more similar performance.

6.1.5 Conclusions and discussion

The study shows that with smaller axial gaps, the turbine performance is not as highly affected by the axial gap variation as with larger axial gaps. With larger relative axial gaps of $g_{ax}/h_{rotor} = 0.448$ and $g_{ax}/h_{rotor} = 0.598$, the performance penalty due to the increasing axial gap grows rapidly. With this studied turbine type the results show that the increase of the axial gap has an accelerating effect on efficiency decrement, although it should be noted that a varying y^+ could have an effect on the efficiency. Especially in the intermediate axial gap the efficiency

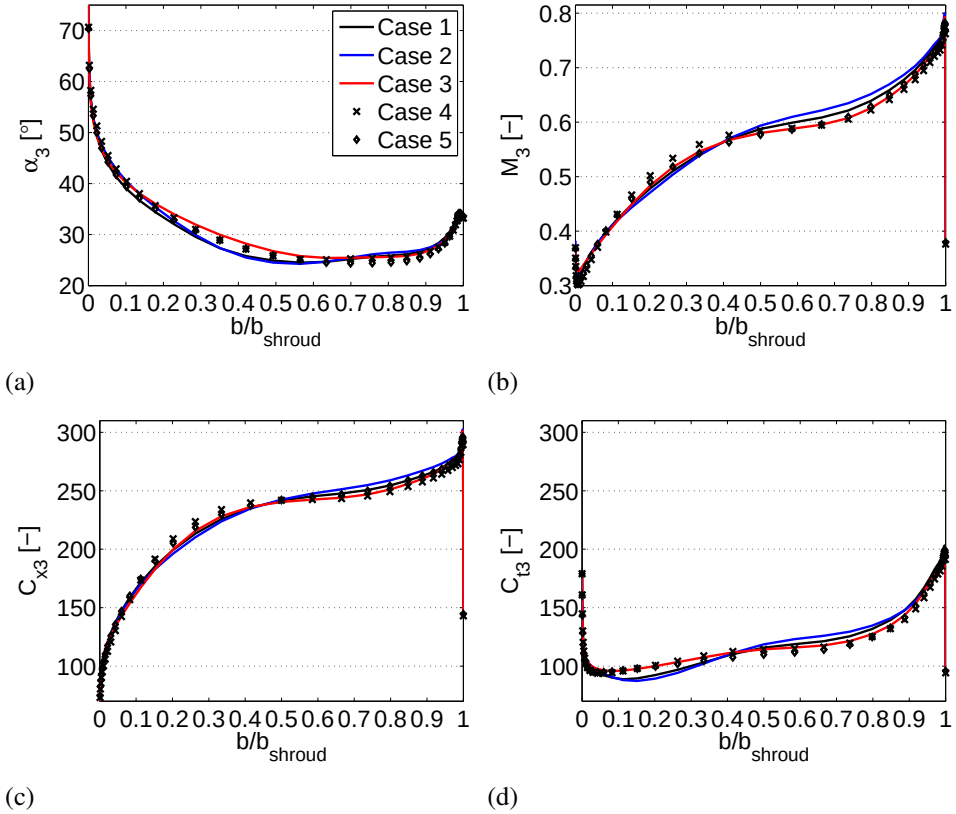

Figure 6.8: Spanwise averaged rotor outlet (a) absolute flow angle, (b) Mach number,(c) axial velocity and (d) tangential velocity with variating stator rotor axial distance. The calculated cases of 1 to 5 are presented in table 6.1 and figure 6.1.

can be lower than predicted. Overall, the efficiency of the turbine in the design operating conditions is higher than is usually presented in the literature for supersonic axial turbines. The efficiency is still, however, lower than it is typically with high reaction subsonic axial turbines.

The diffuser performance is only slightly affected by changes in the axial gap. The total pressure loss from the stator inlet into the rotor inlet increases when the axial gap increases, which is in accordance with the literature. The increase is seen both at the hub and the shroud, but at the midspan the losses are relatively similar in all cases. The results show that there is a connection with the whole turbine performance and the total pressure losses due to an increased axial gap. The importance of total pressure losses in the whole turbine performance is evident, but with the two largest axial gaps the losses do not increase as much as they should if

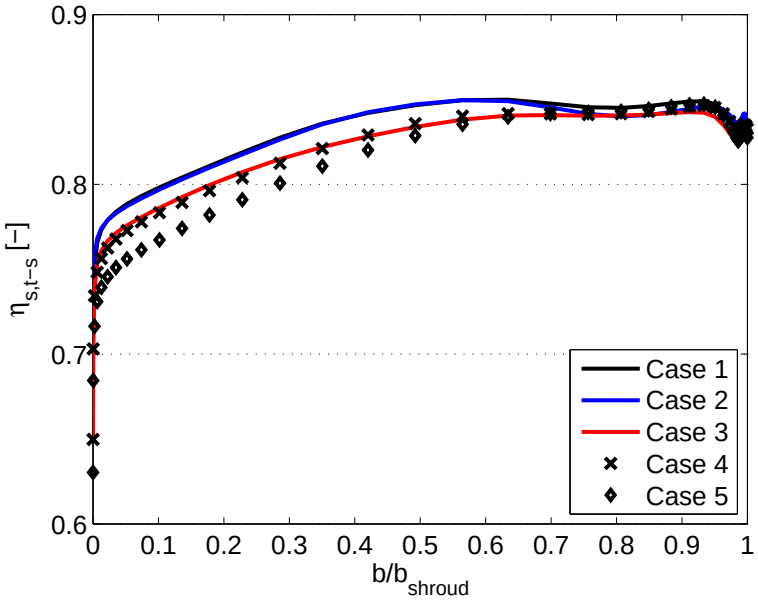

Figure 6.9: Spanwise distribution of isentropic total-to-static efficiency calculated from the turbine inlet to the rotor outlet by equation 6.2. The calculated cases of 1 to 5 are presented in table 6.1 and figure 6.1.

there were a linear correlation between the efficiency and the total pressure losses.

In all of calculated cases, the Mach number from the stator inlet rises smoothly into sonic speed, and a small step in acceleration appears before the stator trailing edge. After this, the flow accelerates into maximum speed, which is seen just before the trailing edge. The Mach number decreases relatively smoothly from the maximum in cases 1 to 3, whereas in cases 4 and 5 there is one additional acceleration followed by a deceleration in the space between the stator and the rotor.

The stator throat flow field is in practise not effected by the axial gap variation. The Mach number distribution is greater than unity in every case, which indicates that the actual throat has moved back to the upstream direction.

At the rotor inlet, the flow angle at the hub increases when the axial gap increases, whereas the flow angle at the shroud decreases when the axial gap increases. This leads to a less variating rotor incidence with a smaller axial gap. Overall, the flow angle decreases from the hub to the shroud. This more curved rotor inlet flow angle distribution profile can be worse for the rotor, and that way it can decrease the efficiency. Because the flow angle is more tangential at the hub, the flow at

the hub has to travel longer until it reaches the rotor blades, compared to the flow at the shroud. This longer flow path can increase the losses and explain the lower hub side efficiency.

The absolute Mach number at the rotor inlet is higher at the hub and decreases towards the shroud. When the axial gap increases, the maximum of the spanwise Mach number moves towards the shroud. In general, an increase of the axial gap decreases the absolute Mach number at the hub and the shroud. Also the boundary layer thickness has a tendency to increase at the hub and the shroud when the axial gap increases, which is in accordance with the literature. The behaviour of tangential velocity is similar to the absolute Mach number. Opposite to tangential velocity, axial velocity increases from the hub to the shroud. At the hub, axial velocity decreases with the increasing axial gap.

The pressure variation over the rotor blade is smallest at the hub and increases towards the shroud. At the hub and the midspan, the pressure variations between the calculated cases are higher at the suction surface than at the pressure surface. There is no clear connection between the blade loading and variation of axial distance between the stator and the rotor. Areas of higher pressure at the suction surface are seen in cases 4 and 5 at the hub and the shroud.

The increase of the axial distance between the stator and the rotor decreases the fluctuation of the rotor outlet absolute flow angle when $g_{ax}/b_{rotor} \geq 0.149$. An increase in the flow angle, Mach number, axial velocity and tangential velocity is seen at the shroud because of the tip clearance flow. The Mach number does not have any clear trend, even though with the two smallest axial gaps, the distribution is more linear than in the other cases, which is also common for the axial velocity distribution. When the potential effect of y^+ is considered, it makes the Mach number distribution of the third largest axial gap more linear, which indicates a connection between the more linear rotor outlet Mach number and better turbine performance. The fluctuation of tangential velocity is stronger with the two smallest axial gaps than with the rest of the cases. The increase of the axial gap decreases the spanwise turbine performance at the hub when the turbine efficiency at the rotor outlet is examined.

Based on the discussed results, the differences in the performance between different axial gaps are mainly caused by the total pressure losses between the stator and the rotor, but also some increasing additional losses may happen due to a higher hub side rotor incidence and lower axial velocity. It can be concluded that the objective of studying the effect of stator-rotor axial distance on the studied turbine type and improvement of the efficiency in the design conditions is reached.

6.2 Quasi-steady modelling of the effects of stator-rotor axial distance at off-design conditions

The studied turbine is also modelled in low pressure ratio and low rotating speed operating conditions with variating stator-rotor axial gaps. The differences between the modelled cases are evaluated. The differences between off-design and design performance are also studied. The off-design operating conditions used in the modelling are from actual measurements, and they are shown in table 6.3 as the low off-design condition. These measurements were preliminary, however, and the data of temperatures etc. was not reliable enough to be used e.g. in efficiency comparison. The modelled geometries are cases 2, 3 and 5 in the table 6.1, and they are referred to with these numbers later in the text. The studied turbine was also measured with the rotating speed of 28500 rpm, and this operating condition and the measured efficiency are shown in table 6.3 as the intermediate off-design condition. Due to late completion of the measurements at the intermediate off-design condition, the turbine has not been modelled numerically in this condition.

Table 6.3: Off-design conditions of the turbine.

Off-design condition	low	intermediate
Mass flow [kg/s]	0.49 $q_{\mathrm{m},des}$	0.84 $q_{\mathrm{m},des}$
Pressure ratio [-]	2.55	4.05
Rotating speed [rpm]	23010	28500
Measured efficiency [%]	-	76.1

The isentropic turbine total-to-static efficiency is calculated by equation 5.1, and the modelled results are plotted in figure 6.10. All the temperatures and pressures used in calculating the performance parameters are mass flow averaged. Also the flow angle, Mach number and velocity distributions are calculated with mass flow averaged values. The total-to-static efficiency decreases when the axial gap increases. The efficiency decrement is almost linear, which is in agreement with the results of Yamada et al. (2009). The measured efficiency in the intermediate off-design condition is higher than the calculated efficiency in the low off-design condition with the same axial gap but is slightly lower than the calculated efficiency in the design conditions. In a recent study by Jaatinen (2009) using Finflo, the

centrifugal compressor performance is reported to be underpredicted with CFD when Chien's k-ϵ turbulence model has been used, whereas in an earlier study of Turunen-Saaresti (2004) the results were opposite, although it should be noted that in the earlier study the tip clearance was not modelled.

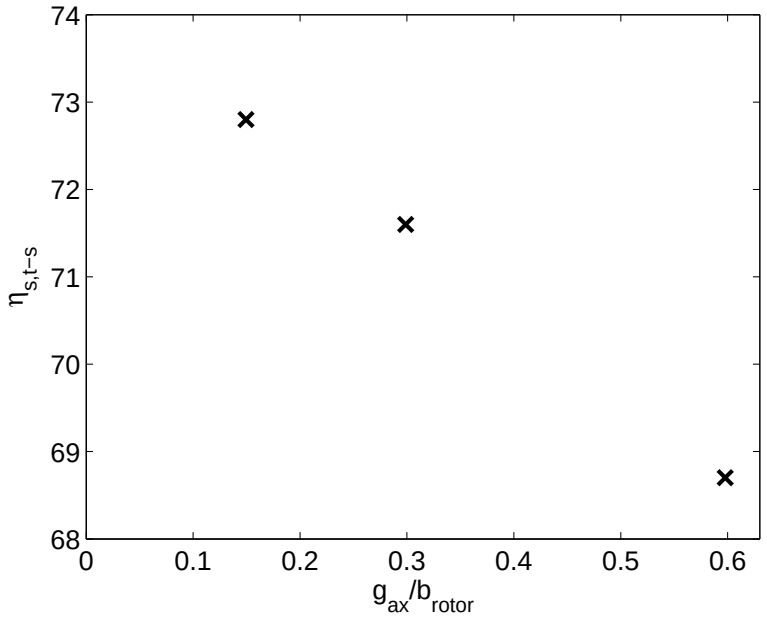

Figure 6.10: Isentropic total-to-static efficiency of the turbine at low off-design conditions (shown in table 6.3).

In figures 6.11 (a) and (b), the total pressure loss from the stator inlet to plane 2 at the rotor inlet is plotted. The loss is calculated by equation 5.2. The loss increases when the axial gap increases. In figure 6.11 (a), doubling the axial gap gives almost constant increment to the total pressure loss. The spanwise total pressure loss profile in figure 6.11 (b) reveals that an increase of losses happens before the shroud wall and from the midspan to the back flow area before the hub wall. The differences between cases in these areas are somewhat similar. An increase of total pressure loss due to increased axial gap has also been found by Jeong et al. (2006).

The flow development from the stator leading edge to the rotor leading edge is plotted in figure 6.12 as mass flow averaged values along the axial length l_{ax}. In case 5 there is a small step in acceleretion just before the maximum value. The flow accelerates smoothly in general to the maximum value, which is detected just before the trailing edge of the stator. The maximum Mach number increases when

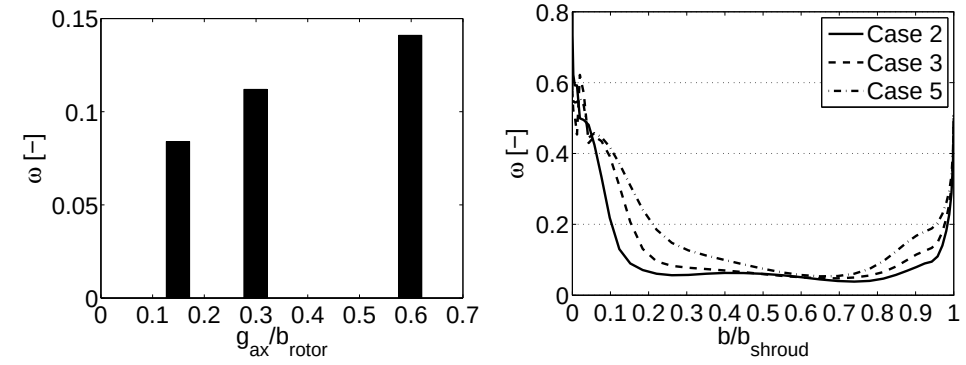

Figure 6.11: Total pressure loss from stator inlet to measurement plane 2 at the rotor inlet at low off-design conditions (shown in table 6.3). Mass flow averaged values (a) and mass flow averaged spanwise distribution (b). The calculated cases are presented in table 6.1.

the axial gap increases, whereas the Mach number at the rotor leading edge decreases when the axial gap increases. In case 2, the Mach number decreases from the maximum value quite smoothly until $0.25g_{ax}$, after which the Mach number is almost constant until the rotor leading edge. A negligble Mach number rise is seen just before the rotor leading edge in cases 2 and 3. The Mach number decreases from the maximum value less smoothly in case 3 than in case 2. The Mach number increases again approximately from $0.25g_{ax}$ to $0.54g_{ax}$. In case 5 the Mach number decreases quite smoothly, the minimum value is detected at $0.04g_{ax}$ and a second maximum at $0.41g_{ax}$.

In table 6.4, the modelled turbine diffusor performance is shown. Case 5 has the best diffusor performance and case 3 the worst. The difference between the peak and bottom values is 0.037.

Table 6.4: Off-design performance of the turbine diffusor with varying axial distance between the stator and the rotor at low off-design conditions (shown in table 6.3).

	Case 2	Case 3	Case 5
C_{pr} [-]	0.161	0.146	0.183

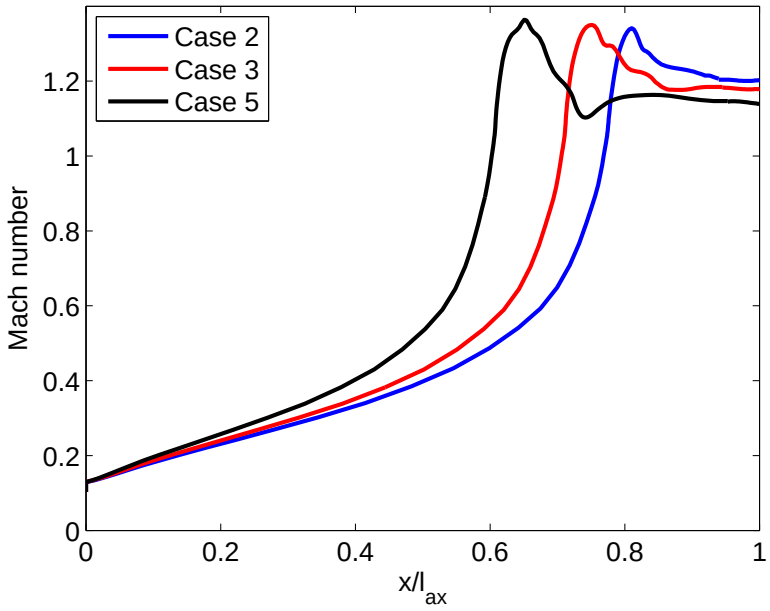

Figure 6.12: Flow development from the stator leading edge to the rotor leading edge at low off-design conditions (shown in table 6.3). The calculated cases are presented in table 6.1.

6.2.1 Stator throat flow field

The stator throat absolute flow angle and Mach number at the off-design conditions are plotted as spanwise averaged values in figures 6.13 (a) and (b), respectively. The flow angle distribution is similar in cases 2 and 5, being slightly lower than the designed 78°. In case 3 the flow angle is a little over the designed value for most of the flow channel length, which could be due to the higher non-dimensional wall distance, as shown in the previous chapter. A lower flow angle is seen in areas close to the hub and shroud in all cases.

In figure 6.13 (b), the Mach number distribution is highest in case 2. Case 3 has the lowest values for the large part of the flow channel. The distributions of cases 3 and 5 are in practice equal closer to the shroud. In general the Mach number decreases from the hub to the shroud, and the values are more than unity for a majority of the flow channel. If the possible effects of non-dimensional wall distance are included, all distributions are in general closer to each other.

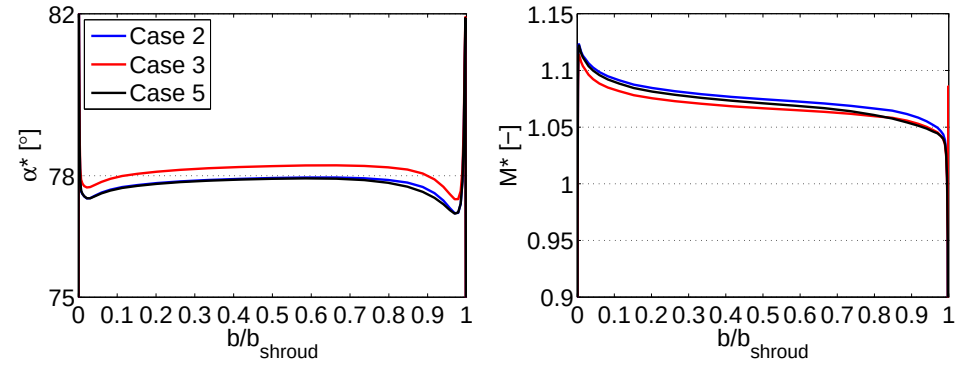

(a) (b)

Figure 6.13: Spanwise averaged stator throat (a) absolute flow angle and (b) absolute Mach number with variating stator rotor axial distance at low off-design conditions (shown in table 6.3). The calculated cases are presented in table 6.1.

6.2.2 Rotor inlet flow field

The spanwise averaged absolute flow angle distribution at the rotor inlet is plotted in figure 6.14 (a). A backflow is seen at the hub in every case. The distribution becomes flatter when the axial gap is decreased. An increase of the axial gap increases the flow angle before the backflow region and decreases the flow angle at the shroud.

In figure 6.14 (b), the spanwise averaged absolute Mach number distribution is plotted. For more than half of the spanwise direction, the Mach number decreases when the axial gap increases. It should be noted that the turbine rotor operates at transonic conditions.

The spanwise averaged axial velocity distribution is plotted in figure 6.14 (c). For most of the span, the differences between cases are negligible. A backflow region is seen at the hub in all cases. The increase of the axial gap decreases the axial velocity before the backflow region.

In figure 6.14 (d), the spanwise averaged tangential velocity distribution is plotted. Tangential velocity decreases when the axial gap increases in areas before the back flow area at the hub and before the shroud wall. The area of lower tangential velocity at the hub increases with the increasing axial gap. The maximum value moves towards the shroud when the axial gap increases.

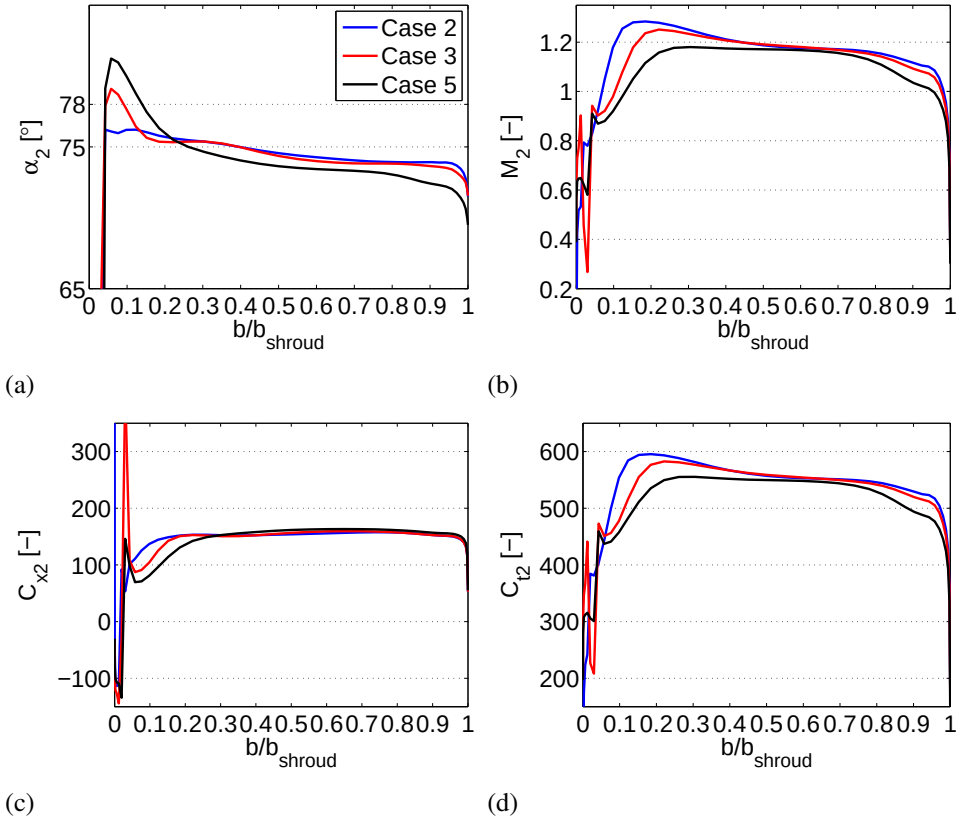

Figure 6.14: Spanwise averaged rotor inlet (a) absolute flow angle, (b) absolute Mach number, (c) axial velocity, and (d) tangential velocity with varying stator rotor axial distance at low off-design conditions (shown in table 6.3). The calculated cases are presented in table 6.1.

6.2.3 Pressure at the rotor surface

The pressure variations between the calculated cases at the rotor surface (hub, midspan and shroud) are plotted in figures 6.15 (a), (b) and (c). The pressure difference over the rotor blade is lowest at the hub, and the greatest pressure variations are seen at the midspan. The highest pressure differences are detected right after the leading edge.

Figure 6.15 (a) shows that the pressure at the pressure surface after the leading edge is the highest in case 2 and lowest in case 5. When the suction surface is examined, it can be seen that the highest pressure is in case 5 and the lowest or equal to the lowest in case 2 for more than 50% of the blade axial chord. At the midspan (figure 6.15 (b)), the pressure of case 5 is the highest after the leading

edge at the pressure surface. At the hub (figure 6.15 (c)), the pressure in case 2 is the lowest at the suction surface. Case 3 is slightly lower than case 5 in the beginning of the suction surface, but they are almost equal for the rest of the blade.

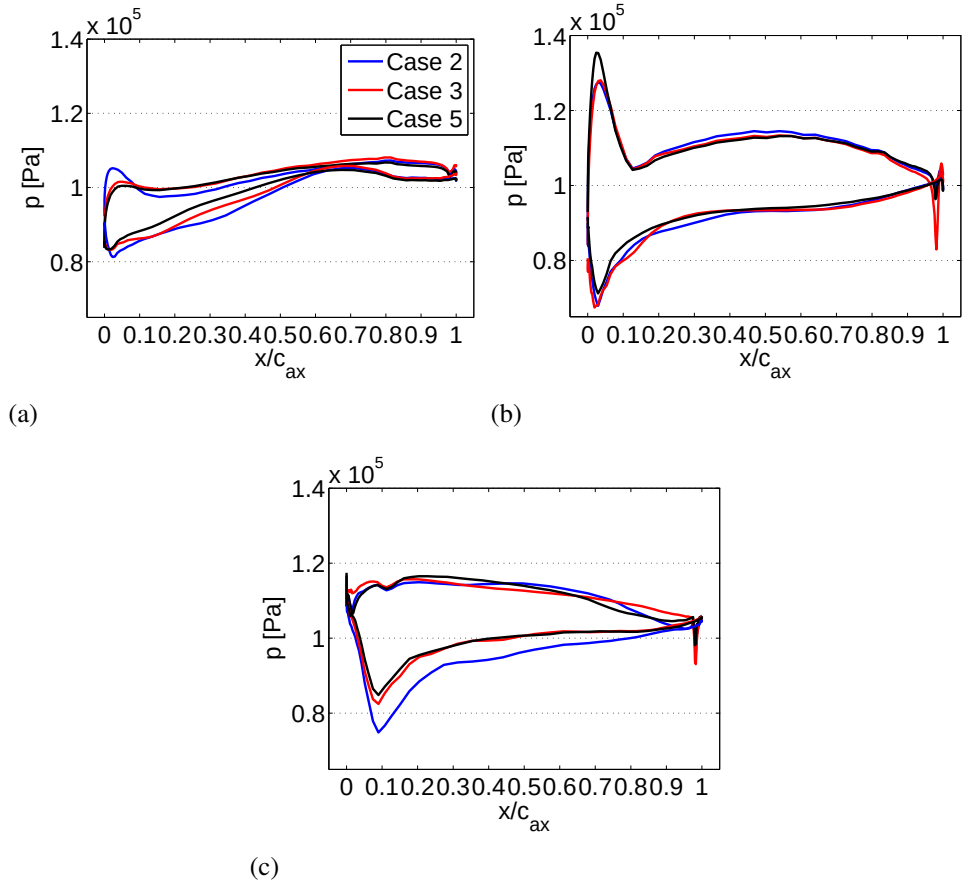

Figure 6.15: Pressure at the rotor surface at the hub (a), at the midspan (b), and at the shroud (c) at low off-design conditions (shown in table 6.3). The calculated cases are presented in table 6.1.

6.2.4 Rotor outlet flow field

In figure 6.16 (a), the spanwise averaged rotor outlet absolute flow angle at the off-design conditions is plotted. The increase of the axial gap increases the flow angle in over 70% of the span. The greatest differences are seen at the hub and after the midspan. The flow angle distributions are quite similar at the shroud.

The distribution becomes flatter when the axial gap increases.

The spanwise averaged rotor outlet absolute Mach number is plotted in figure 6.16 (b). At the hub, the increase of the axial gap slightly increases the Mach number. The distribution in case 5 is the most linear.

Spanwise averaged rotor outlet axial velocity at the off-design conditions is plotted in figure 6.16 (c). The distributions in cases 2 and 3 have relatively similar shapes. The distribution in case 5 differs from the others for the majority of the spanwise direction, and it is more linear than in cases 2 and 3. Closer to the shroud, all the cases have quite similar distributions. At the hub, the axial velocity decreases when the axial gap increases.

In figure 6.16 (d), spanwise averaged rotor outlet tangential velocity at the off-design conditions is plotted. At the hub, the velocity increases when the axial gap increases. The difference between minimum and maximum velocity decreases with the increasing axial gap.

The turbine efficiency at the rotor outlet is plotted from hub to shroud in figure 6.17 for all three different axial gaps. The performance is worst with the largest axial gap for most of the span until the shroud wall. The best performance is with the smallest gap for a majority of the span. At the hub, the performance penalty due to the increased axial gap is high with the largest axial gap. The differences between cases 2 and 3 are more stable for a majority of the span than the difference between them and case 5. With the largest axial gap in case 5, the performance difference decreases from the hub toward the midspan.

6.2.5 Comparison of design and off-design performance

In figure 6.18 (a), comparison of the turbine efficiency at the design and off-design conditions is presented with same axial gaps. The turbine efficiency drops more drastically at the off-design than at the design conditions. The efficiency decrement profile is more linear at the off-design conditions than at the design conditions.

The spanwise turbine efficiency distribution at the rotor outlet drops at the hub in both operating conditions when the axial gap increases, see figures 6.9 and 6.17. The differences between the diffuser performance minimum and maximum are almost twice as high at the off-design as at the design conditions, see tables 6.2 and 6.4.

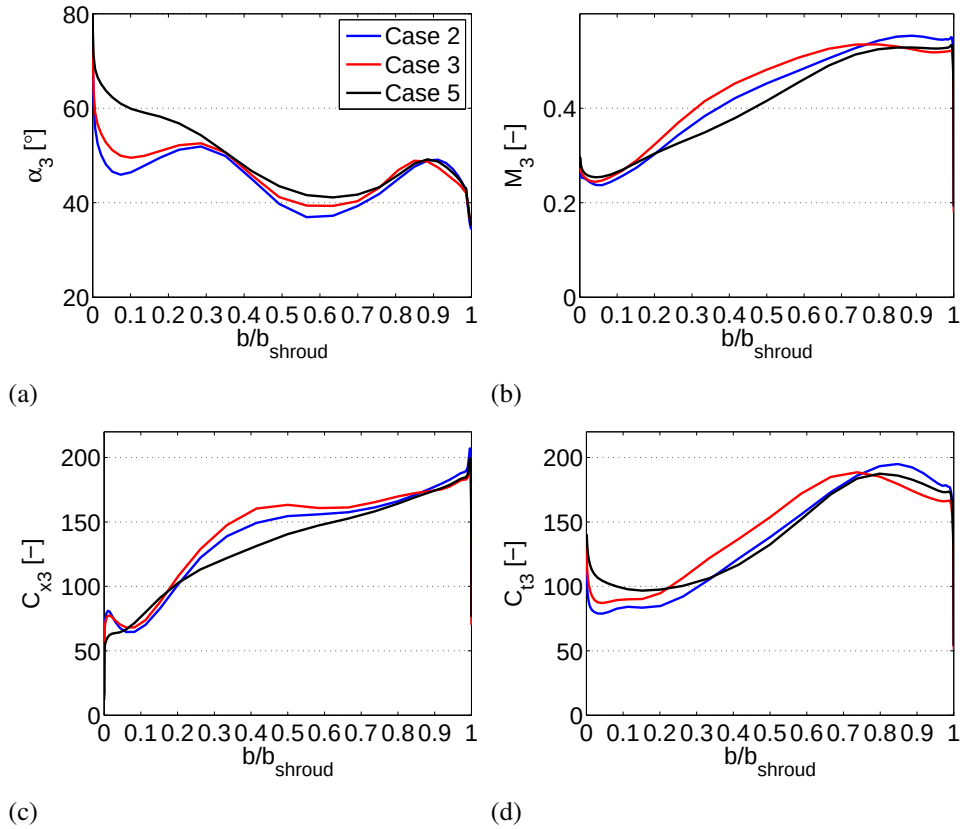

Figure 6.16: Spanwise averaged rotor outlet (a) absolute flow angle, (b) Mach number, (c) axial velocity, and (d) tangential velocity with variating stator-rotor axial distance at low off-design conditions (shown in table 6.3). The calculated cases are presented in table 6.1.

In figure 6.18 (b), the comparison of the total pressure loss at the rotor inlet in the design and off-design conditions is presented. The total pressure losses differ from each other when cases 2, 3 and 5 are compared at the design and off-design conditions. The increase of losses is almost linear at the off-design conditions, whereas the increase of losses at the design conditions accelerates when the axial gap is increased.

The Mach number maximum is seen just before the stator trailing edge in both operating conditions, see figures 6.4 (a) and (b) and 6.12. A small step in flow acceleration is seen at the design conditions and with the largest axial gap at the off-design conditions.

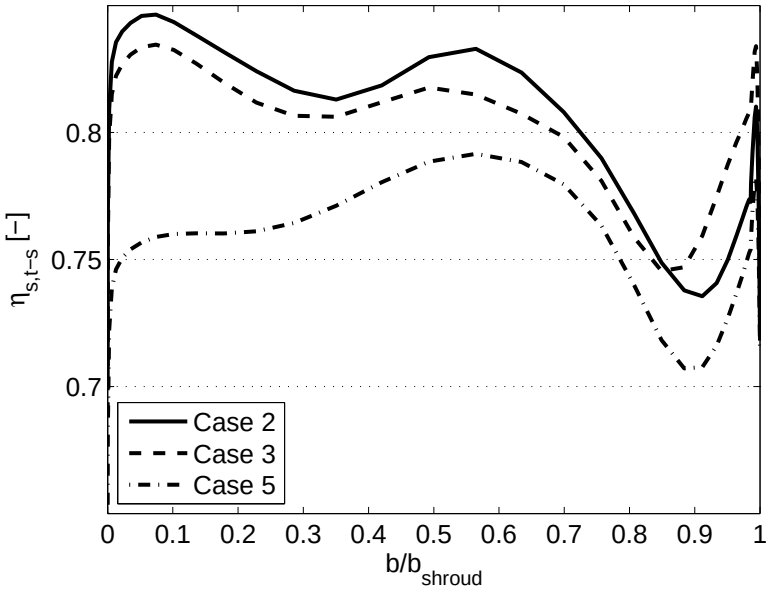

Figure 6.17: Spanwise distribution of isentropic total-to-static efficiency calculated from turbine inlet to rotor outlet by equation 6.2 at low off-design conditions (shown in table 6.3). The calculated cases are presented in table 6.1.

The flow at the stator throat is almost not at all affected in the design and off-design conditions by the changes of the axial gap. At the rotor inlet hub, the increase of axial gap increases the rotor inlet flow angle in both operating conditions, but reversed flow is only seen at the off-design conditions, see figures 6.6 (a) and 6.14 (a). At the shroud, the flow angle decreases when the axial gap increases in both conditions. The pressure variation is smallest at the hub in both operating conditions.

6.2.6 Conclusions and discussion

In the low pressure ratio and low rotating speed operating conditions the total-to-static efficiency decreases drastically when the axial gap is increased. The decrement is almost linear, which is in agreement with an other study from the literature. The differences in the spanwise total-to-static efficiency distributions are greatest at the hub in the case of the largest axial gap. At the shroud the performance with the medium axial gap is the best, although overall the efficiency decreases with the increasing axial gap. The best diffusor performance is seen

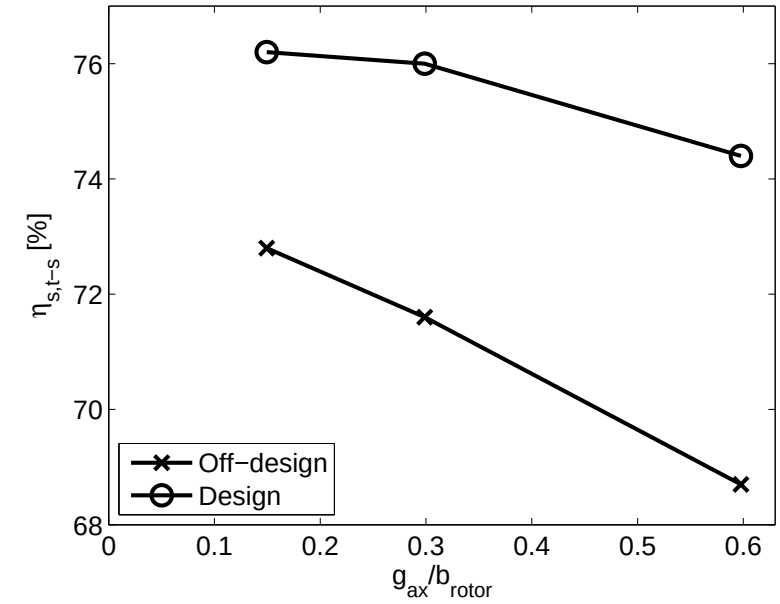

(a)

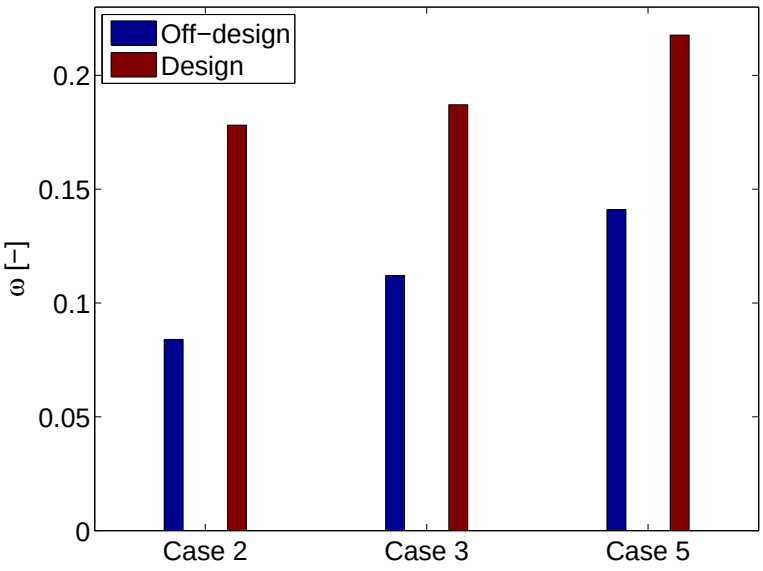

(b)

Figure 6.18: Comparison of the turbine efficiency in design and low off-design conditions (a) and comparison of the total pressure loss from turbine inlet to rotor inlet at design and low off-design conditions (b). The calculated cases are presented in table 6.1

in the case with the largest axial gap. The measured turbine efficiency in the intermediate pressure ratio and rotating speed operating conditions was higher than calculated in the low pressure ratio and low rotating speed operating conditions. The measured turbine efficiency was slightly lower than the calculated efficiency in the design operating conditions. The results agree with the assumption that the measured efficiency should be between the calculated design and off-design performance. Therefore the measurements give more reliability to the modelling. Overall, the efficiency of the turbine in the off-design operating conditions is higher than is usually presented in the literature for supersonic axial turbines.

The total pressure losses from the turbine inlet to the rotor inlet increase when the axial gap increases, and doubling the axial gap generates almost a constant increment of total pressure loss. The changes in total pressure loss and efficiency behave in a similar manner, indicating that efficiency is linearly dependent on the total pressure losses in the low off-design conditions.

The flow accelerates smoothly from the stator inlet to the maximum Mach number in all cases. The maximum value detected a little before the trailing edge of the stator increases when the axial gap increases, although the value at the rotor leading edge decreases with the increasing axial gap. A second local maximum appears with two of the largest axial gaps in the area between the stator and the rotor.

The stator throat is moved from the designed position to the upstream direction towards the turbine inlet. The flow at the throat is affected very little by the axial gap variation in the low off-design conditions.

At the rotor inlet, the flow turns more at the hub when the axial gap increases, and an area of backflow is detected in all axial gaps. At the shroud, the flow is less turned when the axial gap is increased. The maximum value of the Mach number and tangential velocity move towards the shroud when the axial gap increases. Overall, tangential velocity and the Mach number decrease when the axial gap increases.

The rotor surface pressure at the hub is affected by the variation of the axial gap. The increase of the axial gap decreases the pressure right after the leading edge at the pressure surface, and increases the pressure in approximately half of the axial chord length at the suction surface (starting after the leading edge). At the midspan, the pressure is affected only little by the changes in the axial gap. At the shroud, the pressure is lowest with the smallest axial gap at the suction surface,

and the increase of the axial gap increases the pressure, especially between the smallest and intermediate gaps.

At the rotor outlet, the increase of the axial gap increases the absolute flow angle, especially at the hub, but also after the midspan. A flatter distribution is also seen when the axial gap increases. At the hub, the absolute Mach number increases slightly when the axial gap increases. The axial velocity decreases at the hub when the axial gap is increased, which is opposite to the tangential velocity behaviour. It should be noted, however, that this kind of behaviour is stronger and happens in a longer spanwise area in the case of tangential velocity. The difference between the maximum and minimum tangential velocity decreases with the increasing axial gap. The Mach number and axial velocity distributions are most linear with the maximum axial gap.

The turbine efficiency drops in both design and off-design operating conditions when the axial gap increases, but the drops are more drastic in the off-design conditions. The decrease of turbine performance is clear at the hub when the axial gap increases. The flow acceleration is affected only little by the operating conditions, whereas the spanwise flow angle profiles at the rotor inlet and outlet are affected more. Also the distribution of the rotor loading changes, and the maximum pressure variation moves from the shroud (design) to the midspan (off-design).

As a conclusion for the objective of the off-design modelling, it can be concluded that the objective of studying the effect of stator-rotor axial distance on the studied turbine type and improvement of efficiency in the off-design conditions has been reached.

6.3 Modelling of a supersonic stator with pulsatile inlet flow

In this section, a supersonic turbine stator is modelled with three different methods: quasi-steady, time-accurate, and time-accurate with pulsatile inlet conditions. The effects of different modelling approaches to the stator performance are studied. Also the effects of pulsating inlet flow to the stator flow field and performance are studied. Part of the results presented in this section are also presented in Grönman et al. (2010). The modelled stator has the same geometry as in the whole turbine modelling. Only one stator channel is modelled. The inlet conditions, or average inlet conditions in the case of the pulsatile inlet, are the design inlet conditions of the whole turbine in one-dimensional design. Three mass flow pulses are modelled in order to have the effects of pulsation well established in the calculation. The mass flow pulsation is defined by equation 4.24, and it is shown

in figure 4.1. The outlet pressure from the one-dimensional design is higher than in the whole turbine model, which leads to the pressure ratio of 3.8.

The grid is almost equal to the stator grid used in the previous sections. The outlet of the calculation domain is located at the similar distance from the trailing edge as the inlet domain from the leading edge (approximately 2.7 times the stator axial chord). This position of the outlet domain makes the number of cells slightly higher than in the stator grid in the previous sections. The number of cells from the inlet domain to the trailing edge is unchanged. The used boundary conditions and measurement planes are shown in figure 6.19. The positions of inlet and outlet domains and measurement plane 1 in the figure are not the actual ones, which are further away from the stator flow channel. The measurement locations are defined as follows: 1) inlet, A) throat, B) diverging section, C) trailing edge, D) $l_{TE}/b_{stator} = 0.09$, E) $l_{TE}/b_{stator} = 0.17$, and F) $l_{TE}/b_{stator} = 0.26$. The measurement plane E is equal to the inlet of the rotor at the design turbine configuration (case 2) shown in the previous sections. The mass flow averaged values of the studied parameters are defined in these locations. Either spanwise averaged distributions or a single averaged value are used.

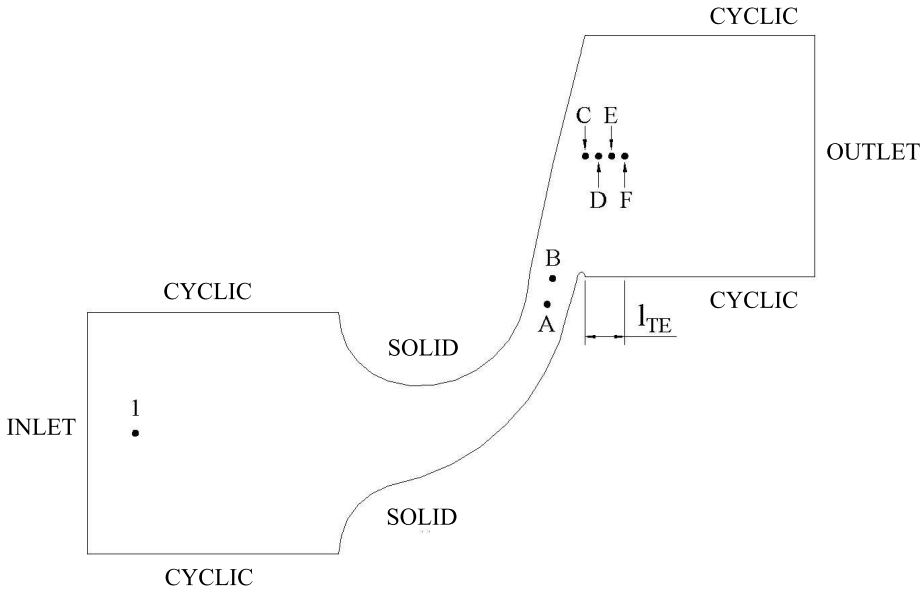

Figure 6.19: Stator hub geometry and calculation boundaries. Inlet, outlet and plane 1 are not in actual positions relative to the stator flow channel. The definitions of the different "measurement planes" are 1) inlet, A) throat, B) diverging section, C) trailing edge, D) $l_{TE}/b_{stator} = 0.09$, E) $l_{TE}/b_{stator} = 0.17$, and F) $l_{TE}/b_{stator} = 0.26$.

The averaged values for the variables in the time-accurate modelling with and without pulsating inlet conditions are calculated as an average over the sum of every time-step

$$\bar{\rho} = \frac{1}{I} \sum_{i=1}^{I} \rho_i \tag{6.3}$$

where I is the number of time steps, and i is the number of the time step. Stator efficiency is used to study the stator performance, and it is defined as

$$\eta_{\text{stator}} = \frac{T_1 - T_2}{T_1 - T_{2\text{s}}} \tag{6.4}$$

where T_1 is the static inlet temperature, T_2 is the static temperature at the chosen measurement plane, and $T_{2\text{s}}$ is the static isentropic temperature at the chosen measurement plane.

The results of the three modelled cases are compared in table 6.5, where the time-accurate and pulsatile inlet results have been calculated from time-averaged values. The efficiencies have been calculated starting from the trailing edge in positions C, D, E and F. The efficiency decreases when the distance from the trailing edge increases, which is common for all the modelling approaches. The efficiencies of quasi-steady modelling are slightly lower than those of time-accurate and pulsatile-inlet modelling, except in plane D. This is opposite to part of the results of Lam et al. (2002), as they had lower than steady flow efficiency for the whole radial turbine with two efficiency calculation methods out of three, whereas one method overestimated the efficiency. Cycle-mean efficiency is stated to be higher than steady-state efficiency by Hakeem et al. (2007). The efficiency calculation methods that predicted unsteady performance better than steady state performance were based on integrating the efficiency over one pulse period and taking the average over the integration. Steady state performance has been reported to be better than pulsatile flow performance in a paper of Daneshyar et al. (1969).

6.3.1 Effects of different modelling approaches on the stator flow field

Spanwise averaged absolute flow angle distributions at different positions are plotted in figures 6.20 (a) to (f). The effects of different modelling approaches are compared, and figures 6.20 (a) and (b) show that the absolute flow angle at

Table 6.5: Performance of the stator with varying axial distance from the stator trailing edge and effects of different modelling approaches. Time-accurate and pulsatile inlet results have been calculated from averaged values (equation 6.3).

	Quasi-steady	Time-accurate	Pulsatile inlet
$\eta_{\mathrm{stator}}(C)$ [%]	91.6	91.7	91.7
$\eta_{\mathrm{stator}}(D)$ [%]	88.5	88.4	88.3
$\eta_{\mathrm{stator}}(E)$ [%]	87.3	87.5	87.5
$\eta_{\mathrm{stator}}(F)$ [%]	86.3	86.7	86.7

the throat and diverging section do not vary between the different modelling approaches. From the trailing edge in figure 6.20 (c) until measurement plane F in figure 6.20 (f), the absolute flow angle distribution after the hub area is almost similar in the time-accurate and pulsatile inlet modelling. At the hub, the flow angle becomes slightly lower with the pulsatile inlet than with the other modelling approaches, especially in positions E and F. The flow angle distribution from the trailing edge with quasi-steady modelling deviates slightly from the other modelling approaches. It can be seen in figures 6.20 (c) to (f) that the flow at the hub side turns more when the axial distance from the trailing edge increases.

The radially averaged absolute Mach number distributions at different positions are plotted in figures 6.21 (a) to (f). Figures 6.21 (a) and (b) show that the absolute Mach number distribution inside the stator flow channel is not affected by the modelling approach. The Mach number distribution is slightly the highest or equal to highest after the hub with the pulsatile inlet from the trailing edge until measurement plane F, except for measurement plane D (figure 6.21 (d)), where the Mach number is the highest at the midspan with the quasi-steady modelling. The quasi-steady modelling produces the lowest Mach number distributions in planes E and F between the hub and the midspan. The area of slower flow at the hub increases when the axial distance from the trailing edge increases. This can be seen when figures 6.21 (c) and (f) are compared. The maximum Mach number decrease is also seen with increasing the axial distance from the trailing edge.

6.3.2 Effects of pulsatile inlet flow to the stator flow field

The mass flow at five positions in the stator calculation domain is plotted in figure 6.22 as a function of time. The mass flow pulsation amplitude is lower at the stator throat (line A) than at the inlet. Downstream from the throat, the amplitude does

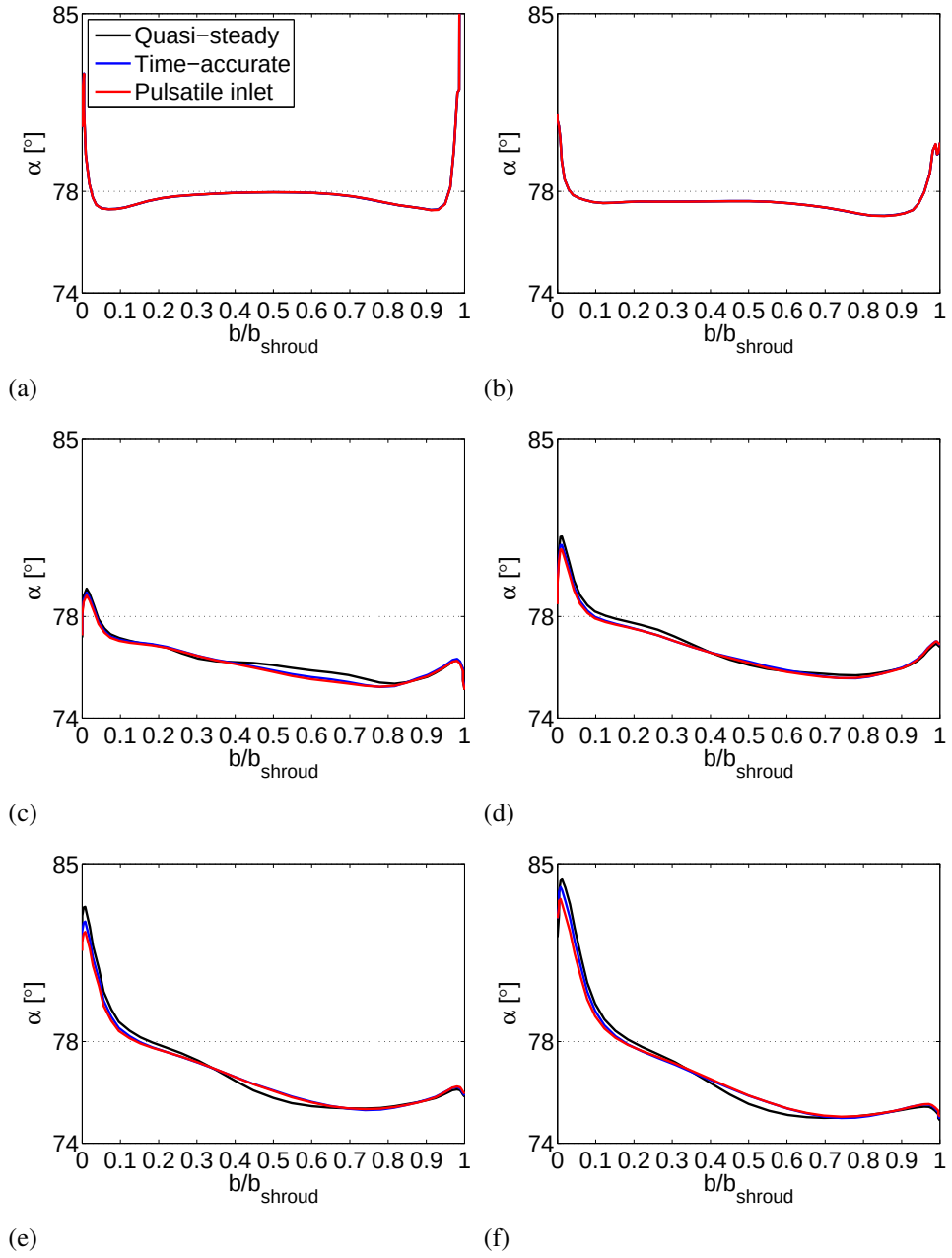

Figure 6.20: Radially averaged absolute flow angles with different modelling approaches at positions (a) A, (b) B, (c) C, (d) D, (e) E, (f) F. The measurement plane positions A to F are presented in figure 6.19.

not have such dramatic changes. In a paper of Denos et al. (2001), the fluctuation

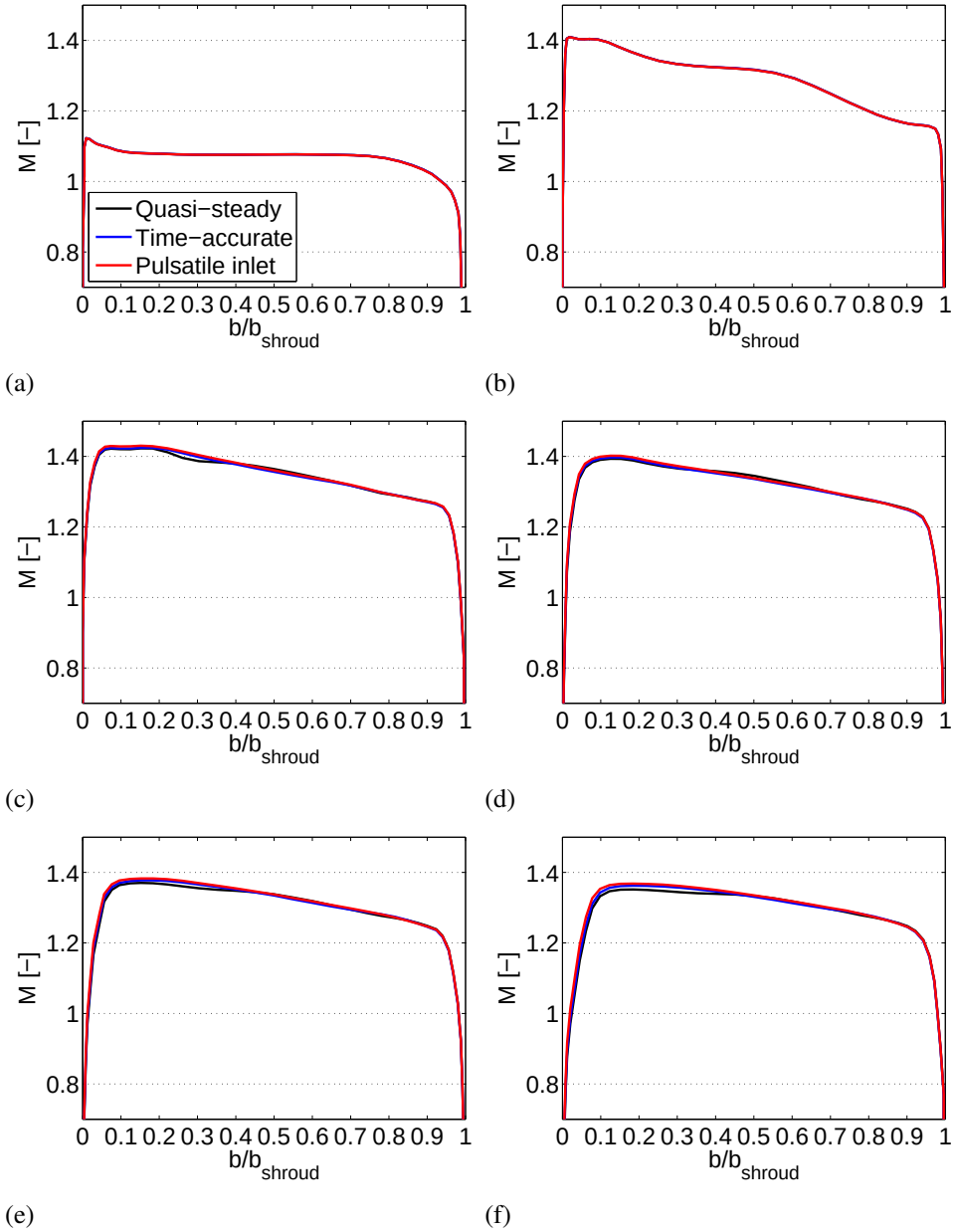

Figure 6.21: Radially averaged absolute Mach number with different modelling approaches at positions (a) A, (b) B, (c) C, (d) D, (e) E, (f) F. The measurement plane positions A to F are presented in figure 6.19.

amplitude is reported to decrease at the blade leading edge region when the axial gap increases.

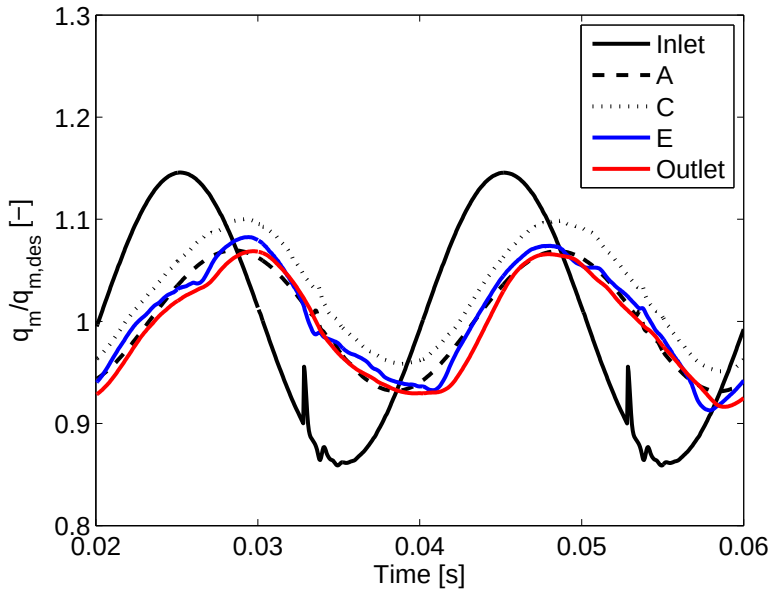

Figure 6.22: Development of mass flow pulse from the stator inlet to the stator outlet as a function of time. The measurement plane positions are depicted in figure 6.19.

In figure 6.23, the sonic line transition to the upstream direction is illustrated. The position of the designed throat (sonic line) is drawn with a red line, and the actual position of the throat is shown as a blue curved line at the midspan. In the figure, the actual throat is strongly curved to the upstream direction. Throat transition is also seen when the whole turbine stage is modelled as an over unity Mach number at the designed throat (figures 6.5 (b) and 6.13 (b)). The curved sonic line is most likely due to the curved profile of the stator flow channel upstream from the throat. Reichert and Simon (1997) proposed to design a nearly parallel and uncurved throat for a supersonic radial turbine nozzle in order to have a straight sonic line.

The mass flow averaged absolute flow angle at various positions in the stator calculation domain is plotted in figure 6.24 (a) as a function of time. The flow angle at the throat (A) or diverging section (B) does not vary almost at all when the mass flow pulse goes through the stator flow channel, whereas the behaviour downstream from the trailing edge (C) is more pulsatile. The flow angle decreases when the distance from the trailing edge increases, as seen in lines D and E, although the difference between the two furthest measurement planes is small compared to their difference with the trailing edge flow angles.

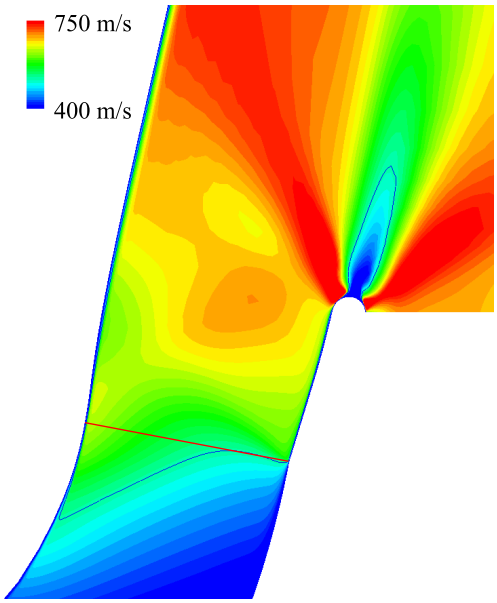

Figure 6.23: Contours of absolute flow velocity distribution at the stator channel and the contour of Mach number one (blue line) at the midspan. Also shown in the figure is the designed throat position (red line). The plot is from averaged results of pulsatile inlet modelling.

Mass flow averaged axial velocity at various positions in the stator calculation domain is plotted in figure 6.24 (b) as a function of time. The axial velocity pulsates slightly at the throat and the diverging section as a function of time. Steeper variation is seen at the trailing edge and after the trailing edge. The axial velocity accelerates from the throat until the trailing edge. After that a clear drop is seen between the trailing edge (C) and measurement plane D. The axial velocity profiles are in practice identical between planes D and E.

Mass flow averaged tangential velocity at various positions in the stator calculation domain is plotted in figure 6.24 (c) as a function of time. The tangential velocities at the throat (B) and diverging section (C) pulsate more clearly than the axial velocities. The lowest calculated tangential velocities at the bottom of the pulse are slightly higher in plane B than in plane C, but otherwise the tangential velocity accelerates from the throat until the trailing edge. The velocity also decelerates from the trailing edge to plane D and further to plane E. The deceleration from plane D to E is much slower than from the trailing edge to plane D, though the distance between the trailing edge and plane D is equal to the distance between planes D and E.

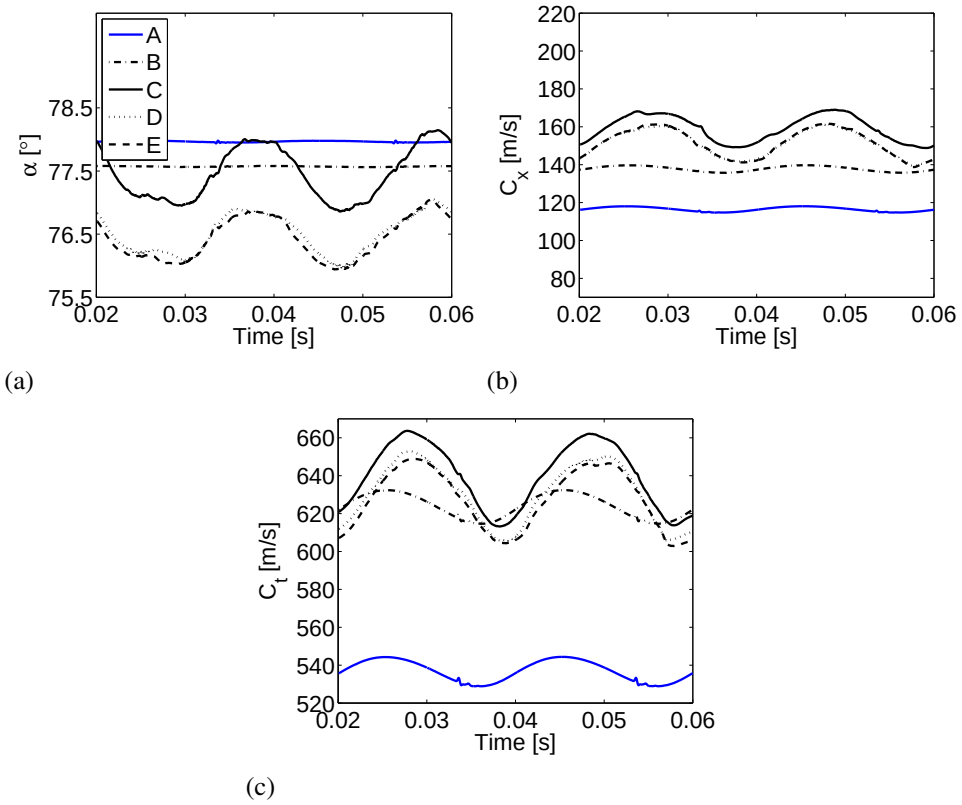

Figure 6.24: Development of mass flow averaged absolute flow angle (a), axial velocity (b), and tangential velocity (c) as a function of time at five positions along the stator calculation domain. The measurement plane positions A to E are depicted in figure 6.19.

The contours of absolute flow angle at measurement plane E at six different time steps are plotted in figures 6.25 (a) to (f). Two shock waves propagate from the trailing edge, and one of them is seen in every figure of this series on the left side of the figure as an spanwise area of higher flow turning. The flow angle is higher at the hub than at the shroud along the whole presented time span. In figure 6.25 (a), a lower turning area (blue) from the midspan to the shroud is seen. In the next figure, 6.25 (b), the low turning area is decreased, and it decreases even more in figure 6.25 (c). It starts to develop again in figure 6.25 (d), and keeps developing through figures 6.25 (e) and (f). Qualitatively, the flow development in figures 6.25 (a) to (f) is in agreement with the mass flow averaged flow angle distribution as a function of time in figure 6.24 (a) (line E).

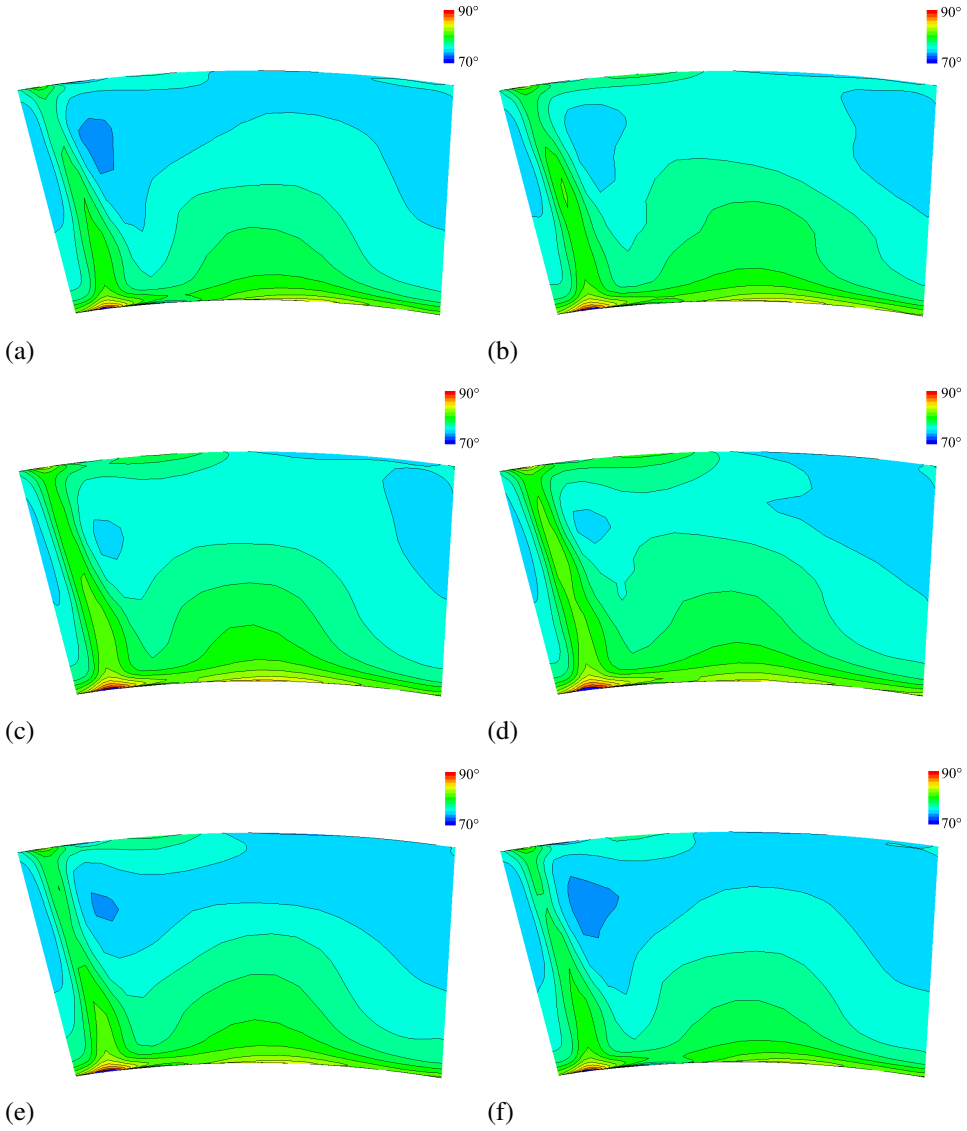

Figure 6.25: Contours of absolute flow angle at measurement plane E at time steps 0.03s (a), 0.0335s (b), 0.037s (c), 0.0405s (d), 0.044s (e) and 0.0475s (f). Measurement plane E is equal to the inlet of the rotor at the design configuration of the whole turbine (case 2 in table 6.1 and figure 6.1) and is shown in figure 6.19.

6.3.3 Effects of pulsatile inlet flow on stator performance

In this chapter, the performance of the stator is studied as a function of time in two measurement planes, C and E. The isentropic (ideal) total-to-static pressure ratio presented in figure 6.26 (a) is calculated as

$$\pi_s = \frac{p_{t1}}{p} = \left(1 + \frac{\gamma - 1}{2} M^2\right)^{\frac{\gamma}{\gamma - 1}} \tag{6.5}$$

where the Mach number M at measurement plane C or E is calculated from the numerical results of each studied time step. The pressure ratio π in figure 6.26 (a) is defined as

$$\pi = \frac{p_{t1}}{p} \tag{6.6}$$

The total-to-static pressure ratio as a function of time is plotted in figure 6.26 (a) at two measurement planes, trailing edge (C) and in the position of the rotor leading edge in the design configuration of the whole turbine modelling (E). Also the ideal pressure ratio (from equation 6.5) is compared to the results of CFD. The modelled pressure ratio follows the sinusoidal shape of the inlet pulse. In the case of CFD, the pressure ratio increases when the distance from the trailing edge increases, which is opposite to the results of the isentropic pressure ratio. The pressure ratio from CFD is higher than the isentropic one.

Stator efficiency as a function of time is plotted in figure 6.26 (b) at measurement planes C and E, during one pulse period. The pulse follows the sinusoidal shape of the inlet pulse, but the peak value is seen close to the time of the minimum pressure ratio in figure 6.26 (a). The efficiency drops from the trailing edge to measurement plane E during the whole pulse period.

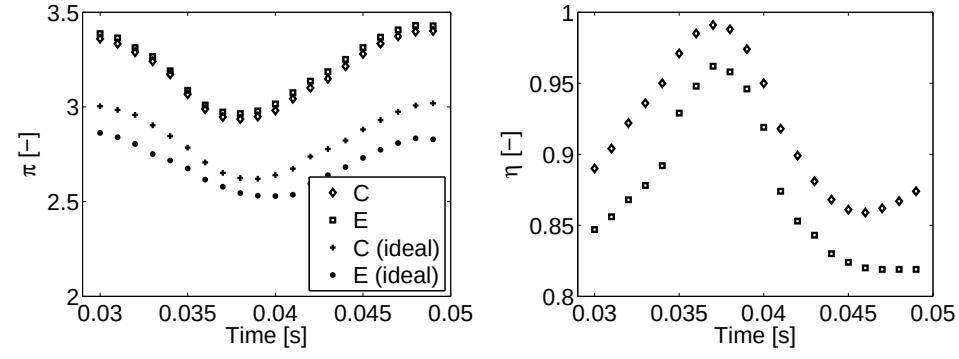

(a) (b)

Figure 6.26: Stator pressure ratio as a function of time (a) and stator efficiency as a function of time (b) during one pulse period. The measurement plane positions C and E are depicted in figure 6.19.

The stator pressure ratio as a fuction of inlet mass flow during one pulse period is plotted in figure 6.27 (a). Hysteresis-like behaviour is seen during the pulse period. Similar kind of behaviour has also been found in several papers studying mixed flow turbines, e.g. Karamanis and Martinez-Botas (2002), Palfreyman and Martinez-Botas (2005), Rajoo and Martinez-Botas (2007), and Hakeem et al. (2007). The behaviour in the case studied here is relatively symmetrical compared to the studies in the literature with rotating machines.

Stator efficiency as a function of stator inlet mass flow is plotted in figure 6.27 (b). The efficiency shows hysteresis-like behaviour. The area covered by the pulse period is larger at measurement plane E than at the trailing edge. Hysteresis in the efficiency behaviour has been also reported by Karamanis and Martinez-Botas (2002), Lam et al. (2002), Palfreyman and Martinez-Botas (2005), and Hakeem et al. (2007). The efficiency is lower downstream from the trailing edge (plane E) than at the trailing edge at the same phase during the pulse period.

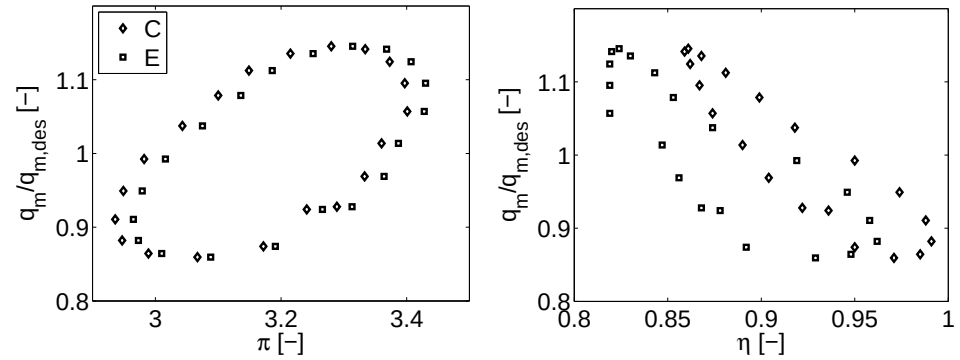

(a) (b)

Figure 6.27: Stator pressure ratio as a function of inlet mass flow during one pulse period (a) and stator efficiency as a function of inlet mass flow during one pulse period (b). Measurement plane positions C and E are depicted in figure 6.19.

6.3.4 Conclusions and discussion

Overall, the time-accurate and pulsatile inlet mass flow modelling approaches increase slightly the average stator efficiency of the axial turbine stator when compared to quasi-steady modelling with the same average mass flow, inlet total enthalpy and outlet static pressure. This result in the case of the pulsatile inlet flow is different from that assumed on the basis of previous studies. The result could

be due to the averaging process which is close to the averaging method that has been reported to predict pulsatile flow better than steady state efficiencies. In the flow field comparison, the flow inside the stator is not affected by the modelling approach, but downstream from the trailing edge there are small differences between the approaches. Especially the results of quasi-steady modelling differ slightly from other results.

The mass flow pulsation amplitude is decreased at the throat, after that the amplitude does not have such dramatic changes. The absolute flow angle does not pulsate almost at all in the stator throat and the diverging section. The pulsation is clear downstream from the trailing edge, and the average flow angle decreases when the distance from the trailing edge increases. The absolute flow angle decrement is much smaller from $l_{TE}/b_{stator} = 0.09$ to $l_{TE}/b_{stator} = 0.17$ than it is from the trailing edge to $l_{TE}/b_{stator} = 0.09$. The flow angle is higher at the hub than at the shroud for the whole pulsating period.

The axial velocity pulsates slightly in the throat and the diverging section, but stronger pulsation is seen at the trailing edge and after it. The changes in tangential velocity are more drastic than the changes in axial velocity. The tangential and axial velocities behave in general similarly. First the flow velocity accelerates from the throat to the trailing edge and then the velocity decelerates away from the trailing edge. The highest decrease in tangential and axial velocity is seen after the trailing edge. A further increase of axial distance from the trailing edge does not affect axial velocity distribution almost at all. Slightly bigger differences are still seen at the tangential velocity.

The total-to-static pressure ratio and the efficiency follow the sinusoidal shape of the inlet flow. The pressure ratio increases slightly after the trailing edge. The isentropic pressure ratio is lower than the corresponding pressure ratio in the CFD modelling, and it also decreases downstream from the trailing edge. This isentropic pressure ratio behaviour opposite to the CFD results is due to the decreasing Mach number downstream from the trailing edge. This behaviour can be expected because the equation of the isentropic pressure ratio is for duct flows where the Mach number increases downstream in the case of supersonic flow and convergent-divergent nozzle. It can be concluded that the analytically calculated pressure ratio is relatively poorly predicted in the studied case with the used method.

The efficiency decreases away from the trailing edge during the whole pulse period. Hysteresis-like behaviour is detected when the pressure ratio is plotted as a function of inlet mass flow over one pulse period. This is similar to the hysteresis-

like behaviour in the mixed flow turbine studies found in the literature, although the results are more symmetrical in the current study, probably because of the non-rotating stator. Hysteresis-like behaviour is also detected for efficiency as a function of inlet mass flow over one pulse period. This behaviour is also in accordance with the literature. The variation of efficiency during one pulse period is higher downstream from the trailing edge than at the trailing edge.

As a final conclusion based on the results shown in this chapter, it can be stated that the objective of studying the effect of pulsating inlet flow on the flow field and performance of a supersonic axial turbine stator has been reached.

7 Summary and recommendations

More efficient turbocharger designs are desired in large diesel engines in order to lower the emissions. Flow inside the turbine becomes relatively easily supersonic with higher pressure ratios if only one turbine stage is used. Also limited space can be one constraint in the design process. The use of a supersonic axial turbine is one answer to these requirements. Compared to subsonic axial turbines of same power, supersonic axial turbines can be designed in smaller physical size. Usually a subsonic axial turbine stage still works with higher efficiency than a supersonic one. Production costs for one supersonic turbine are, however, lower than for two subsonic turbine stages. Since supersonic axial turbines have typically low degree of reaction, they create lower axial forces to the bearings compared to high reaction turbines.

In this thesis, the effect of changing the stator-rotor axial gap in a small high (rotating) speed supersonic axial flow turbine was studied in both design and off-design conditions. Also the effect of using pulsatile mass flow at the supersonic stator inlet was studied. The reliability of the modelling was studied and conclusions were drawn, keeping the possible effects of numerical error in mind.

The literature review showed a lack of scientific results about the effect of the stator-rotor axial gap on low reaction supersonic axial turbines. The review of the modelling of pulsatile mass flow in a supersonic axial turbine stator also showed lack of studies.

The effect of grid density and non-dimensional wall distance was studied in the beginning of the numerical reliability section. The grid was seen to be grid-dependent even with the largest studied grid. Also the non-dimensional wall distance had an effect on the results of modelling.

Later in the numerical reliability section, the used code Finflo was validated by using measurements published in the literature. The modelling results showed that the code was capable of modelling shock waves with certain limitations with compressions and reflections from surfaces, although it was considered that the use of a smaller non-dimensional wall distance could lead to better modelling results.

The modelling of a supersonic stator was compared to the analytical calculations of the shock wave angle in the end of the numerical reliability section. The results showed that the trailing edge shock wave was modelled well in the beginning, but the results deviated from each other later on in the flow channel when the angle of

the numerical results decreased.

In the beginning of the numerical results section, five different turbine configurations with five different stator-rotor axial gaps were modelled by 3-dimensional CFD under turbine design conditions. To gain more knowledge about the performance of the studied turbine type under off-design conditions with different axial gaps, three turbine configurations were modelled with a low rotating speed and pressure ratio. The turbine efficiency measurement results from the intermediate off-design conditions, with intermediate rotating speed and pressure ratio, gave more reliability to the modelling results. The main findings of the whole turbine stage modelling study were:

1. The total-to-static efficiency of the turbine decreased when the axial gap was increased in both design and off-design conditions.

2. The turbine efficiency decrement accelerated at the design conditions when the axial gap increased.

3. An almost linear efficiency curve was found at the off-design conditions as a function of the axial gap, showing a decrease in the efficiency with the increasing axial gap.

It was concluded that the penalty in the turbine performance when the axial gap increased was mainly due to increased total pressure losses between the stator and the rotor. Some increasing extra losses may also have been caused at the design conditions by the increased hub side rotor incidence and lower axial velocity. The importance of having the smallest possible axial gap is more pronounced at the off-design than at the design conditions. The author would recommend a smallest possible axial gap to be used for this turbine type. The objectives of studying the effect of stator-rotor axial distance in the design and off-design conditions and the improvement of the efficiency were reached in this study. It was also concluded that the efficiency of the turbine in the design and off-design conditions is higher than is usually presented in the literature for supersonic axial turbines. There is still a need for additional scientifically valid measurements in both design and off-design conditions, and this is planned to be filled in the future when a test rig is available. Also the modelling of the turbine in the measured 28500 rpm off-design point is planned as future work. Even though the study of the whole turbine stage has been made for a turbine designed for turbocharger, these results can also be applied to some extent in similar turbines operating for example in space rocket engines.

Later in the numerical results section, one supersonic axial turbine stator was modelled in quasi-steady, time-accurate, and time-accurate with pulsatile inlet flow

conditions. The effect of different modelling approaches on the stator performance and flow field, and the effect of pulsatile inlet flow on the stator flow field and performance were studied. The stator geometry was the same as the one used in the whole turbine modelling. The main findings of the stator study were the following:

1. The flow inside the stator was not affected by the modelling approach.
2. The amplitude of the mass flow pulsation was decreased at the stator throat.
3. Variations of the total-to-static pressure ratio and the stator efficiency had sinusoidal shapes as a function of time.
4. The total-to-static pressure ratio and stator efficiency showed hysteresis-like behaviour as a function of inlet mass flow over one pulse period.

The efficiencies that were calculated on the basis of the time-averaged values with pulsatile inlet flow or time-accurate modelling were overall slightly overestimated. In the case of pulsatile inlet flow, this could be due to the averaging process, which was close to averaging process that has been reported to overestimate turbine performance in pulsatile flow conditions. Based on the current study, the author would suggest that a supersonic stator could be used in an axial turbocharger turbine. The objectives of studying the effect of pulsating inlet flow on the flow field and performance of the stator were reached in this study. As a recommendation for future work, it would be fruitful to implement the pulsatile inlet flow model for the full turbine stage modelling.

The first scientific contribution of this work is the use of a low reaction supersonic axial turbine in a turbocharger and its modelling in design and off-design conditions with variating stator-rotor axial distances. The second scientific contribution is the time-accurate modelling of a supersonic stator with pulsatile inlet flow.

References

van Albada, G.D., van Leer, B., and Roberts Jr., W.W. (1982). A Comparative Study of Computational Methods in Cosmic Gas Dynamics. *Astronomy and Astrophysics*, 108, pp. 76–84.

Anderson, J.D. (1991). *Fundamentals of Aerodynamics*, 2nd edn. New-York: McGraw-Hill.

Andersson, S. (2007). A Study of Tolerance Impact on Performance of a Supersonic Turbine. In: *43rd AIAA/ASME/SAE/ASEE Joint Propulsion Conference & Exhibit*, AIAA 2007-5513. Cincinnati, OH, USA, July 8-11, 2007.

Andersson, S., Lindeblad, M., and Wåhlén, U. (1998). Performance Test Results for the Vulcain 2 Supersonic/Transonic Turbine. In: *34th AIAA/ASME/SAE/ASEE Joint Propulsion Conference*. Cleveland, OH, USA, July 12-15, 1998.

Busby, J.A., et al. (1999). Influence of Vane-Blade Spacing on Transonic Turbine Stage Aerodynamics: Part II - Time-Resolved Data and Analysis. *Journal of Turbomachinery*, 121, pp. 673–682.

Chien, K.Y. (1982). Predictions of Channel and Boundary-Layer Flows with a Low-Reynolds-Number Turbulence Model. *AIAA Journal*, 20(1), pp. 33–38.

Costall, A., et al. (2006). Assessment of Unsteady Behavior in Turbocharger Turbines. In: *Proceedings of ASME Turbo Expo 2006: Power for Land, Sea and Air*, GT2006-90348. Barcelona, Spain, May 8-11.

Daneshyar, H., et al. (1969). A Comparison of the Performance of Three Model Axial Flow Turbines Tested Under Both Steady and Pulse Flow Conditions. *Proceedings of the Institution of Mechanical Engineers*, 184, pp. 1119–1133.

Denos, R., et al. (2001). Investigation of the Unsteady Rotor Aerodynamics in a Transonic Turbine Stage. *Journal of Turbomachinery*, 123, pp. 81–89.

Dorney, D.J., Griffin, L.W., and Gundy-Burlet, K.L. (2000a). Simulations of the Flow in Supersonic Turbines with Straight Centerline Nozzles. *Journal of Propulsion and Power*, 16, pp. 370–375.

Dorney, D.J., Griffin, L.W., Huber, F., and Sondak, D.L. (2002a). Unsteady Flow in a Supersonic Turbine with Variable Specific Heats. *Journal of Propulsion and Power*, 18, pp. 493–496.

Dorney, D.J., Griffin, L.W., and Huber, F.W. (2000b). A Study of the Effects of Tip Clearance in a Supersonic Turbine. *Journal of Turbomachinery*, 122, pp. 674–683.

Dorney, D.J., Griffin, L.W., Huber, F.W., and Sondak, D.L. (2002b). Effects of Endwall Geometry and Stacking on Two-Stage Supersonic Turbine Performance. In: *40th AIAA Aerospace Sciences Meeting and Exhibit*, AIAA-2002-78. Reno, NV, USA, Jan. 14-17, 2002.

Dorney, D.J., Griffin, L.W., and Sondak, D.L. (2004). Full- and Partial-Admission Performance of the Simplex Turbine. *Journal of Propulsion and Power*, 20, pp. 486–491.

Filsinger, D., Szwedowicz, J., and Schäfer, O. (2002). Approach to Unidirectional Coupled CFD-FEM Analysis of Axial Turbocharger Turbine Blades. *Journal of Turbomachinery*, 124, pp. 125–131.

Filsinger, D., Szwedowicz, J., Schäfer, O., and Dickmann, H.P. (2001). Pulse Charged Axial Turbocharger Turbines - a Challenge for Numerical Design Methods. In: *Proceedings of 23rd CIMAC World Congress on Combustion Engine Technology*, vol. 2, pp. 712–722. Hamburg, Germany, May 7-10, 2001.

Funazaki, K., Yamada, K., Kikuchi, M., and Sato, H. (2007). Experimental Studies on Aerodynamic Performance and Unsteady Flow Behaviors of a Single Turbine Stage with Variable Rotor-Stator Axial Gap: Comparisons with Time-Accurate Numerical Simulation. In: *Proceedings of ASME Turbo Expo 2007: Power for Land, Sea and Air*, GT2007-27670. Montreal, Canada, May 14-17.

Gaetani, P., Persico, G., Dossena, V., and Osnaghi, C. (2006a). Investigation of the Flow Field in a HP Turbine Stage for Two Stator-Rotor Axial Gaps: Part I - 3D Time-averaged Flow Field. In: *Proceedings of ASME Turbo Expo 2006: Power for Land, Sea and Air*, GT2006-90553. Barcelona, Spain, May 8-11.

Gaetani, P., Persico, G., Dossena, V., and Osnaghi, C. (2006b). Investigation of the Flow Field in a HP Turbine Stage for Two Stator-Rotor Axial Gaps: Part II - Unsteady Flow Field. In: *Proceedings of ASME Turbo Expo 2006: Power for Land, Sea and Air*, GT2006-90556. Barcelona, Spain, May 8-11.

Ghasemi, S., Shirani, E., and Hajilouy-Benisi, A. (2002). Performance Prediction of Twin-Entry Turbocharger Turbines. In: *Proceedings of ASME Turbo Expo 2002: Power for Land, Sea and Air*, GT2002-30576. Amsterdam, The Netherlands, June 3-6.

Griffin, L.W. and Dorney, D.J. (2000). Simulations of the Unsteady Flow Through the Fastrac Supersonic Turbine. *Journal of Turbomachinery*, 122, pp. 225–233.

Grönman, A. (2006). *Ylisoonisen yksivaiheisen aksiaaliturbiinin suunnittelu [Design of supersonic one-stage axial turbine]*. Master's thesis. Lappeenranta University of Technology. In Finnish.

Grönman, A., Turunen-Saaresti, T., Jaatinen, A., and Backman, J. (2010). Numerical Modelling of a Supersonic Axial Turbine Stator. *Journal of Thermal Science*, 19(3), pp. 211–217.

Groth, P., Mårtenson, H., and Edin, N. (2010). Experimental and Computational Fluid Dynamics Based Determination of Flutter Limits in Supersonic Space Turbines. *Journal of Turbomachinery*, 132, 011010.

Hakeem, I., Su, C.C., Costall, A., and Martinez-Botas, R.F. (2007). Effect of Volute Geometry on the Steady and Unsteady Performance of Mixed Flow Turbines. *Journal of Power and Energy*, 221, pp. 535–550.

Harinck, J., Turunen-Saaresti, T., and Colonna, P. (2007). *Performance and CFD Analyses of a High-Expansion-Ratio Radial ORC Turbine*. Technical Report. ET-2262. Delft University of Technology, Process and Energy Department, Energy Technology Section, The Netherlands.

Harinck, J., et al. (2010). Computational Study of a High-Expansion Ratio Radial Organic Rankine Cycle Turbine Stator. *Journal of Engineering for Gas Turbines and Power*, 132, 054501.

Hellström, F. and Fuchs, L. (2008). Numerical Computations of Pulsatile Flow in a Turbo-Charger. In: *46th AIAA Aerospace Science Meeting and Exhibit*. Reno, NV, USA, Jan. 7-10, 2008.

Hoffren, J. (1992). *Time-Accurate Schemes for a Multi-Block Navier-Stokes Solver*. Technical Report. A-14. Helsinki University of Technology, Laboratory of Aerodynamics.

Hoffren, J., Talonpoika, T., Larjola, J., and Siikonen, T. (2002). Numerical Simulation of Real-Gas Flow in a Supersonic Turbine Nozzle Ring. *Journal of Engineering for Gas Turbines and Power*, 124, pp. 395–403.

Honkatukia, J. (2006). *Diesel Process Simulations with Matlab and GT-Power*. Unpublished.

Ijichi, N., et al. (1998). Development of a High Expansion Ratio, Single-Stage Axial Turbine for Marine Turbocharger. In: *6th International Conference on Turbocharging and Air Management Systems*, IMechE Paper C554/009/98, pp. 303–314. London, UK, Nov. 3-5.

Jaatinen, A. (2009). *Performance Improvement of Centrifugal Compressor Stage with Pinched Geometry or Vaned Diffuser*. Ph.D. thesis. Lappeenranta University of Technology, Finland.

Jeong, E., Park, P.K., Kang, S.H., and Kim, J. (2006). Effect of Nozzle-Rotor Clearance on Turbine Performance. In: *Proceedings of FEDSM2006 2006 ASME Joint U.S.-European Fluids Engineering Summer Meeting*, FEDSM2006-98388. Miami, FL, USA, July 17-20.

Jöcker, M. (2002). *Numerical Investigation of the Aerodynamic Vibration Excitation of High-Pressure Turbine Rotors*. Ph.D. thesis. Royal Institute of Technology, Sweden.

Karamanis, N. and Martinez-Botas, R.F. (2002). Mixed Flow Turbines for Automotive Turbochargers: Steady and Unsteady Performance. *International Journal of Engine Research*, 3, pp. 127–138.

Lam, J.K.W., Roberts, Q.D.H., and McDonnel, G.T. (2002). Flow Modelling of a Turbocharger Turbine Under Pulsating Flow. In: *7th International Conference on Turbochargers and Turbocharging*, IMechE Paper C602/025/2002, pp. 181–197. London, UK, May 14-15.

Larjola, J., et al. (2009). *GENSET subtask 1.6: Turbocharging, final report (2005-2009)*. Technical report. Lappeenranta University of Technology, Helsinki University of Technology.

Lombard, C.K., Bardina, J., Venkatapathy, E., and Oliger, J. (1983). Multi-Dimensional Formulation of CSCM - an Upwind Flux Difference Eigenvector Split Method for Compressible Navier-Stokes Equations. In: *6th AIAA Computational Fluid Dynamics Conference*, Paper 83-1895-CP, pp. 649–664. Danvers, MA, USA, July 13-15.

Palfreyman, D. and Martinez-Botas, R.F. (2005). The Pulsating Flow Field in a Mixed Flow Turbocharger Turbine: An Experimental and Computational Study. *Journal of Turbomachinery*, 127, pp. 144–155.

Pan, H. (1993). *Two-Dimensional Navier-Stokes Computations of Subsonic and Supersonic Flows Through Turbine Cascades*. Technical report. T-66. Helsinki University of Technology, Laboratory of Aerodynamics.

Rajoo, S. and Martinez-Botas, R.F. (2007). Unsteady Effect in a Nozzled Turbocharger Turbine. In: *Proceedings of ASME Turbo Expo 2007: Power for Land, Sea and Air*, GT2007-28323. Montreal, Canada, May 14-17.

Rashid, S., Tremmel, M., Waggott, J., and Moll, R. (2006). Curtis Stage Nozzle/Rotor Aerodynamic Interaction and the Effect on Stage Performance. In: *Proceedings of ASME Turbo Expo 2006: Power for Land, Sea and Air*, GT2006-91115. Barcelona, Spain, May 8-11.

Reichert, A.W. and Simon, H. (1997). Design and Flow Field Calculations for Transonic and Supersonic Radial Inflow Turbine Guide Vanes. *Journal of Turbomachinery*, 119, pp. 103–113.

Reunanen, A. (2001). *Experimental and Numerical Analysis of Different Volutes in a Centrifugal Compressor*. Ph.D. thesis. Lappeenranta University of Technology, Finland.

Roe, P.L. (1981). Approximate Riemann Solvers, Parameter Vectors and Difference Schemes. *Journal of Computational Physics*, 43, pp. 357–372.

Sadovnichiy, V.N., Binner, M., and Seume, J.R. (2009). The Influence of Axial Gaps and Leaned-Twisted Guide Vanes on the Shroud Leakage and Turbine Stage Efficiency. In: Heitmeier, F., Martelli, F., and Manna, M., eds, *Proceedings of 8th European Conference on Turbomachinery*, pp. 1459–1468. Graz, Austria, March 23-27, 2009. Graz: Verlag der Technischen Universität Graz.

Schäfer, O. (2002). Simulation of Unsteady Compressible Flow in Turbomachinery. *Progress in Computational Fluid Dynamics*, 2, pp. 1–8.

Siikonen, T., Rautaheimo, P., and Salminen, E. (2004). *Finflo User Guide, Version 7.2*. Helsinki University of Technology, Laboratory of Applied Thermodynamics.

Sonoda, T., et al. (2006). A Study of Advanced High-Loaded Transonic Turbine Airfoils. *Journal of Turbomachinery*, 128, pp. 650–657.

Tang, J. (2006). *Computational Analysis and Optimization of Real Gas Flow in Small Centrifugal Compressors*. Ph.D. thesis. Lappeenranta University of Technology, Finland.

Traupel, W. (1977). *Thermische Turbomachinen*, 3rd edn, vol. I - Thermodynamisch-strömungstechnische Berechnung. Berlin, Heidelberg, New York: Springer-Verlag.

Turunen-Saaresti, T. (2004). *Computational and Experimental Analysis of Flow Field in the Diffusers of Centrifugal Compressors*. Ph.D. thesis. Lappeenranta University of Technology, Finland.

Turunen-Saaresti, T., Tang, J., van Buijtenen, J., and Larjola, J. (2006). Experimental and Numerical Study of a Real-Gas Flow in a Supersonic ORC Turbine Nozzle. In: *Proceedings of ASME Turbo Expo 2006: Power for Land, Sea and Air*, GT2006-91118. Barcelona, Spain, May 8-11.

Venable, B.L., et al. (1999). Influence of Vane-Blade Spacing on Transonic Turbine Stage Aerodynamics: Part I - Time-Averaged Data and Analysis. *Journal of Turbomachinery*, 121, pp. 663–672.

Yamada, K., Funazaki, K., Kikuchi, M., and Sato, H. (2009). Influences of Axial Gap Between Blade Rows on Secondary Flows and Aerodynamic Performance in a Turbine Stage. In: *Proceedings of ASME Turbo Expo 2009: Power for Land, Sea and Air*, GT2009-59855. Orlando, FL, USA, June 8-12.

ACTA UNIVERSITATIS LAPPEENRANTAENSIS

349. JUUTILAINEN, MATTI. Towards open access networks – prototyping with the Lappeenranta model. 2009. Diss.

350. LINTUKANGAS, KATRINA. Supplier relationship management capability in the firm´s global integration. 2009. Diss.

351. TAMPER, JUHA. Water circulations for effective bleaching of high-brightness mechanical pulps. 2009. Diss.

352. JAATINEN, AHTI. Performance improvement of centrifugal compressor stage with pinched geometry or vaned diffuser. 2009. Diss.

353. KOHONEN, JARNO. Advanced chemometric methods: applicability on industrial data. 2009. Diss.

354. DZHANKHOTOV, VALENTIN. Hybrid LC filter for power electronic drivers: theory and implementation. 2009. Diss.

355. ANI, ELISABETA-CRISTINA. Minimization of the experimental workload for the prediction of pollutants propagation in rivers. Mathematical modelling and knowledge re-use. 2009. Diss.

356. RÖYTTÄ, PEKKA. Study of a vapor-compression air-conditioning system for jetliners. 2009. Diss.

357. KÄRKI, TIMO. Factors affecting the usability of aspen (Populus tremula) wood dried at different temperature levels. 2009. Diss.

358. ALKKIOMÄKI, OLLI. Sensor fusion of proprioception, force and vision in estimation and robot control. 2009. Diss.

359. MATIKAINEN, MARKO. Development of beam and plate finite elements based on the absolute nodal coordinate formulation. 2009. Diss.

360. SIROLA, KATRI. Chelating adsorbents in purification of hydrometallurgical solutions. 2009. Diss.

361. HESAMPOUR, MEHRDAD. Treatment of oily wastewater by ultrafiltration: The effect of different operating and solution conditions. 2009. Diss.

362. SALKINOJA, HEIKKI. Optimizing of intelligence level in welding. 2009. Diss.

363. RÖNKKÖNEN, JANI. Continuous multimodal global optimization with differential evolution-based methods. 2009. Diss.

364. LINDQVIST, ANTTI. Engendering group support based foresight for capital intensive manufacturing industries – Case paper and steel industry scenarios by 2018. 2009. Diss.

365. POLESE, GIOVANNI. The detector control systems for the CMS resistive plate chamber at LHC. 2009. Diss.

366. KALENOVA, DIANA. Color and spectral image assessment using novel quality and fidelity techniques. 2009. Diss.

367. JALKALA, ANNE. Customer reference marketing in a business-to-business context. 2009. Diss.

368. HANNOLA, LEA. Challenges and means for the front end activities of software development. 2009. Diss.

369. PÄTÄRI, SATU. On value creation at an industrial intersection – Bioenergy in the forest and energy sectors. 2009. Diss.

370. HENTTONEN, KAISA. The effects of social networks on work-team effectiveness. 2009. Diss.

371. LASSILA, JUKKA. Strategic development of electricity distribution networks – Concept and methods. 2009. Diss.

372. PAAKKUNAINEN, MAARET. Sampling in chemical analysis. 2009. Diss.

373. LISUNOV, KONSTANTIN. Magnetic and transport properties of II-V diluted magnetic semiconductors doped with manganese and nickel. 2009. Diss.

374. JUSSILA, HANNE. Concentrated winding multiphase permanent magnet machine design and electromagnetic properties – Case axial flux machine. 2009. Diss.

375. AUVINEN, HARRI. Inversion and assimilation methods with applications in geophysical remote sensing. 2009. Diss.

376. KINDSIGO, MERIT. Wet oxidation of recalcitrant lignin waters: Experimental and kinetic studies. 2009. Diss.

377. PESSI, PEKKA. Novel robot solutions for carrying out field joint welding and machining in the assembly of the vacuum vessel of ITER. 2009. Diss.

378. STRÖM, JUHA-PEKKA. Active*d*u/d*t* filtering for variable-speed AC drives. 2009. Diss.

379. NURMI, SIMO A. Computational and experimental investigation of the grooved roll in paper machine environment. 2009. Diss.

380. HÄKKINEN, ANTTI. The influence of crystallization conditions on the filtration characteristics of sulphathiazole suspensions. 2009. Diss.

381. SYRJÄ, PASI. Pienten osakeyhtiöiden verosuunnittelu – empiirinen tutkimus. 2010. Diss.

382. KERKKÄNEN, ANNASTIINA. Improving demand forecasting practices in the industrial context. 2010. Diss.

383. TAHVANAINEN, KAISA. Managing regulatory risks when outsourcing network-related services in the electricity distribution sector. 2010. Diss.

384. RITALA, PAAVO. Coopetitive advantage – How firms create and appropriate value by collaborating with their competitors. 2010. Diss.

385. RAUVANTO, IRINA. The intrinsic mechanisms of softwood fiber damage in brown stock fiber line unit operations. 2010. Diss.

386. NAUMANEN, VILLE. Multilevel converter modulation: implementation and analysis. 2010. Diss.

387. IKÄVALKO, MARKKU. Contextuality in SME ownership – Studies on owner-managers´ ownership behavior. 2010. Diss.

388. SALOJÄRVI, HANNA. Customer knowledge processing in key account management. 2010. Diss.

389. ITKONEN, TONI. Parallel-Operating Three-Phase Voltage Source Inverters – Circulating Current Modeling, Analysis and Mitigation. 2010. Diss.

390. EEROLA, TUOMAS. Computational visual quality of digitally printed images. 2010. Diss.

391. TIAINEN, RISTO. Utilization of a time domain simulator in the technical and economic analysis of a wind turbine electric drive train. 2010. Diss.